Final Report:

Improving the Accuracy of Mixing Depth Predictions from the Mesoscale Meteorological Model MM5

CARB Contract Number: 96-319

Prepared for

Jim Pederson, Project Officer
California Air Resources Board and the California Environmental Protection Agency

Prepared by

Kirankumar V. Alapaty, Principal Investigator (MCNC)
    (919) 248-9253; alapaty@ncsc.org
Nelson L. Seaman, Co-Principal Investigator (The Pennsylvania State University)

Environmental Programs
MCNC–North Carolina Supercomputing Center
P.O. Box 12889
Research Triangle Park, NC 27709-2889

Disclaimer

The statements and conclusions in this report are those of the Contractor and not necessarily those of the California Air Resources Board. The mention of commercial products, their source, or their use in connection with material reported herein is not to be construed as actual or implied endorsement of such products.

Acknowledgments

Table of Contents

Abstract

This research work was initiated to determine modeling aspects that control the accuracy of the estimated mixed-layer depths over central California, calculated by meteorological models. Most importantly, we focused on surface and large-scale atmospheric process representations and studied their effects in controlling the growth of the daytime boundary layer over this region.

First, using a 1-D boundary layer model, we studied and improved the representation of surface processes. We developed a technique to facilitate the assimilation of surface data into the model without damaging the modeled mixed-layer structures. We then demonstrated that the modeled boundary layer predictions are improved and are closer to the observations when using this technique. Next we developed and tested a formulation to improve the estimation of surface latent heat fluxes; it allows the vegetation component to be included explicitly in the land surface parameterization. We found that this formulation improved modeled surface fluxes and thus improved boundary layer predictions. These two new methods need further testing in a 3-D mesoscale model.

Second, using the Mesoscale Model, Version 5 (MM5) with a nested-grid configuration, we studied the interactions of large-scale processes with the growth of the boundary layer.. We performed several sensitivity studies to understand the interactions of processes and to weed out insignificant aspects of model configurations. We found that increasing model vertical resolution from 32 to 62 layers did not lead to a significant skill increase in the model estimations. Inclusion of a large outer domain covering the East Pacific Ridge helped to yield better model solutions in the inner domains. Removal of analysis nudging in coarser domains in the lowest 1.5 km also improved the model solutions in the innermost domain in which no nudging was performed. Boundary layer initialization over the marine environment did not much improve the model solutions. Finally, application of a physically robust boundary layer scheme resulted in further improvements in the model predictions compared to a simple boundary layer scheme. Thus, we found that an enhanced model configuration did lead to improved mixed-layer predictions over central California.

Executive Summary

BACKGROUND

Accurate meteorological information is needed to support air quality modeling, which is used to predict future air quality, determine the effects from control of emissions, and formulate the State implementation plans for attaining federal standards for ozone and particulate matter. Ambient pollutant concentrations are sensitive to the mixing depth; therefore, this depth must be correctly characterized for reliable air quality modeling results. Meteorological models that both simulate the thermodynamics of the atmosphere and utilize meteorological observations can better characterize the spatial and temporal variability of mixing depth, winds, and other variables needed in the air quality model, compared to what can be done using diagnostic modeling of the observations. The objective of this study was to improve the accuracy of the mixing depth estimates generated by the meteorological, state-of-the-science model widely known as MM5 and used by the ARB. This model simulates the physical processes and assimilates information from meteorological measurements. MM5 was demonstrated, in developing the State Implementation Plan for Ozone, to reproduce the significant flow features in areas of complex terrain with finer detail than would be expected from the spacing of the available observations. However, MM5 overestimated the mixing depth when used with limited observations.

METHODS

We investigated the numerical and physical processes in the model that affect estimation of mixing depth and potential sources of inaccuracy in mixed-layer depths over central California, when simulated by a standard formulation of the meteorological model MM5. Study of the representation of surface processes, using a 1-D boundary layer model to identify factors influencing daytime mixed-layer depths resulted in the development and testing of two new methodologies to improve boundary layer predictions. One improvement is a new technique for assimilating observations of the surface layer into the model, while maintaining consistent thermodynamic relationships and modeled mixed-layer structures. The other improvement allows explicit representation of the latent heat flux from vegetation, within the land surface parameterization, thereby improving the estimates of total latent heat flux and the partition of available energy between latent and sensible heat. These two new methods will require further testing in a 3-D mesoscale model.

Next, using the Mesoscale Model, Version 5 (MM5) with a nested-grid configuration, we studied the effects of large-scale atmospheric processes on the growth of the boundary layer. Several sensitivity studies were performed to understand process interactions and identify the significant and insignificant aspects of model configurations. These studies focused on the effects of (1) large-scale dynamics and thermodynamics,

(2) vertical resolution, (3) initializing the marine atmospheric boundary layer, (4) mesoscale circulations in the Sacramento Valley, (5) different boundary-layer turbulence parameterizations, and (6) use of a four-dimensional data assimilation strategy.

RESULTS

Our new formulation to perform consistent adjustment of ground temperature, along with the assimilation of temperature and water vapor mixing ratio in the surface layer, mixed layer, and free atmosphere, led to very significant improvements in the simulated boundary layer depth and its structures. Using a 1-D model, assimilation of surface temperature observations can be used successfully to adjust for uncertainties in surface characteristics, such as soil moisture specifications and inaccuracies in boundary layer parameterizations. Using the same 1-D model, we also developed and tested a new formulation that introduces vegetative effects into the equation that is being used in MM5 for estimating surface latent heat fluxes. This formulation uses many surface and vegetation parameters, as do other sophisticated land surface schemes. But the new formulation takes a diagnostic approach, providing many advantages over prognostic approaches.

We found that increasing MM5 model vertical resolution from 32 to 62 layers did not lead to a significant skill increase in the model estimations. Inclusion of a large outer domain, covering the East Pacific Ridge, helped to yield better model solutions in the inner domains. Removal of analysis nudging in coarser domains in the lowest 1.5 kilometers also helped the model solutions in the innermost domain in which no nudging was performed. Boundary layer initialization over the marine environment did not significantly improve the model solutions. Finally, application of a physically robust boundary layer scheme resulted in further improvements in the model predictions, compared to a simple boundary layer scheme.

CONCLUSIONS

Results obtained from the 1-D model simulations indicated very good improvement in the boundary layer predictions using the two new methodologies. We have demonstrated that an enhanced MM5 model configuration improved mixed-layer predictions over central California and confirmed that a vertical resolution of 32 layers was adequate. To further improve boundary layer predictions over the central California region, particularly for use in air pollution modeling studies, it is highly desirable that the new formulations developed in this study be implemented and tested rigorously in MM5. Because the 1-D model results were very

encouraging, we anticipate that the implementation of the new formulations in MM5 will lead to better predictions of mixed-layer depths.

1. Introduction

Measured ozone concentrations at the surface during the summer in California's San Joaquin Valley (SJV) often exceed the limits set by the Federal government. To better understand the meteorological and chemical characteristics of the atmosphere and air quality over central California, the California Air Resources Board (CARB) has undertaken extensive observational and modeling studies of the meteorological influences on air quality over the San Joaquin Valley (SJV) region. Special observation programs capable of providing atmospheric data with dense horizontal and temporal resolution are vital for better understanding of the complex mesoscale circulations. For example, the San Joaquin Valley Air Quality Study (SJVAQS) and the Atmospheric Utility Signatures, Predictions, and Experiments (AUSPEX) project were conducted simultaneously in summer 1990 and provided excellent upper-air coverage as well as a fine-scale network of surface observations (Ranzieri and Thuillier 1991). However, such special field programs are very expensive to operate even for limited periods. Therefore, numerical dynamical modeling has become a very important method for providing a comparatively inexpensive means to study mesoscale atmospheric structures and to supply quality meteorological inputs for air chemistry models.

During the summer months, especially during episodes of high ozone concentrations, mixing depths in the San Joaquin Valley of California are known to be quite low compared to those of other semi-arid parts of the western United States. These shallow mixing depths occur in conjunction with maximum surface temperatures that often exceed 35-40 °C. In contrast, it is common in this season for many other inland semi-arid areas throughout the West to have similar temperatures, but with convectively unstable boundary layers exceeding 3 kilometers (km) in depth. These deep mixed layers are normal for areas as close to the SJV as the Mojave Desert and Nevada. However, at the same time, mixing depths for convectively unstable boundary layers in the SJV can be as low as 400-800 meters (m). Because these low mixing depths have important implications for understanding air quality in the SJV and the specific mechanisms responsible for them are unclear, this phenomenon has significant scientific and practical importance.

It is well known that shallow mixing depths tend to reduce ventilation and thereby concentrate pollutants near the surface. In the SJV, unlike the Los Angeles Basin, the capping inversion above the mixed layer tends to be quite weak, often no more than 1 °C. Meanwhile, a very strong, shallow capping inversion (often exceeding 15 °C) is typically found upwind over the Pacific Ocean and in coastal regions only a few hundred kilometers away. Therefore, there are important questions regarding the origin of the shallow boundary layers in the SJV. Are they due to inland advection of the marine mixed layer? Are they due to local or even synoptic-scale circulations? Finding clear answers to these questions is important because of their implications for regional air quality in that area.

Numerical dynamical modeling is a key tool used for answering such questions. For example, under the SJVAQS/AUSPEX Regional Modeling Adaptation Project (SARMAP) study, the rich SJVAQS/AUSPEX observational database was used with the SARMAP Mesoscale Model (SMM) (Seaman et al., 1995; Seaman and Stauffer, 1995) to simulate circulation features over California and surrounding states and to provide meteorological data to the SARMAP Air Quality Model (SAQM) (Chang et al., 1996). The SMM is an advanced version of the Penn State University/National Center for Atmospheric Research (PSU/NCAR) Mesoscale Model (MM5), developed by Seaman et al. (1995). Two primary objectives of the SARMAP study were to better understand the meteorology of the high-ozone episodes and to establish the viability of the

MM5–Four-Dimensional Data Assimilation (FDDA) system. The study included statistical evaluations of the SMM/MM5 and its ability to simulate specific mesoscale structures of the wind and thermal fields.

One of the main findings of Seaman et al. (1995) is that the SMM/MM5 system overestimates the depth of the mixed layer. In the innermost nested domain (4-km horizontal resolution), which covers central California, estimated depths of the atmospheric boundary layer (ABL) during the period 1200 UTC August 2 through 1200 UTC August 7, 1990, were found to have a mean error of +343 m. At individual grid points (e.g., over the southern SJV), the estimated error in the ABL depth was found to be as high as 900 m. It was also found that applying special thermal sounding data in addition to the regular analysis nudging reduced the mean error in the estimated depths to 139 m. These results pertain to the simulations where Blackadar's nonlocal-closure scheme was used to represent the convective boundary layer (CBL) processes. Seaman et al. (1995) further found that use of the turbulent kinetic energy (1.5-order closure) scheme to represent the ABL processes has two advantages compared to Blackadar's scheme: (1) the opportunity exists to assimilate the surface-layer temperatures in the SMM/MM5 modeling system, and (2) estimated ABL depths with the 1.5-order scheme are better than those obtained using Blackadar's scheme.

Realistic representation of ABL processes is very important because they control the dynamic, thermodynamic, and chemical states of the lower troposphereWhen meteorological model predictions are used to drive an air quality modeling system, errors resulting from the inaccurate specification of boundary layer parameters can adversely affect the resultant concentrations of simulated atmospheric pollutants (Sistla et al. 1996, Russell and Dennis 2000). For example, a poor simulation of ABL depth can adversely influence other turbulence processes, such as the upward eddy-transport of surface emissions and fumigation of elevated pollutants to the surface. These errors in turn can affect the nonlinearity of the chemical system and hence the concentrations of secondary chemical species. Alapaty and Mathur (1998) showed that differences in the estimated depths of the mixed layer resulting from several local- and nonlocal-closure ABL schemes resulted in large differences among the simulated concentrations of various atmospheric chemical pollutants.

Another important component of ABL modeling is the realistic representation of land surface characteristics and associated processes. The effects of uncertainty in the specification of surface characteristics on simulated ABL processes and structure are widely recognized, and have been reviewed by many researchers (e.g., Alapaty et al., 1997a; Niyogi et al., 1999). Several studies (e.g., Pleim and Xiu 1995, Alapaty et al. 1997a, Niyogi et al. 1999) have pointed out that uncertainty in the representation of surface characteristics and turbulent processes can lead to serious prediction errors, mainly in the temperature and moisture fields within the ABL, while errors in the predicted dynamic fields (Alapaty et al.1997a) are less significant. In an effort to reduce modeling errors, several sophisticated soil-vegetation parameterization schemes have been developed that provide fairly realistic representations of land surface-atmosphere exchange processes in meteorological models. However, using these comprehensive schemes require specifying many input variables, some of which may be poorly known (e.g., soil porosity).

Lack of specific input data has been a major hindrance in the ability to use complex soil-vegetation schemes with a high degree of confidence in 3-D meteorological models. For example, Lakhtakia (1999) used a sophisticated land surface scheme, the Biosphere Atmosphere Transfer Scheme (BATS) (Dickinson et al. 1993), and a very simple moisture flux scheme to perform numerical simulations using a regional climate model. It was found that simulation results obtained using the simple scheme were superior to those obtained using BATS due in part to the uncertainty in the specification of surface parameters. Such results clearly demonstrate the gross effects of uncertainties in the specification of surface characteristics. Moreover, proper

specification of soil moisture in meteorological models can be particularly important, even for short-range weather forecasts, because it can have a large nonlinear influence on the surface sensible and latent heat fluxes (Niyogi et al. 1999) and thus on the kinetic energy of the turbulent eddies. However, because observed soil moisture data are not routinely available, errors in initial estimates used in meteorological models can be difficult to detect and correct.

Errors in the ABL predictions can also result from deficiencies and/or assumptions used in various ABL parameterizations. For example, Alapaty et al. (1997b) studied the performance of several local- and nonlocal-closure ABL schemes using a 1-D model. They found that near-surface turbulent fluxes predicted by each of the ABL schemes differed from one another by a maximum of about 22%, even though the formulation used to represent the surface-layer processes was the same. These differences arose from differing ways of representing subgrid-scale vertical mixing processes. They also found that vertical profiles of predicted dynamic and thermodynamic parameters from each of the ABL schemes differed from the others, particularly during daytime growth of the ABL.

Similarly, as mentioned earlier, the SARMAP study (Ranzieri and Thuiller 1991) involving 3-D numerical simulations using the nonhydrostatic MM5 found that the depth of the mixed layer was overestimated in central California (mean error +343 m). They noted that a low–level capping inversion is a characteristic feature of the thermal structure of the summertime CBL over central California during periods having poor air quality. This capping inversion is often so weak that it is difficult to define its altitude unambiguously. In these situations, accurate representation of mesoscale processes in a model is crucial, particularly those influencing the growth of the ABL, because modest errors can easily erode the inversion, resulting in unrealistic development of deep mixed layers as reported by Seaman et al. (1995). It was also found that assimilating special mesoscale thermal sounding data reduced the mean error in the estimated ABL depths to 139 m. However, at certain sounding locations (e.g., over the southern SJV), this approach failed and the estimated error in the depth of the ABL was found to be over 80%. To alleviate these types of prediction errors, Ruggiero et al. (1996) studied the effects of frequent intermittent assimilation of surface observations using an objective analysis in an intermittent technique. They found that their simple technique improved mesoscale analyses and forecasts. Recently, Lohmann et al. (1999) performed 1-D simulations using a simple relaxation assimilation technique to improve their model simulations. A disadvantage in their method is the uncertainty in specifying the relaxation time scale.

In general, modeled ABL processes can be affected by (1) the accuracy of the initial conditions and specified parameters, (2) the type of formulation used to represent surface processes, (3) the formulation used for turbulent mixing processes, (4) the vertical resolution of the model, and (5) the effective simulation of mesoscale and large-scale dynamics. Despite progress in reducing errors associated with each of these factors, it remains difficult to prevent significant errors in all cases. As discussed above, such errors can have damaging effects in subsequent air pollution modeling. There is a need to develop improved data assimilation techniques for thermodynamic variables to further alleviate prediction errors in the ABL. We hypothesized that simulation errors in the ABL could be reduced if the measured or analyzed temperature and moisture data in the surface layer could be assimilated in a way that causes little disruption of the model's physical processes within the ABL, but instead focuses the corrective measures at the surface, which strongly controls the natural evolution of the ABL.

The goal of the research work we undertook for the CARB project described in this report was to gain a better understanding of the various aspects that control the accuracy of the estimated mixed-layer depths in a

meteorological model such as MM5. The project's results can be used to increase the accuracy and usefulness of meteorological models for studying and improving air quality in California and elsewhere.

2. Project Objectives

This project had two major objectives:

1. To determine factors that influence the growth of a CBL

2. To suggest, develop, and test methodologies that lead to increased accuracy in central California CBL depths simulated by meteorological models

To accomplish these objectives, we chose three modeling pathways: (1) study the influence of various surface and boundary layer parameters on the accuracy of simulated mixed-layer depths, (2) develop and test new methodologies that control the error growth in the simulated mixed-layer depths, and (3) study how various aspects of modeling large-scale flow affect CBL depths during a summer period in central California. We accomplished objectives 1 and 2 using a 1-D boundary layer model and objective 3 using a 3-D meteorological model.

3. Investigation of Causes of Overestimated Mixed-Layer Depths and Testing of Improvements

To accomplish the objectives of this research project, we performed extensive 1-D and 3-D model simulations. Details are given in the following sections.

3.1 One-Dimensional Model Simulations

The objectives of the 1-D modeling study are (1) to illustrate how uncertainty present in the specification of surface characteristics and ABL parameterizations affects the simulated ABL structures, and (2) to demonstrate the feasibility of a new technique that allows continuous data assimilation of surface observations to improve the boundary layer predictions. To accomplish these objectives, we performed several numerical simulations using a 1-D soil-vegetation ABL model developed by Alapaty et al. (1997b).

3.1.1 Model Description

The 1-D model of Alapaty et al. (1997b) uses advanced local and nonlocal boundary layer formulations to realistically represent turbulent processes of the ABL with an efficiency suitable for use in 3-D models. For this study the model was configured with 35 vertical layers between the surface and ~5000 m altitude. It predicts the wind (eastward and northward components), temperature, and mixing ratio of water vapor. The 1-D model provides the option to specify externally the horizontal advection of all prognostic variables. The user can select from various turbulence schemes and soil-vegetation interaction formulations; however, we describe below only the physical parameterization schemes that were used in this study. For further details, refer to Alapaty et al. (1997b).

3.1.2 Land Surface Parameterization Schemes

In this study we chose two types of formulations to estimate the surface latent heat fluxes: (1) a diagnostic formulation suggested by Carlson and Boland (1978), which is available in MM5; and (2) the soil-vegetation parameterization scheme suggested by Noilhan and Planton (1989) and Jacquemin and Noilhan (1990). In both the formulations there are two soil layers, representing surface and subsurface processes; the first layer is 0.01 m thick and the second is 1 m thick. The prognostic equations used to calculate the temperatures and soil moisture contents of these two layers are shown in Eqs. 1–6; the temperature tendency equations (1 and 2) are based on a force-restore method and are the same in both formulations.

The rate of change of the mean soil temperature of layer 1 can be written as

$$\frac{\partial T_{g1}}{\partial t} = C_T (R_n - S_{hf} - L_{hf}) - \frac{2p}{t}(T_{g1} - T_{g2}) \tag{1}$$

where T_{g1} and T_{g2} are the temperatures of layers 1 and 2; C_T is the inverse of the thermal capacity of a particular soil type; R_n is the net radiation at the surface; S_{hf} and L_{hf} are the surface sensible and latent heat fluxes; and τ is the number of seconds in a day. The mean temperature of layer 2 is given by (Blackadar 1976):

$$\frac{\partial T_{g2}}{\partial t} = \frac{(T_{g1} - T_{g2})}{t} \tag{2}$$

The first formulation used to estimate surface kinematic latent heat flux, suggested by Carlson and Boland (1978), can be written as

$$L_{hf} = \frac{M_a k u_* \left(q_{vs}(T_g) - q_{va} \right)}{\lambda n \left(\frac{k u_* z_a}{K_a} + \frac{z_a}{z_\lambda} \right) - \Phi_h} \tag{3}$$

where M_a is the soil moisture availability, k the von Karman constant, u_* the friction velocity, q_{vs} the saturated water vapor mixing ratio at temperature T_g, q_{va} the water vapor mixing ratio of air in the lowest layer of the model, z_a the altitude of the lowest level in the model, K_a the background molecular diffusivity, z_λ the depth of the molecular layer, and Φ_h the nondimensional stability parameter for heat. In the Carlson and Boland formulation, M_a is generally specified as a constant.

The second, more detailed formulation to estimate surface latent heat fluxes was suggested by Noilhan and Planton (1989). In this formulation prognostic equations for the soil moisture of the two layers are given as

$$\frac{\partial W_{g1}}{\partial t} = \frac{C_1}{r_w d_1}(P_g - E_g) - \frac{C_2}{t}(W_{g1} - W_{geq}) \tag{4}$$

$$\frac{\partial W_{g2}}{\partial t} = \frac{(P_g - E_g - E_{tr})}{r_w d_2} \tag{5}$$

9

where W_{g1} and W_{g2} are the volumetric soil moisture contents of the two soil layers, C_1 and C_2 are soil moisture coefficients (see Noilhan and Planton 1989), ρ_w is the density of liquid water, d_1 and d_2 are the layer thicknesses, P_g is the flux of liquid water reaching the soil surface, E_g is the evaporation flux at the soil surface, W_{geq} is the layer 1 soil moisture when gravity balances the capillary forces, and E_{tr} is the transpiration flux. The water content on the wet parts of the canopy due to rainfall and/or dew formation on the foliage is represented by W_r. The prognostic equation for W_r is based on Deardorff's (1978) formulation and can be written as

$$\frac{\partial W_r}{\partial t} = (V_c P_r) - E_r - R_r \qquad (6)$$

where V_c is the vegetation cover in fractional units, P_r is the precipitation rate at the top of the vegetation, and E_r is the evaporation rate from the wet parts of the canopy, and R_r is the runoff rate from canopy interception reservoir. The total kinematic latent heat flux (E) into the atmosphere's surface layer is the sum of bare ground evaporation, transpiration from plant canopies, and evaporation from wet parts of the canopy (due to dew formation and/or rainfall interception). This can be written as

$$E = (E_g + E_{tr} + E_r)/\rho_a \qquad (7)$$

where ρ_a is the air density at the surface. The two land surface schemes differ in that the Carlson and Boland (1978) formulation uses constant moisture availability (M_a is a function of land use type), while moisture availability is a prognostic variable (W_{g1} and W_{g2}) in the Noilhan and Planton (1989) scheme.

A simple surface radiation model is used in the 1-D ABL model. Net radiation at the surface is calculated as the sum of incoming solar radiation absorbed at the surface, atmospheric longwave back-scattering radiation, and outgoing longwave surface radiation. The solar radiation reaching the surface is a function of solar zenith angle, surface albedo, and atmospheric turbidity. Surface albedo is computed as the sum of minimum albedo with a solar zenith angle of zero and albedo changes due to the variation in the solar zenith angle (Idso et al. 1975; Pleim and Xiu 1995). Upward and downward longwave radiation are calculated as suggested by Grell et al. (1994), as functions of soil emissivity, ground temperature, atmospheric longwave emissivity, and atmospheric temperatures.

3.1.3 Surface-Layer Formulation

The lower boundary layer (surface layer) is parameterized based on similarity theory suggested by Monin and Yaglom (1971) using the nondimensional stability parameters Φ_m, Φ_h, and Φ_q for momentum, heat, and moisture, respectively. Turbulent kinematic sensible heat fluxes are computed using the relationship given by

$$S_{hf} = u_* \boldsymbol{q}_*$$

where u_* is friction velocity and θ_* is the scale for temperature, while the turbulent kinematic latent heat fluxes are estimated using either Eq. 3 or 7.

3.1.4 Mixed-Layer Formulations

In this study, we used two different mixed-layer formulations: (1) an ABL scheme based on turbulent kinetic energy and its dissipation rate (E-ε) (a local-closure model); and (2) a combination of the Asymmetric

Convective Model (ACM) (a nonlocal-closure model) and a K-theory-based scheme (a local-closure model). These two different mixed–layer formulations are described briefly below.

3.1.4.1 Turbulent Kinetic Energy (E-*e*) Scheme

The prognostic equations used in this scheme to explicitly calculate the turbulent kinetic energy (E) and its dissipation rate (ε) are those suggested by Mellor and Yamada (1974) and as used by Alapaty et al. (1997b). This scheme is often called a 1.5-order closure scheme in which the unknown terms in the prognostic equations are parameterized in terms of local gradients of dynamic and thermodynamic parameters. The coefficient of vertical eddy diffusivity for momentum is calculated from the ratio of E and ε. Surface-layer similarity profiles (Businger et al. 1971) are used for obtaining boundary conditions for the prognostic equations for E and ε, while for the mixed layer the E-ε scheme is used. For further details, the reader is referred to Alapaty et al. (1997b). The coefficients of eddy diffusivity for momentum and heat, K_m and K_h, can be written as

$$K_m = \frac{c_3 E^2}{e} \tag{8}$$

$$K_h = K_m \frac{\Phi_m(z/L)}{\Phi_h(z/L)} \tag{9}$$

where c_3 is an empirical constant (Detering and Etling 1985), Φ_m and Φ_h are nondimensional functions for momentum and heat (Businger et al. 1971), z is altitude, and L is Monin-Obukhov length.

3.1.4.2 Asymmetric Convective Model and K-Theory-Based Scheme (ACM-BKT Scheme)

The ACM is based on Blackadar's nonlocal-closure scheme (Blackadar 1979), which is based on the assumption that turbulent mixing is isotropic (i.e., symmetric) in the ABL. Noting that the observational evidence and large-eddy simulation modeling results of the mixing processes in a convective boundary layer (Schumann, 1989) are essentially asymmetric (i.e., turbulence is anisotropic), Pleim and Chang (1992) modified this model by adding asymmetry in the vertical mixing processes. However, the ACM can be used only during convective conditions in the ABL. For other stability regimes, a K-theory-based approach is used to represent the turbulence processes. We refer to this combination as the ACM-BKT scheme.

Asymmetric Convective Model: Turbulent mixing in the ABL for any dynamic or thermodynamic variable, S, can be written as

$$\frac{\partial S_i}{\partial t} = \sum_{j=1}^{N} S_j M_{ij}(t, \Delta t) \tag{10}$$

where i and j are indices for different model layers, N is the number of layers, the elements in the matrix M represent mass mixing rates, t is time, and Δt is the diffusion time step. Only a few pathways that represent the dominant mixing scales in the CBL are considered, resulting in a very sparse transilient matrix that can be solved numerically. Specifically, upward transport originates in the bottom-most layer and goes to all CBL layers above. Downward transport goes from each layer to the next lower layer. This simulates rapid upward

transport from the surface layer by buoyant plumes and more gradual compensatory subsidence. The calculation of the matrix elements is based on the conservation of sensible heat flux in the vertical direction. If M_u and M_d represent upward mixing and downward mixing rates, respectively, then Eq. 10 can be rewritten as

$$\frac{\partial S_i}{\partial t} = M_u S_1 - M_{di} S_i + M_{di+1} S_{i+1} \frac{\Delta \pmb{s}_{i+1}}{\Delta \pmb{s}_i} \tag{11}$$

where $\Delta \sigma$ is the relative mass in or thickness of cell *i* in a numerical model. The upward and downward mixing rates are estimated using the sensible heat flux. See Pleim and Chang (1992), Pleim and Xiu (1995), and Alapaty et al. (1997b) for details and performance tests of the ACM.

K-theory-based scheme: Because the ACM represents only the convective mixing in the ABL, we consider the formulations suggested by Businger et al. (1971) and Hass et al. (1991) to represent the turbulent processes in the stable boundary layer (we refer to this as the BKT scheme). This type of formulation has been successfully used to represent turbulent mixing in the ABL (see for example, Chang et al. 1987; Hass et al.1991). The coefficient of vertical eddy diffusivity, K_z, for the surface layer is

$$K_z = \frac{ku_*z}{\Phi_h(z/L)} \tag{12}$$

while for the stable or neutral mixed layer, it is

$$K_z = \frac{ku_*z\left(1 - \frac{z}{h}\right)^2}{\Phi_h(z/L)} \qquad \text{for h/L} \geq \text{-10} \tag{13}$$

where h is the depth of the boundary layer. In the free atmosphere, turbulent mixing is parameterized using the formulation suggested by Blackadar (1979) in which vertical eddy diffusivities are functions of the Richardson number and wind shear in the vertical. This formulation can be written as

$$K_z = K_o + S(k\lambda)^2 \frac{R_c - R_i}{R_c} \tag{14}$$

where K_o is the background value (1 m^2 s^{-1}), S is the vertical wind shear, l is the characteristic turbulent length scale (100 m), R_c is the critical Richardson number, and R_i is the Richardson number:

$$R_i = \frac{g}{\Theta_v S^2} \frac{\partial \Theta_v}{\partial z}$$

where g is the acceleration due to gravity and Θ_v is virtual potential temperature.

3.1.5 *Experimental Design and Analysis of Observational Data*

We performed several 1-D simulations to investigate and delineate the effects of ABL modeling errors (1) the effects of uncertainty in soil moisture availability, (2) the variability due to different mixed-layer

formulations, (3) the effects of horizontal advection of temperature, and (4) the variability due to different mixed-layer height calculations. Two additional experiments (5 and 6) were performed to test a new technique for assimilation of surface data in the ABL (test 5) and the combined effect of the data assimilation and change in the soil moisture availability (test 6). For these simulations we used the observational data from two field experiments, the SJVAQS (Blumenthal et al. 1993), and the **F**irst **I**nternational Satellite Land Surface Climatology Project (ISLSCP) **F**ield **E**xperiment (FIFE) (Sellers et al. 1992). All numerical experiments were begun shortly after sunrise and ran for 13 h. A brief analysis of the observational data is given below.

3.1.5.1 Analysis of Buttonwillow, CA, Observational Data

From the SJVAQS, we selected observational data for Buttonwillow, CA ($35^{o}24^{'}47^{''}$ N, $119^{o}28^{'}20^{''}$ W) in the southern SJV. These data include vertical profiles of eastward and northward winds, virtual potential temperature, and water vapor mixing ratio for various times throughout the day starting from 0700 PDT 3 August 1990. These profiles are shown in Fig. 1. The wind profiles (Figs. 1a and 1b) from 0700 to 1900 PDT indicate that the top of the ABL appears to be around 1200 m. Both wind components show vertical wind shear, indicating that the ABL may not have well-mixed layers, even during convective conditions. The virtual potential temperature (Θ_v) profile (Fig. 1c) does not vary much between 0700 and 1000 PDT. Notice that the Θ_v profile at 1300 PDT indicates warming of the atmosphere from the surface to the 2000 m altitude, even though there is a negligible vertical gradient only up to ~500 m altitude. The presence of warming in the layers above 500 m (the approximate top of the ABL at this time) may be due to either adiabatic sinking of the air mass associated with the east Pacific high-pressure system or advection of warmer air into this region below 2000 m. By 1600 PDT, the top of the ABL seems to have grown to around 1000 m altitude, as indicated by the Θ_v profile. Again, the effect of a large-scale process can be seen in the 1600 PDT profile farther aloft, although more weakly than before. By 1900 PDT, the mixed layer has grown to about 1200 m before stabilizing due to sensible heat flux divergence at the surface an hour or so before sunset. It also can be seen that the capping inversion above the CBL is rather weak in the afternoon observed soundings. Vertical variations in the mixing ratio of water vapor (Fig. 1d) also indicate, in general, the presence of unmixed layers in the ABL throughout the observational period.

In summary, the maximum depth of the ABL at Buttonwillow appears to reach about 1200 m during the late afternoon on this day. The temperature is well mixed, but the winds and water vapor mixing ratio are not. There is a warming in the layers above the daytime ABL, especially between 1000 and 1300 PDT, with a weak afternoon capping inversion. Obviously, simulating these kinds of ABL structures using a 1-D model is difficult. However, we consider this case to delineate how uncertainties in different processes affect the ABL structures and to study the effect of data assimilation in the ABL.
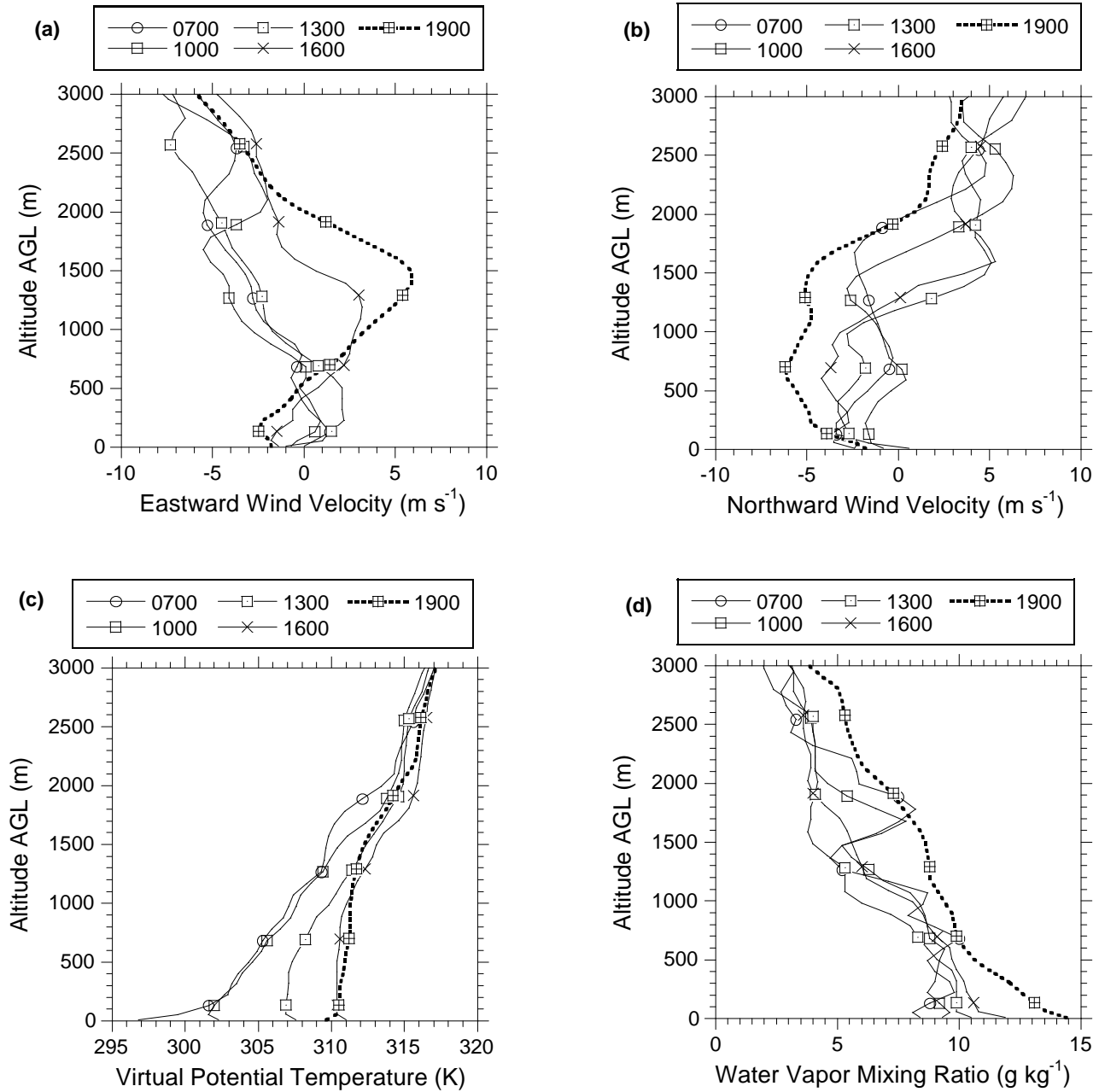
Figure 1. Temporal variation of "observed" (a) eastward wind velocity, (b) westward wind velocity, (c) virtual potential temperature, and (d) water vapor mixing ratio at the Buttonwillow, CA for 3 August 1990 during SARMAP. All times in legends are PDT.

3.1.5.2   Analysis of FIFE Data

We also considered a data set from the FIFE measurements made on a "Golden Day" (i.e., a period during which turbulent mixing processes are the only dominating mechanism in the ABL). Initial meteorological conditions (0700 LT 6 June 1987) over the FIFE site in Manhattan, KS, indicated the presence of remnants of a nocturnal low-level jet located about 500 m above ground level (not shown). Up to about 500 m AGL, the water vapor mixing ratio showed very weak vertical gradients in this case. Virtual potential temperature indicated stable lapse rates particularly below 700 m altitude. Observations at later time periods during the daytime evolution revealed that the nocturnal jet had dissipated, leading to uniform winds within the ABL. Observed water vapor mixing ratio and virtual potential temperature profiles at intervals during the daytime indicated the presence of well-mixed layers in the ABL. A more detailed description can be found in Alapaty et al. (1997a,b).

3.1.6 Effect of Uncertainty in Soil Moisture Availability

In the SARMAP mesoscale meteorology study over California, Seaman et al. (1995) found that the simulated daytime maxima of the surface air temperatures (35 m AGL) during the 2-7 August 1990 episode were about 1-2 K warmer than in the observations (2 m AGL). Superadiabatic lapse rates are commonly present in the surface layer during convective conditions over land, so the projection of model-predicted temperatures at 35 m AGL to an altitude of 2 m AGL would likely yield even higher simulated surface temperatures. Because surface-layer temperature fields are not assimilated in the simulations, prediction errors for the surface-layer temperatures potentially can be linked to uncertainty in the soil moisture availability parameter.

For example, Alapaty et al. (1995) used a hydrostatic 3-D model, the MM4 (Anthes et al., 1987), to provide meteorological (winds and thermodynamic) information to the U.S. Environmental Protection Agency's Regional Oxidant Model (ROM). The modeled domain covered the eastern United States and simulations were performed for the period July 29-August 5, 1988, during which much of the region was under a severe drought. In these simulations, Blackadar's nonlocal-closure scheme was used to represent the CBL mixing processes along with default moisture availabilities for climatologically average summer conditions. They then compared the MM4-generated mixed-layer depths and those obtained by analyzing the standard observations for the eight days. It was found that area-averaged mixed-layer depths over different regions of the eastern United States were underpredicted in MM4 by as much as 50% compared to the diagnostically determined mixed-layer depths. They also found that surface temperatures were underpredicted for the entire simulation period and concluded that the default soil moisture availability (M_a) used in the experiment was not appropriate for the drought conditions. This positive feedback between soil moisture modulations in sensible heating and ABL depths has been confirmed in many other studies (e.g., Niyogi et al. 1997, 1999).

In the agricultural and grazing regions of central California, the vegetation (excluding irrigated farmland) is under high water stress during most of the summer months. For example, virtually no rainfall occurred over the San Joaquin Valley and Coast Ranges during the SARMAP episodes, while only a few showers occurred over the high ridges of the Sierras. Hence, the SARMAP case of 2-7 August 1990 provides an opportunity to study the interactive role of soil moisture uncertainty for central California and its surrounding regions. For this purpose we performed several 1-D model simulations to study how variations in soil moisture availability affected the ABL depth in the SJV, as described in the sections below.

3.1.6.1 Simulation of ABL Structure over Buttonwillow, CA (SARMAP Case)

In their SARMAP study, Seaman et al. (1995) used soil moisture availability values for each land use type that were reduced to half of those generally used in the MM5 (Grell et al. 1994) because of the extreme dryness of the SJV during the summer. In the present analysis, we believe that this kind of uniform reduction of moisture availability across all land use types is unlikely to be optimal. For example, in an observational study of the SJV, Pederson et al. (1995) found maximum latent heat fluxes to be about 400 W m^{-2} for some of the observation sites. Thus, we believe that soil moisture availability values may need to be more carefully selected for the SARMAP region while recognizing that nonirrigated vegetation in California and surrounding regions remains under high water stress.

To study the effects of soil moisture uncertainties on the structures of the ABL, we performed two numerical simulations with the 1-D model utilizing the observational data available for the Buttonwillow site (a site in the southwest SJV dominated by grasslands). The starting time of the simulations is 1400 UTC/0700 PDT 3 August 1990. In these simulations we used the ACM to represent convective mixing in the ABL and the BKT scheme to represent diffusion/mixing processes during the nonconvective conditions in the ABL as described earlier. In the first simulation (referred to as "SMA1"), the soil moisture availability value used in the study of Seaman et al. (1995) was considered (M_a=0.075). The second simulation (referred to as "SMA2") used the standard value of soil moisture availability generally used in the MM5 for summertime agricultural land (M_a=0.15). Figures 2a and 2b show the temporal variation of modeled turbulent sensible and latent heat fluxes in the SMA1 and SMA2 cases. Because the SMA1 soil moisture availability is lower than the SMA2 value by exactly half, latent heat fluxes are larger in SMA2 by about 200 W m^{-2}. Consistent with this response, turbulent sensible heat fluxes are reduced in the SMA2 by about 100 W m^{-2} (Fig. 2a). Predicted virtual potential temperature (Θ_v) profiles at 1600 PDT in SMA1 and SMA2, together with the Θ_v observations, are shown in Fig. 2c. In SMA2, the predicted Θ_v below 1000 m altitude is closer to the observations, while the SMA1 Θ_v is warmer by about 2 K. Notice that surface-layer temperature is well predicted in SMA2 even though the depth of the ABL remains overpredicted (as indicated by the simulated inversion just above 1700 m). The estimated maximum depths of the boundary layer (Fig. 2d) in SMA1 and SMA2 are about 2200 and 1750 m, respectively; this difference reflects the effects of increased soil moisture availability. Additionally, simulated mixing ratio profiles (not shown) followed the variations in the latent heat fluxes, with SMA2 having higher values than SMA1. These results are consistent with those reported in Alapaty et al. (1997b).

Clearly, the observed maximum depth (~1200 m at 1900 PDT) of the ABL for Buttonwillow was not captured in either SMA1 or SMA2. In addition, the mixed-layer depth in these experiments is much greater than that simulated by Seaman et al. (1995) for the Buttonwillow
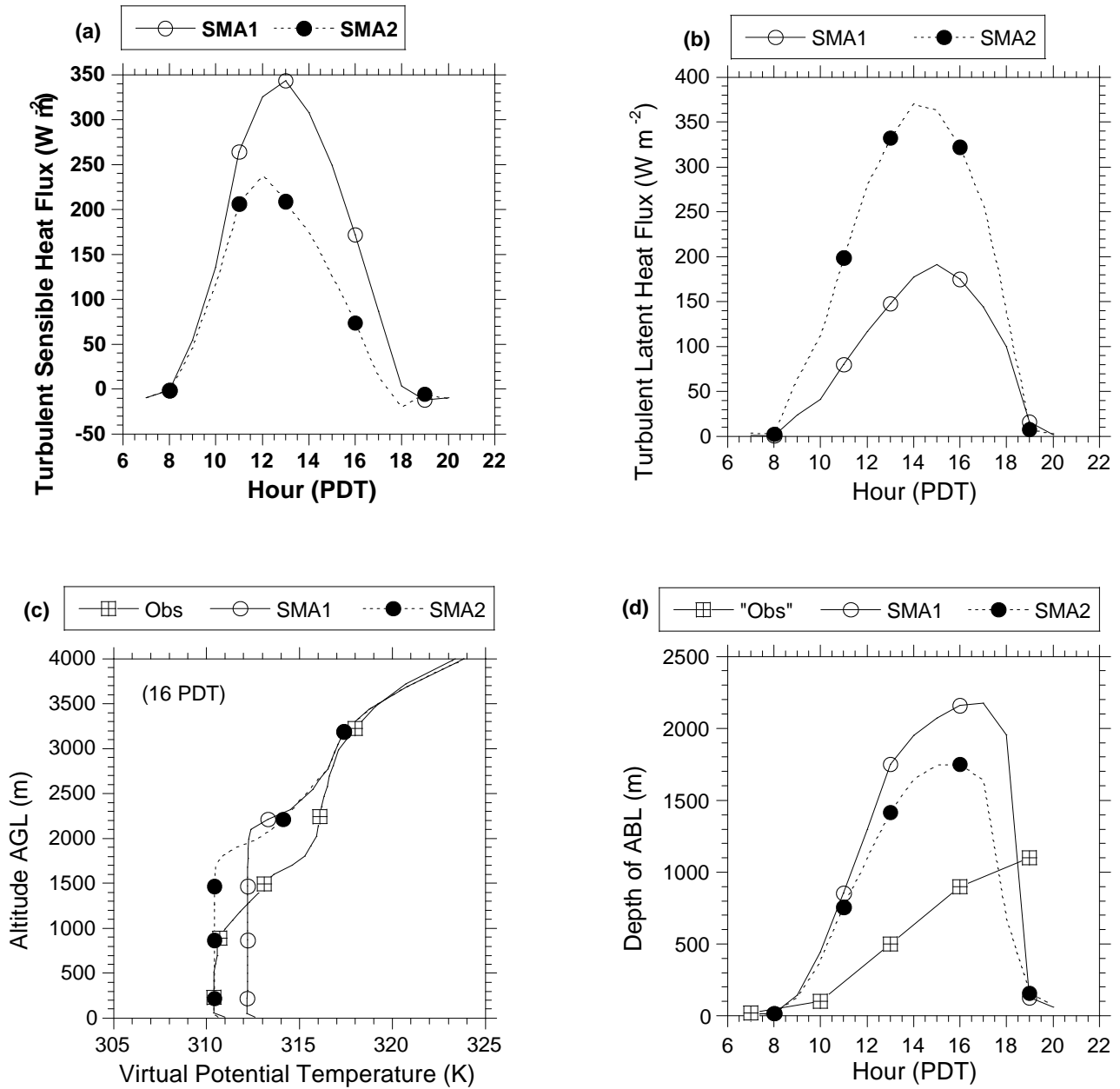
Figure 2. Effects of uncertainty in the specification of soil moisture availability for the SARMAP case: Temporal variation of (a) predicted turbulent sensible heat flux, (b) predicted turbulent latent heat flux, (c) predicted and observed virtual potential temperature at 1600 PDT, and (d) predicted depth of the ABL.

case, in the same episode. However, comparing SMA2 and SMA1 results shows that the soil moisture variability is a critical factor for improving model performance. To further explore the impact of soil moisture variability, we performed additional 1-D simulations using observational data from the FIFE site. Note that from here onwards, SMA1 is also referred to as the control run.

### 3.1.6.2 Simulation of ABL Structure over Manhattan, KS (FIFE Case)

The FIFE site was located near Manhattan, KS, covering a 15×15-km area where tall grass prairie was the predominant vegetation. We selected measurements from 6 June 1987, one of the five FIFE intensive field campaigns (Sellers et al. 1992), for the model simulations. During this intensive observing period, special efforts were made to measure various meteorological, hydrological, and biophysical parameters. This particular day was characterized by almost-clear sky and weak advection conditions, so boundary layer processes dominated the atmospheric profile. We performed three simulations using the 1-D model for 13 h starting from 1200 UTC 6 June 1987. These three cases utilized two different latent heat flux formulations:

FSMA1:   The soil moisture availability was reduced by 50 % as in SMA1 (control run) in Section 3.1.6.1

FSMA2:   The soil moisture availability was the same as that used in SMA2 in Section 3.1.6.1

FNPJ: An interactive soil-vegetation parameterization suggested by Noilhan and Planton (1989) and Jacquemin and Noilhan (1990) was used

In all of the above simulations, we again used the ACM-BKT scheme to represent the CBL mixing. The temporal variation in the predicted and observed fluxes of sensible and latent heat are shown in Figures 3a and 3b, while profiles of the predicted and observed virtual temperature at 17 CDT are shown in Figure 3c. Observed heat fluxes, available at 30-min intervals, were estimated using the eddy correlation (covariance) method. Sensible heat fluxes in SMA1 are the highest, while those obtained in FNPJ and FSMA2 are closer to the observations. An opposite trend can be seen with the latent heat fluxes (Fig. 3b), where fluxes are highest in FNPJ and lowest in FSMA1. The much larger values of observed surface latent heat flux (relative to the sensible heat flux) for 6 June 1987 (Bowen ratio about 0.3) are consistent with the improvement of the model results in FSMA2 versus FSMA1. In fact, the data strongly suggest that the optimal moisture availability for this case should be more moist than the MM5 summer default value for agricultural land used in FSMA2. Similarly, FNPJ and FSMA2 provide better predictions of the virtual potential temperature, compared to FSMA1; as an example, we show the model predictions at 17 CDT (Fig. 3c). The observed depths of the ABL were obtained from SODAR measurements and are compared with the respective modeled values (Fig. 3d). Again, FNPJ and FSMA2 give better predictions of ABL depths. Note that in all the experiments a warmer boundary layer is simulated than exists in the observations, which is related to the overprediction of the sensible heat fluxes when the moisture availability is too low. Consistent with the SARMAP case, these results also confirm that modulating surface characteristics such as the soil moisture can lead to improved simulation results.
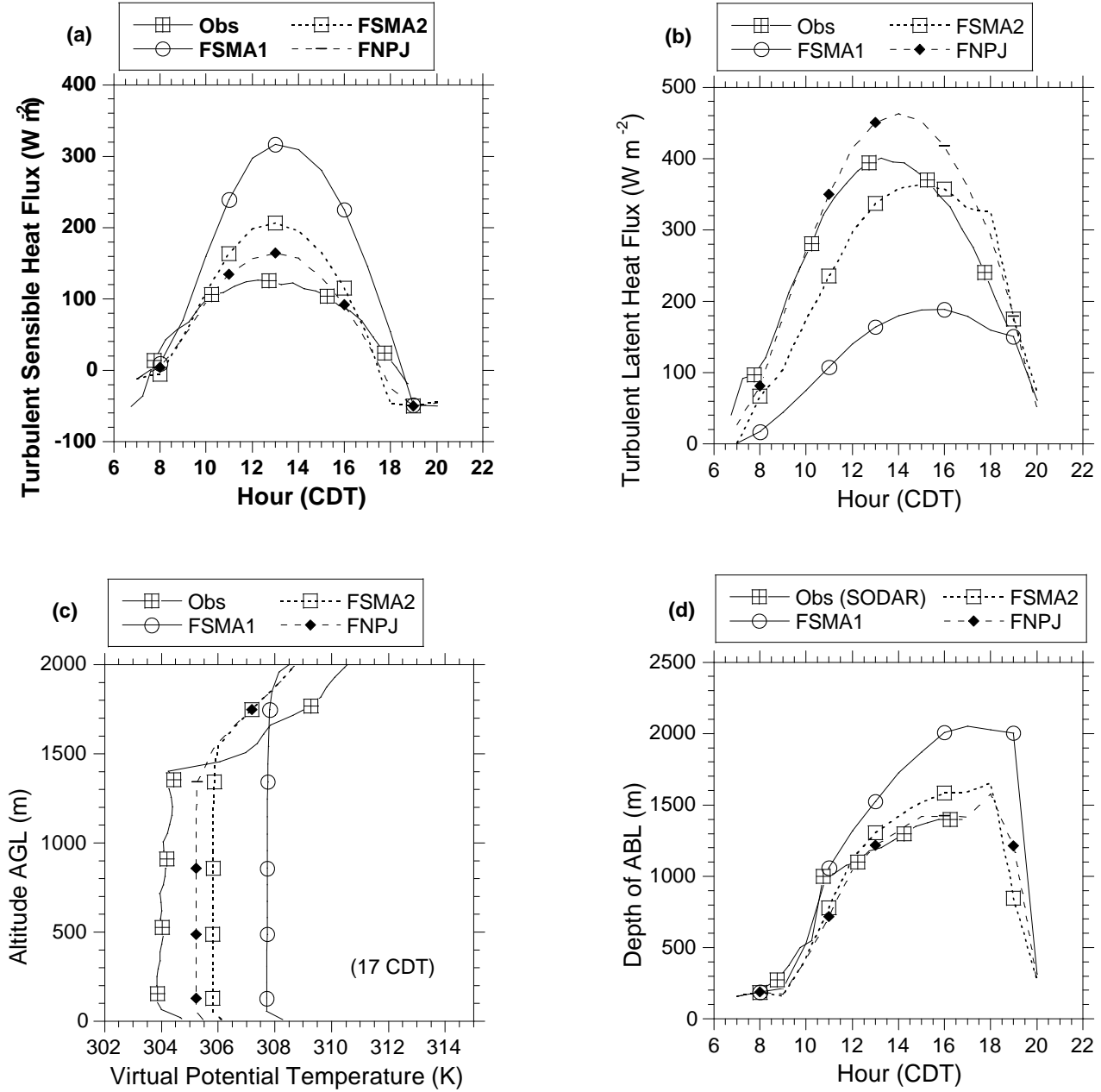
Figure 3. Evaluation of turbulent latent heat flux formulations for the FIFE case: Temporal variation of predicted and observed (a) turbulent sensible heat flux, (b) turbulent latent heat flux, (c) virtual potential temperature at 1600 PDT, and (d) depth of the ABL.

Note that direct measurements of several surface characteristics required for use in the FNPJ (or to adjust soil moisture for departures from seasonal climatology in the case of MM5) are available for the FIFE site for only a short period, and such measurements are not routinely available in most regions for use in a 3-D model. Thus, ABL modeling errors due to soil moisture uncertainty can be large. Methods similar to that proposed by Alapaty and Niyogi (1999) can help reduce these types of errors. And as pointed out by Ruggiero et al. (1996), surface-layer data assimilation also can help to minimize such ABL modeling errors.

3.1.7 Effects of Using Different Mixed-Layer Formulations

Dynamic and thermodynamic profiles within the ABL result from the complex interactions among surface heating, buoyant plumes, shear across the boundary layer, and entrainment in the interfacial layer. Prediction errors may arise from the uncertainty present in the prescribed constants and/or assumptions related to the simplification of the turbulence closure problem. Seaman et al. (1995) found that using a turbulent kinetic energy (TKE) scheme instead of Blackadar's nonlocal-closure scheme resulted in a slight improvement in predicted ABL depths. However, in their TKE scheme, dissipation of TKE was obtained diagnostically. In our case study, we used a TKE scheme (referred to as the E-ε scheme, described in Section 3.1.4.1) in which dissipation of TKE is prognostically determined (e.g., Alapaty et al.1997b). We performed one numerical simulation using the E-ε scheme and a second simulation using the ACM-BKT scheme to study the effects of mixed-layer formulation on ABL structure; Buttonwillow, California observational data and the soil moisture values used in SMA1 were utilized in both simulations.

Figures 4a and 4b show the temporal variation in sensible and latent heat fluxes as predicted by the E-ε and ACM-BKT schemes. Sensible heat fluxes in both simulations are very similar until the afternoon, when the E-ε scheme predicts sensible fluxes about 40 W m^{-2} higher than those from the ACM-BKT scheme. Latent heat fluxes from the ACM-BKT scheme show a compensating increase compared to the E-ε scheme fluxes. Although the afternoon sensible heat fluxes are higher with the E-ε scheme, the predicted maximum depth of the ABL (Fig. 4c) is lower than with the ACM-BKT scheme.

There are several reasons for greater growth of the ABL with the ACM-BKT scheme despite weaker fluxes of sensible heat. First, in the ACM-BKT scheme the depth of the ABL depends directly on the surface layer's virtual potential temperature (a warmer surface layer therefore leads to a deeper boundary layer). Second, it has been found (Pleim and Chang 1992, Alapaty et al. 1997b) that the nonlocal mixing in the ACM-BKT scheme causes a rapid erosion of temperature inversion, leading to faster growth of the ABL; this is clearly evident near noon in Fig. 4c. Also, a deeper ABL entrains potentially warmer air into itself, leading to further warming. In the ACM-BKT scheme the calculation of sensible heat flux depends on the temperature gradient across the surface, thus a warmer surface layer leads to lower sensible heat fluxes. Finally, the ABL collapses about an hour earlier in the evening with the ACM-BKT scheme than with the E-ε scheme. This result agrees with Shafran et al. (2000), who noted that a mixing depth diagnosed as a function of the surface-layer virtual potential temperature stabilizes soon after the surface sensible heat flux becomes negative in the late afternoon, even though turbulent mixing may continue for some time.
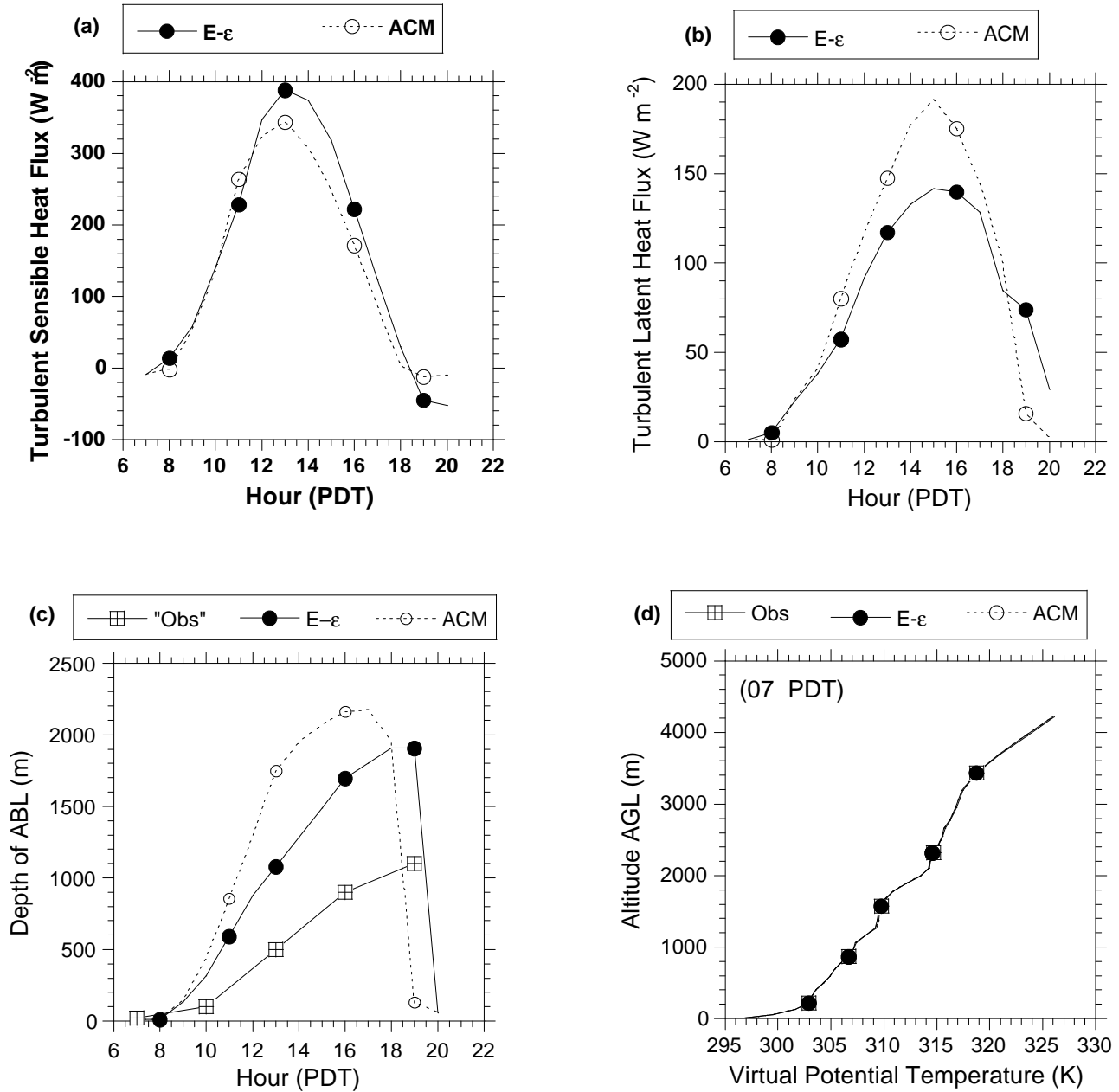
Figure 4. Effects of turbulent mixing formulations for the SARMAP case: Temporal variation of (a) predicted turbulent sensible heat flux, (b) predicted turbulent latent heat flux, (c) predicted depth of the ABL, and (d) predicted and observed virtual potential temperature at 0700 PDT. "ACM" in the legends is short for "ACM-BKT".

The vertical profiles of virtual potential temperature predicted by the E-ε and ACM-BKT schemes are shown together with corresponding observations in Figs. 4d through 4h. The conditions at 0700 PDT shown in Fig. 4d indicate the presence of a stable boundary layer. At 1000 PDT (Fig. 4e), the CBL has not grown above 150 m altitude in either the observations or the simulations. As described earlier, the observed atmospheric layers between 600 and 2000 m were warmed, probably by one or more large-scale processes between 1000 and 1300 PDT (Fig. 1), but these 3-D processes are not modeled in this simulation. Therefore, predicted mean ABL potential temperatures at 1300 PDT (Fig. 4f) indicate well-mixed layers in both the E-ε and ACM-BKT simulations that are deeper than observed, even though the temperatures below 200 m in the E-ε experiment nearly match the observed temperatures. Note that the ACM-BKT scheme predicts a warmer and deeper ABL throughout the afternoon, relative to the E-ε scheme (Figs. 4g and 4h). In general, then, the E-ε scheme shows relatively better agreement with the observed surface-layer temperatures than does the ACM-BKT scheme.

3.1.8 Role of 3-D Processes on Temperature

The near-stationary summertime East Pacific Ridge is often associated with the large-scale circulations that lead to subsidence and adiabatic heating of the air over California. This compressional heating, which is greatest in the first few kilometers above the ground, contributes to stable inversion conditions and can suppress the growth rates of the ABL. The general effect of this heating is replicated in the 1-D model by specifying a positive temperature tendency profile in the atmospheric column. Analysis of the lower troposphere temperature data indicated a warming of the atmosphere of about 4 K between 600 m and 2000 m AGL from 0700 to 1600 PDT 3 August 1990. Therefore, we specified an equivalent warming contribution to the tendency profile, using a heating rate at 600 m AGL that decreased linearly with height to zero at 2200 m altitude. Two numerical simulations were performed using the E-ε and ACM-BKT schemes to study how subsidence-like heating affects ABL growth. These simulations are referred to as "HADV."

Figure 5a shows the modeled sensible heat fluxes in SMA1 (control run) and HADV with both the E-ε and ACM-BKT schemes. The addition of the specified subsidence-like warming led to slightly reduced sensible heat fluxes and a corresponding small increase in the latent heat fluxes (Fig. 5b) in HADV. Consistently, the mean virtual potential temperature of the ABL (Fig. 5c) in HADV indicates 1.5 to 2 K warmer temperatures than in SMA1, mostly due to entrainment of the warmer mid-level air. The mid-level warming resulted in marginally lower boundary layer depths compared to those in SMA1 (Fig. 5d) with both the E-ε and ACM-BKT schemes. This is because turbulent mixing in HADV is weaker than in SMA1, leading to slightly shallower boundary layers.

3.1.9 Variability Due to Different Mixed-Layer Height Calculations

When applying the ACM-BKT scheme, we used two different methods to calculate the depth of the ABL. The first method is the same as that used in the MM5: the ABL depth is defined as the altitude at which the virtual potential temperature of the air becomes the same as that of the air in the surface layer. The second method is based on the bulk Richardson number criterion
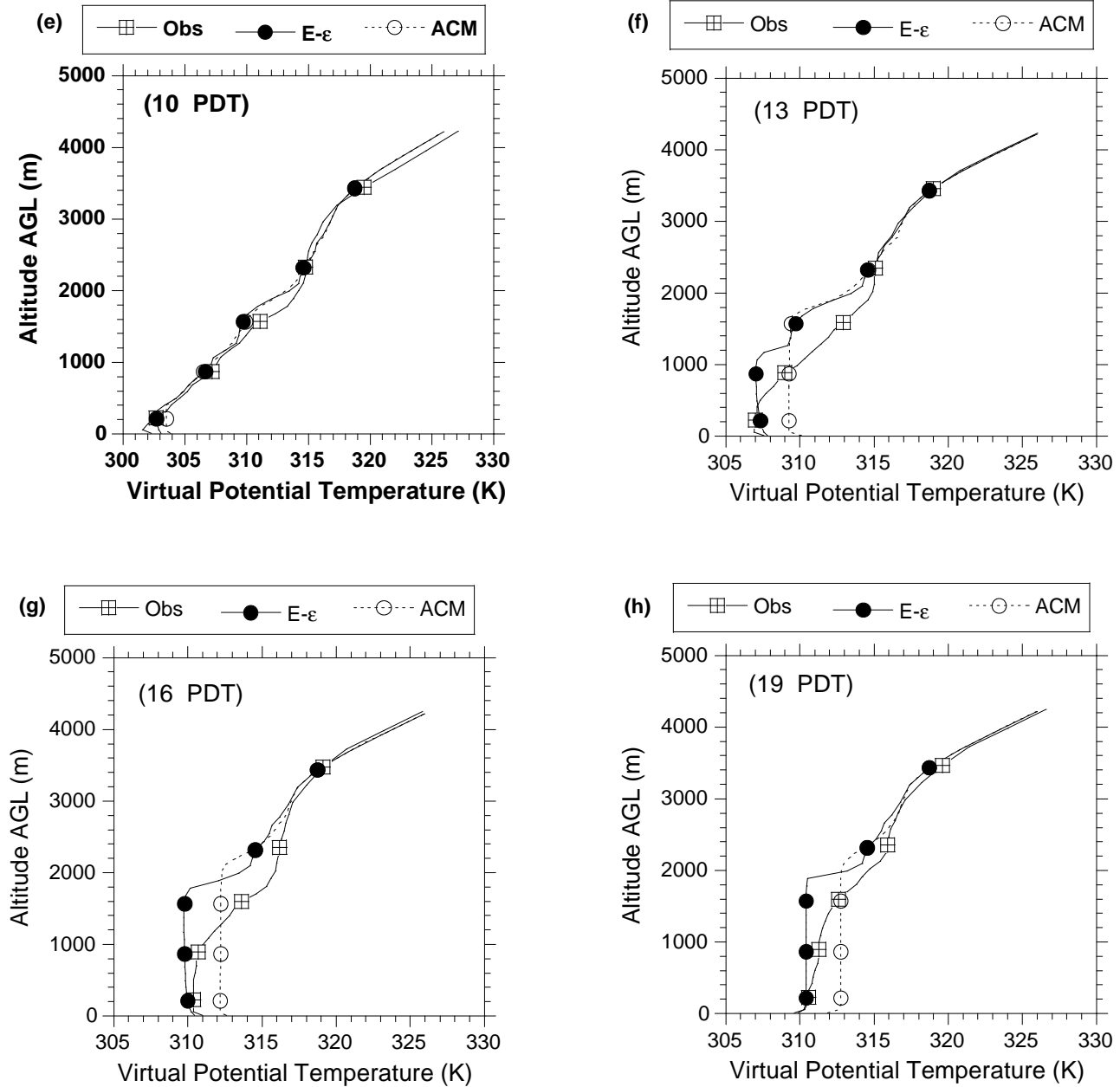
Figure 4 (contd.). Effects of turbulent mixing formulations for the SARMAP case (continued): Temporal variation of predicted and observed virtual potential temperature at (e) 1000 PDT, (f) 1300 PDT, (g) 1600 PDT, and (h) 1900 PDT.
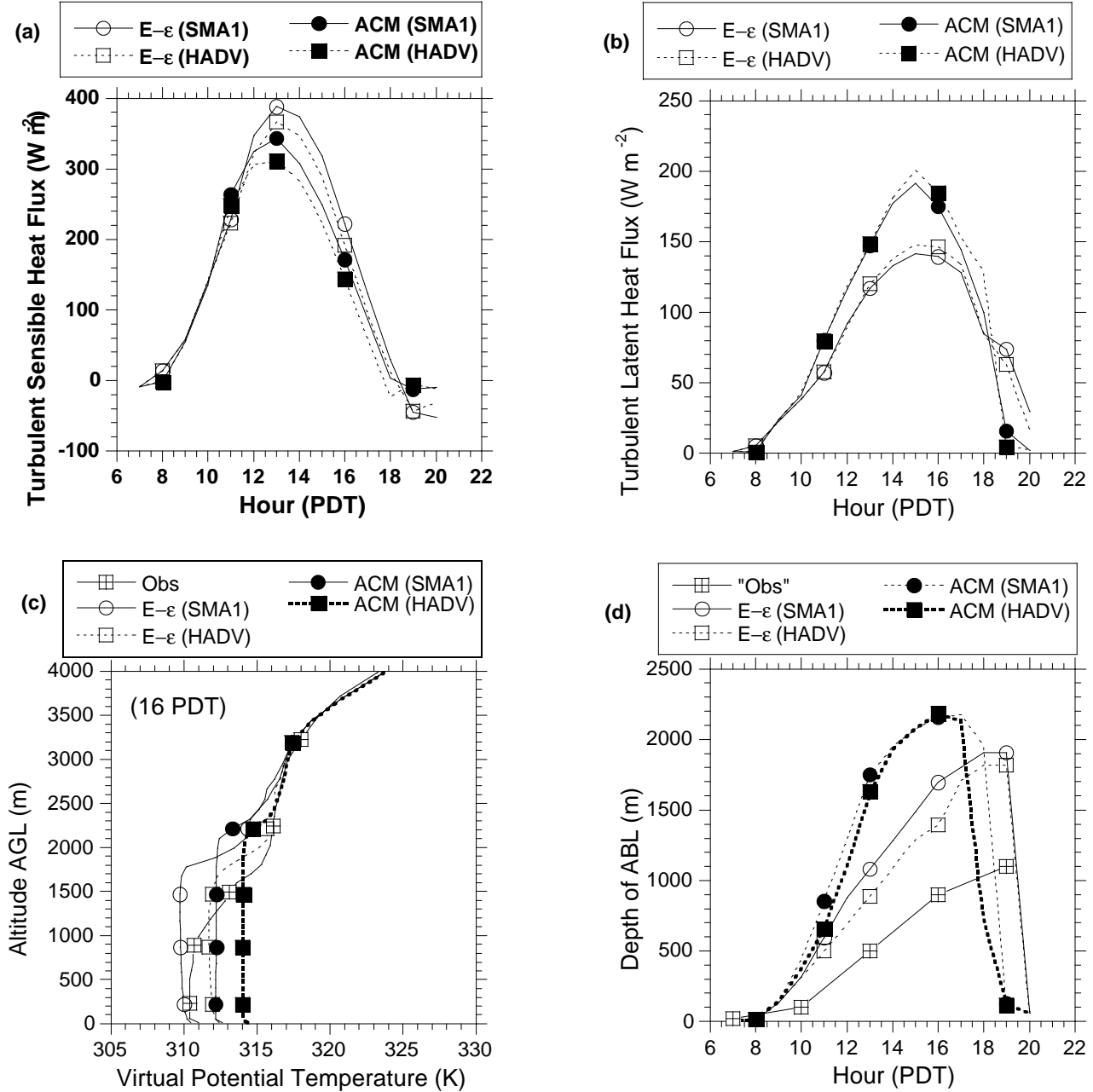
Figure 5. Effects of horizontal advection of warm air in the SARMAP case: Temporal variation of (a) predicted turbulent sensible heat flux, (b) predicted turbulent latent heat flux, (c) predicted and observed virtual potential temperature at 1600 PDT, and (d) predicted depth of the ABL. "ACM" in the legends is short for "ACM-BKT".

suggested by Holtslag et al. (1990). In this method, the bulk Richardson number (R_{ib}) is calculated for every model level, always starting from the lowest level. Then the vertical level at which the R_{ib} exceeds the critical Richardson number (0.25) is diagnosed to be the top of the mixed layer. The bulk Richardson number can be written as

$$R_{ib} = \frac{gz\left[\Theta_v(z) - \Theta_{vs}\right]}{\overline{\Theta_v}\left[u^2(z) + v^2(z)\right]} \tag{15}$$

where z is the altitude, Θ_v is the virtual potential temperature at that altitude, Θ_{vs} is the virtual potential temperature of the surface layer, $\overline{\Theta_v}$ is the average of the virtual potential temperature of the surface layer and a layer at altitude z, and u and v are the eastward and northward components of the horizontal wind. For example, if R_{ib} for levels 15 and 16 are 0.31 and 0.18 respectively, then the ABL top lies in between the altitudes of these two levels. Since the altitudes of all model levels are known, we linearly interpolate the height field at which R_{ib} is exactly 0.25. This linearly interpolated height is considered to be the height of the ABL above ground level.

As stated earlier, Seaman et al. (1995) found that assimilation of surface-layer data is difficult with Blackadar's nonlocal-closure scheme. This is because the calculation of the ABL depth in this scheme relies directly on the surface-layer temperature (the first method described above); any change in the surface-layer temperature due to data assimilation often resulted in dramatic spurious changes in the depth of the ABL. The alternative Holtslag et al. (1990) formulation for ABL depth is attractive for alleviating this problem because it does not emphasize a dependence on surface temperature, but instead relies on the nonlocal difference in the virtual potential temperature and vertical wind shear.

We performed numerical simulations to delineate the effects of using these two diagnostic methods for calculating ABL depth. In Fig. 6, simulation results from Holtslag's method are designated "HOLTSLAG" while the results obtained from SMA1 are designated "MM5-ACM-PBLHT." Figures 6a and 6b, which show the estimated sensible and latent heat fluxes, reveal only marginal differences between the two techniques. Figure 6c shows that the differences in the virtual potential temperature profiles predicted by the two methods are also minor. Figure 6d shows that the diagnosed ABL depths from the two methods are only marginally different. Overall, Hotlslag's formulation estimates a slightly deeper boundary layer than the method used in the Blackadar PBL in MM5. This is because the ACM scheme, in general, (1) simulates weak superadiabatic lapse rates in the surface layer (as does the Blackadar scheme), leading to ABL depth estimates similar to those from other methods that define the altitude of the temperature inversion's base as the depth of the ABL; and (2) does not account for the turbulent mixing due to vertical wind shear in the ABL**.** These two factors are implicitly taken into account by Holtslag's method, which typically calculates the top of the boundary layer in the neighborhood of the top of the interfacial (inversion) layers.
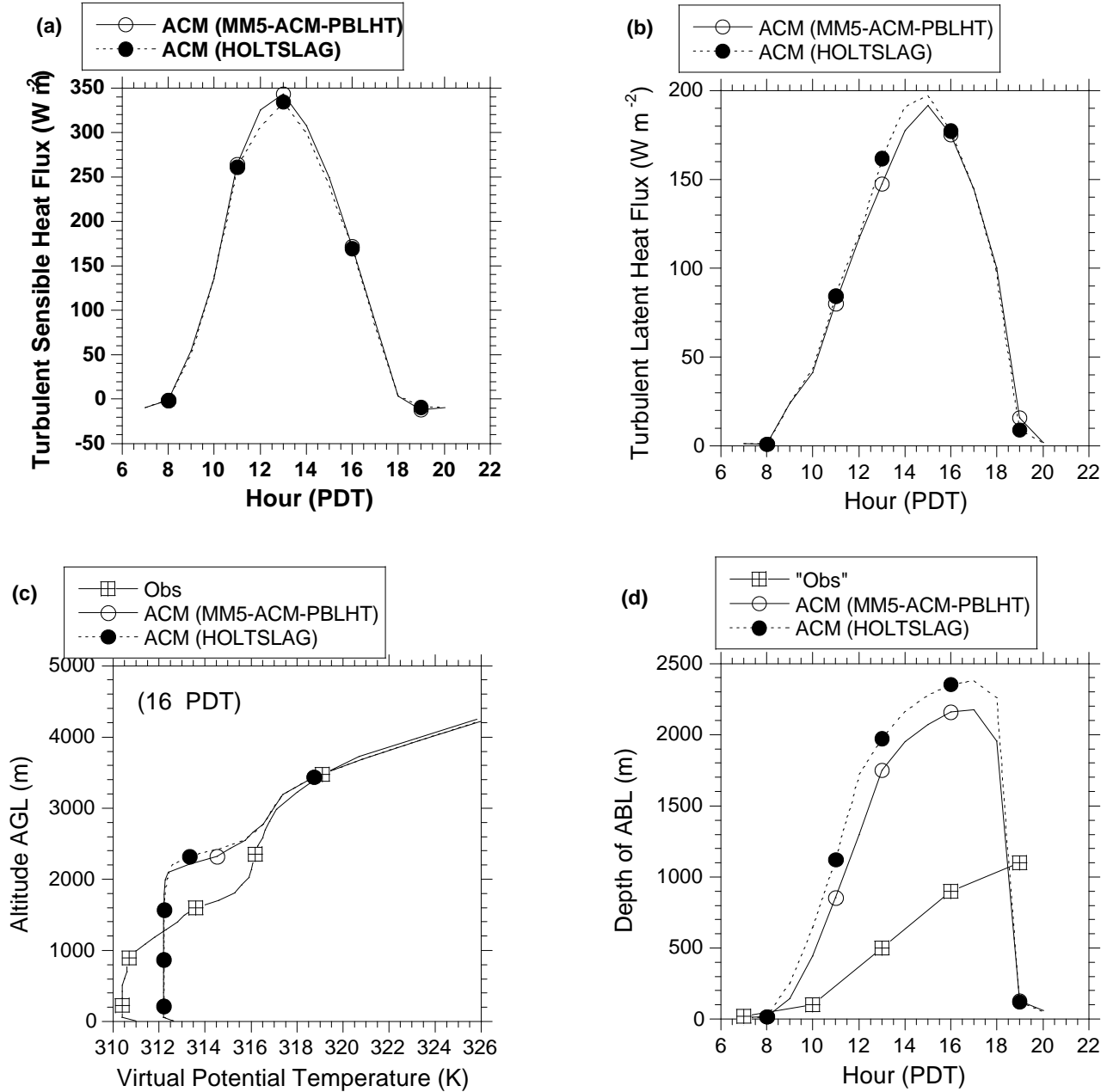
Figure 6. Effects of mixed-layer depth calculation formulations for the SARMAP case: Temporal variation of (a) predicted turbulent sensible heat flux, (b) predicted turbulent latent heat flux, (c) predicted and observed virtual potential temperature at 1600 PDT, and (d) predicted depth of the ABL. "ACM" in the legends is short for "ACM-BKT".

3.2 Development and Testing of New Techniques to Improve the Mixed-Layer Depths Estimations

The results in the previous sections indicate that, even for 1-D processes, considerable errors can be caused by uncertainties in parameter settings and formulations. These problems can be alleviated by improving the existing formulations and also by making use of surface observations in the data assimilation techniques. We present here two new methodologies that can help reduce errors in the estimated mixed-layer depths. The first is a method to assimilate surface data without damaging representation of ABL features. The second is a technique to improve prediction of latent heat flux by implicitly including evapotranspiration from both soil and vegetation.

3.2.1 Surface Data Assimilation Technique

In this section we describe a nudging technique that can reduce errors in surface flux estimates by assimilating surface observations into the model solutions. The modeling study of Seaman et al. (1995) indicated that four-dimensional data assimilation (FDDA) of surface-temperature data could reduce model errors because predicted ground/skin and surface-layer temperatures control turbulent heat fluxes in the CBL. However, their study further concluded that assimilation of surface-temperature data is difficult using Blackadar's nonlocal-closure scheme because (1) the estimated mixed-layer depths are directly linked with surface-layer temperatures, and (2) computation of mixing rates is based on the temperatures of the lowest two layers. Thus, any error in adjusting the surface temperature when using Blackadar's scheme can directly influence the depth of the mixing layer as well as the mixing within it. The approach we took was to assimilate the observational data and adjust the temperature and mixing ratio in the surface layer accordingly. In doing this we also simplified the data assimilation procedure used in MM5. To maintain consistency we then calculated the fluxes that would be needed to effect that rate of change in surface temperature and humidity and then adjusted the ground skin temperature to be consistent with the revised rates of sensible and latent heat fluxes.

Description of Technique

To nudge prognostic variables in the ABL and the free atmosphere in our 1-D model, we simplified the FDDA scheme used in the MM5 (Seaman et al. 1995). Furthermore, we converted changes in temperature and water-vapor mixing ratio caused by the assimilation of surface-layer data to the respective fluxes for use in adjusting the ground/skin temperature, so that the air temperature and water vapor mixing ratio are consistent. This new procedure not only maintains the thermodynamic balance but may also provide an improved ground temperature prediction. Following the data assimilation procedure that is used in the 3-D version of the MM5 (Stauffer and Seaman 1990), a simplified assimilation formulation for use in 1-D models can be written as

$$\frac{\partial a}{\partial t} = F(a, s, t) + G_a(\hat{a} - a) \tag{16}$$

where α is a prognostic variable for which observations are available, t is time, F is the forcing term representing the effects of all physical processes modeled in the single column model, σ is the vertical coordinate, G_α is the nudging factor (magnitude) for α, and $\hat{a}$ is an analyzed value obtained from observations for α. For more details, refer to Stauffer and Seaman (1990).

The proposed adjustment of the ground/skin temperature due to the assimilation of surface data needs further explanation. For brevity, consider the assimilation of surface-layer temperature. Let $\partial T_S^F / \partial t$ be the rate of change of the surface-layer temperature due to nudging. Then the turbulent sensible heat flux, H_S^F (W m^{-2}), required to change the surface-layer temperature in a time interval Δt by ($\partial T_S^F / \partial t \bullet \Delta t$) due to nudging can be written as

$$H_S^F = \rho C_p \left(\partial T_S^F / \partial t \bullet \Delta t \right) \frac{\Delta z}{\Delta t} = \rho C_p \left(\partial T_S^F / \partial t \right) \Delta z \tag{17}$$

where ρ is the density of the air in the lowest layer of the model, C_p is the specific heat of air at constant pressure, and Δz is the thickness of the lowest model layer. Similarly, if $\partial q_S^F / \partial t$ is the rate of change of the surface-layer water vapor mixing ratio due to nudging, then the turbulent latent heat flux, H_λ^F (W m^{-2}), required to change the surface-layer mixing ratio in a time interval Δt by ($\partial q_S^F / \partial t \bullet \Delta t$) due to nudging can be written as

$$H_\lambda^F = \rho L \left(\partial q_S^F / \partial t \bullet \Delta t \right) \frac{\Delta z}{\Delta t} = \rho L \left(\partial q_S^F / \partial t \right) \Delta z \tag{18}$$

where L is the latent heat due to condensation. Because direct ground/skin temperature observations are not generally available (unless they are estimated from clear-sky surface radiances), the above relationships were used to adjust the ground temperature tendency. The adjusted tendency of ground/skin temperature including the assimilation of surface-layer temperature and moisture can be written as

$$C_g \frac{\partial T_g}{\partial t} = R_n - H_m - H_s - H_\lambda - H_s^F - H_\lambda^F \tag{19}$$

where C_g is the thermal capacity of the soil slab per unit area, R_n is the net radiation reaching the ground, H_m is the soil heat flux, H_s is the turbulent sensible heat flux, and H_λ is the turbulent latent heat flux. This procedure can be extended to any 3-D model, making assimilation of surface observations (temperature and water vapor mixing ratio) feasible in a meteorological model.

### *Testing of Data Assimilation Technique*

We tested the data assimilation technique using special observational data. The data available at 3-hour intervals were interpolated in time and height to the model layers. Here we present the results of experiments that include (1) assimilation of temperature, wind, and water vapor mixing ratio data for the ABL and the free atmosphere; and (2) physically consistent adjustment of skin/ground temperature. The weights used for nudging were the same as the standard values used in the MM5 (Grell et al. 1994). Special observational data (winds, temperature, and mixing ratio) available at 3-hour intervals at Buttonwillow,California, were interpolated to the 1-D model's vertical layers. These data were then linearly interpolated in time for every model time step at all layers for use in the continuous assimilation scheme. Results obtained using the data assimilation scheme are shown in Figs. 7a through 7h; we refer to this case as "FDDA."

Figures 7a and 7b show the sensible and latent heat fluxes predicted in SMA1 (control run) and in FDDA using the E-ε and ACM-BKT schemes. As a result of data assimilation, sensible heat fluxes in FDDA are lower than in SMA1 with both of the ABL schemes. Estimated latent heat fluxes (Fig. 7b) in FDDA with the E-ε and ACM-BKT schemes are very close to each other and both are significantly less than in SMA1. Thus, the effect on the surface latent heating is not simply a "mirror image" of the response to changes in sensible heating as found in the earlier experiments. The assimilation technique dramatically reduced the predicted depths of the ABL with both ABL schemes (Fig. 7c). However, compared to the ACM-BKT, the E-ε scheme with FDDA provides better predictions of the ABL depth. For example, at 1600 PDT, the E-ε scheme approximates the observed ABL depth (~900 m) very closely, but even with data assimilation, the ACM-BKT scheme overpredicts the ABL depth by ~300 m. Furthermore, the timing of the collapse of the ABL is better simulated by the E-ε scheme. Predicted virtual potential temperature profiles with the E-ε and ACM-BKT schemes and corresponding observations are shown in Figs. 7d through 7h.

At all observational time periods, both the E-ε and the ACM-BKT predictions are very close to the observations. However, the E-ε scheme shows greater improvement in general than does the ACM-BKT scheme. Thus, consistent adjustment of ground temperature along with the assimilation of ABL and free atmosphere data can lead to improved mixed-layer simulations. Two features stand out from these results: (1) independent of mixed-layer formulation, data assimilation consistently improves the model predictions; and (2) despite data assimilation, minor differences persist between the simulation results, which can be attributed (in this case) primarily to differences between the mixed-layer formulations (since all other formulations are the same).

At this stage it was not clear whether improvements in the simulated ABL structures in the FDDA case were due to assimilation of data into the surface-layer, the mixed-layer, or both. To determine the relative contribution of surface-layer assimilation and associated ground temperature adjustment to the overall improvements in the simulated ABL structures, we performed another case study in which surface-layer assimilation and associated ground temperature adjustment were omitted (in contrast to the previous case, FDDA). Results obtained from this new case are referred to as "NOSFC." Figure 8a shows the vertical variation of virtual potential temperature at 1600 PDT and Fig. 8b shows the temporal evolution of the ABL depth obtained using the ACM-BKT scheme. It is evident omitting surface-layer assimilation and adjustment of ground temperature over predicted the temperature and depth of the ABL (Fig. 8a and 8b) as compared to the FDDA simulation and observations. We also found that sensible heat fluxes at the surface were consistently higher in NOSFC than in FDDA. Results from this case study indicate that surface-layer assimilation and associated ground temperature adjustment indeed help reduce ABL modeling errors.
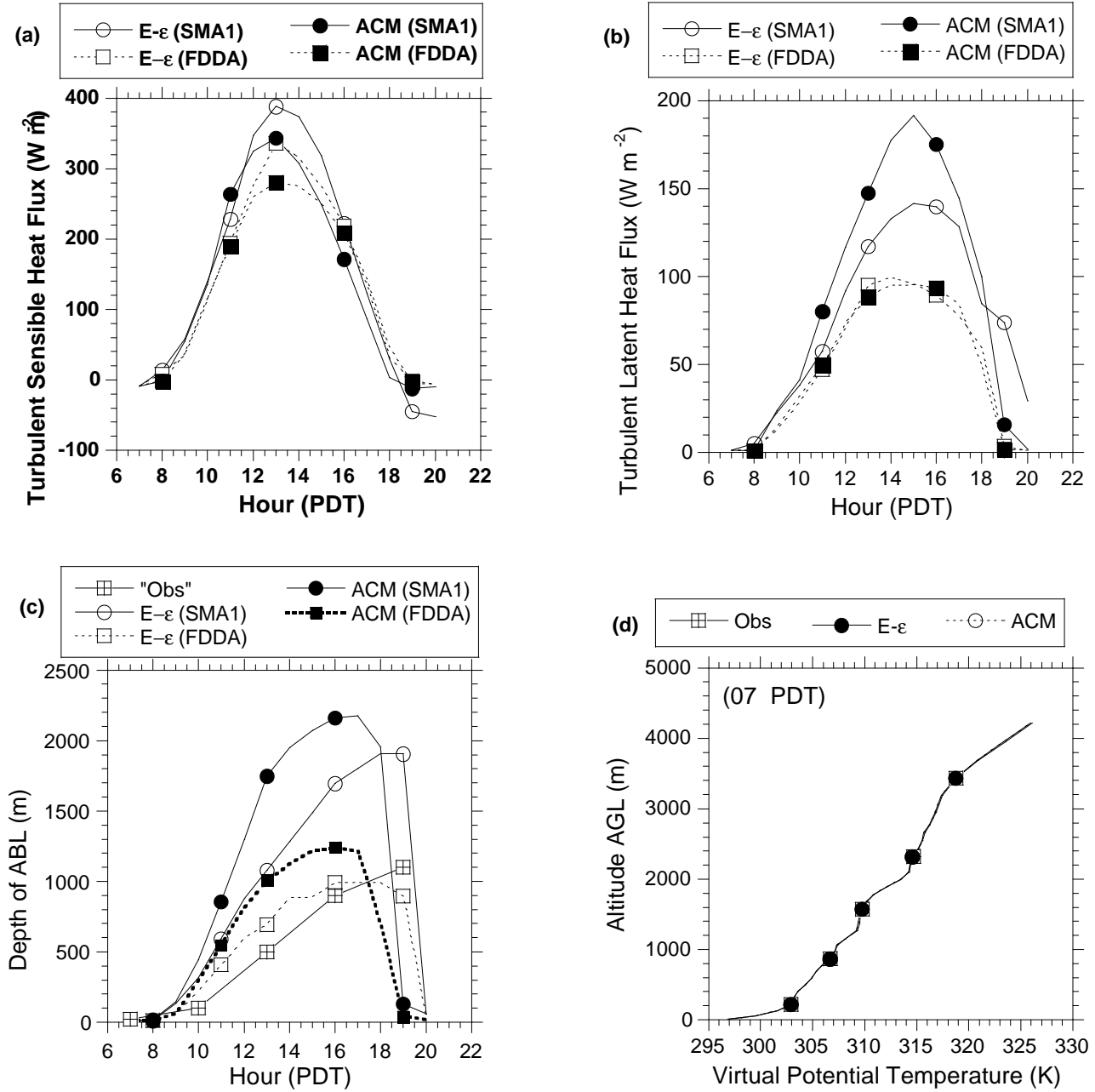
Figure 7. Effects of data assimilation of the boundary layer (including the free atmosphere) for the SARMAP case: Temporal variation of (a) predicted turbulent sensible heat flux, (b) predicted turbulent latent heat flux, (c) predicted depth of the ABL, and (d) predicted and observed virtual potential temperature at 0700 PDT. "ACM" in the legends is short for "ACM-BKT".
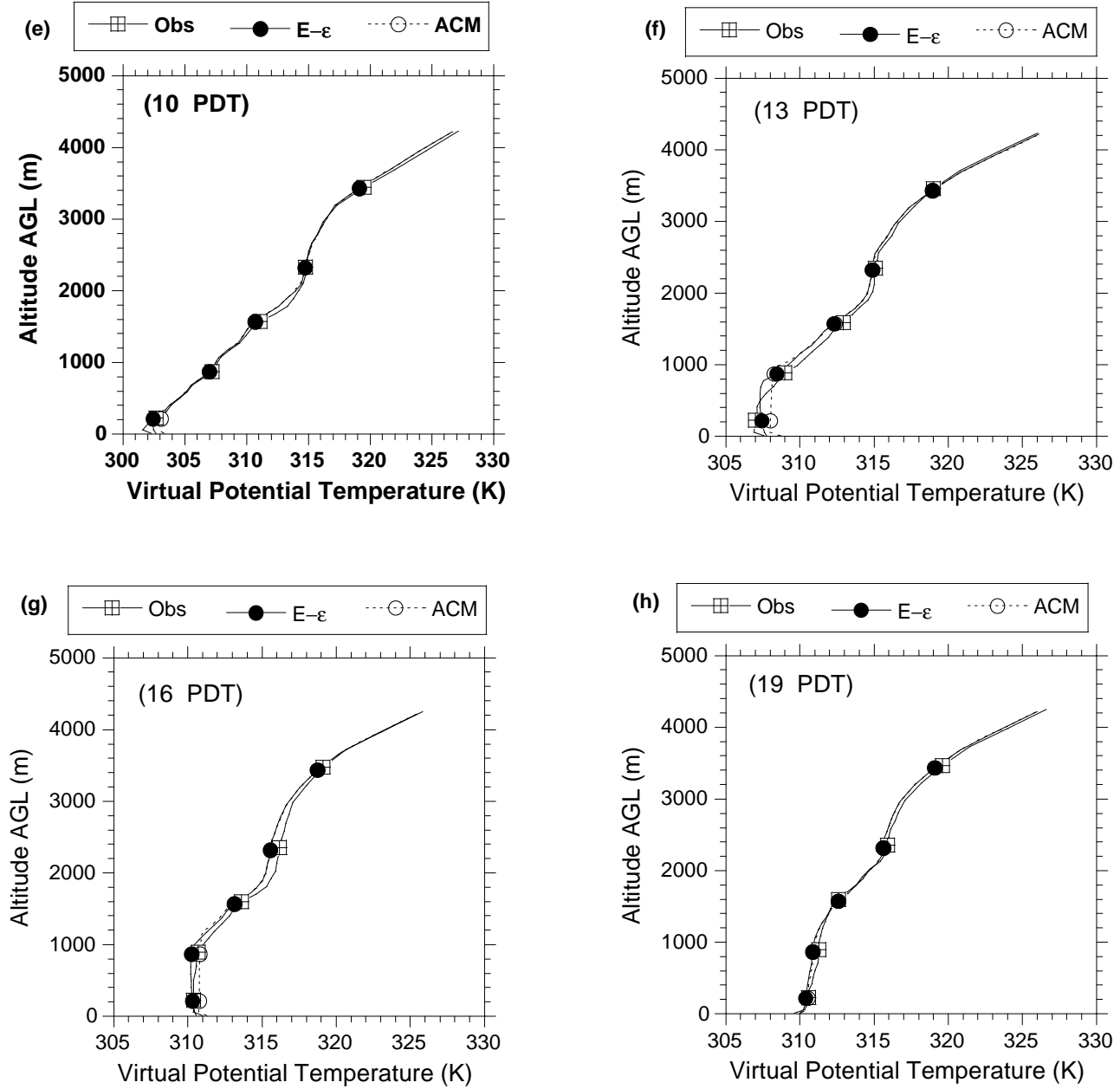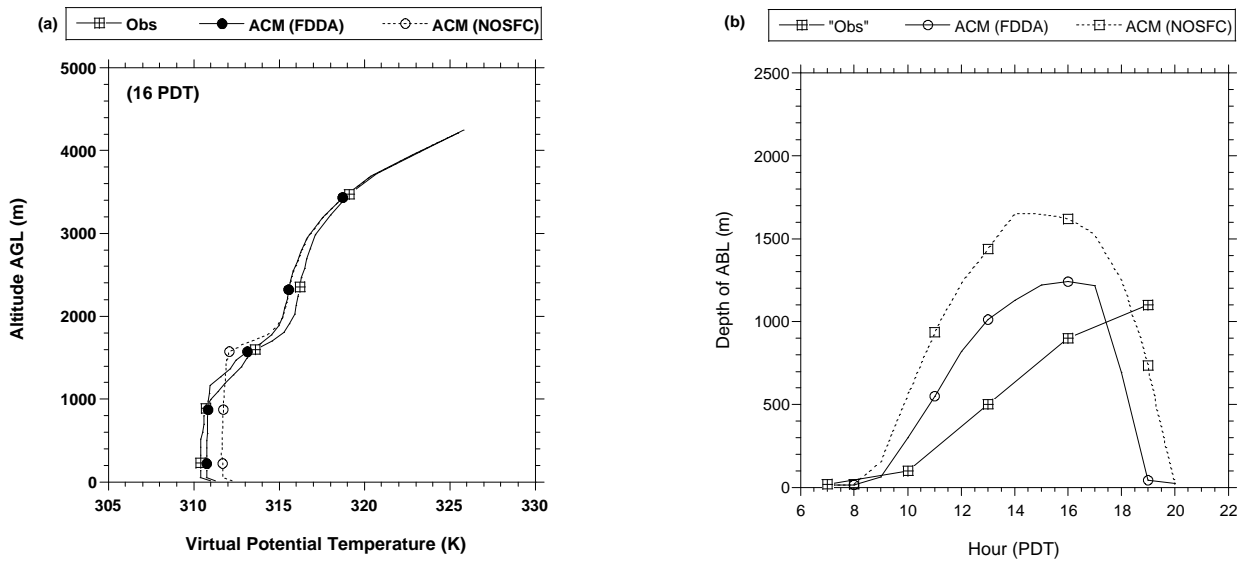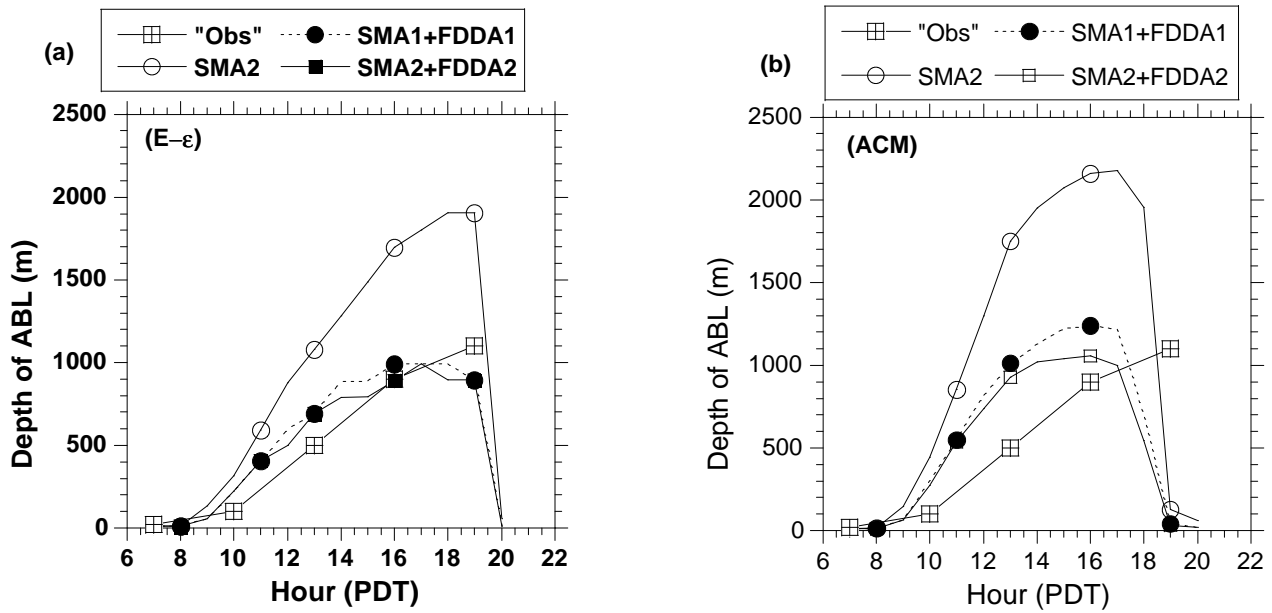
Figure 7 (contd). Effects of data assimilation of the boundary layer (including the free atmosphere) for the SARMAP case (continued): Vertical variation of predicted and observed virtual potential temperature at (e) 1000 PDT, (f) 1300 PDT, (g) 1600 PDT, and (h) 1900 PDT.

Finally, we investigated how the simulated ABL is affected by the combination of data assimilation and increased soil moisture availability. We performed two more simulations with the soil moisture availability values used in SMA2 (recall that SMA2 soil moisture values are double those of SMA1). In the first simulation we used the E-ε scheme and in the second we used the ACM-BKT scheme. Results from the previous FDDA simulations are now referred to as "SMA1+FDDA1," and results from the new simulations are referred to as "SMA2+FDDA2." Figure 9a shows the modeled ABL depths in SMA2, SMA1+FDDA1, and SMA2+FDDA2 using the E-ε scheme, and Figure 9b shows corresponding results obtained using the ACM-BKT scheme. Increased soil moisture availability led to increased latent heat fluxes (not shown), resulting in relatively shallower ABL depths in both of the new simulations. The ACM-BKT–modeled ABL depth at 1600 PDT is now closer to the observed value of about 900 m. Thus, in this case, increased soil moisture availability has a more direct effect on the ACM-BKT simulation than on the E-ε results, which are already close to the observed ABL depths.

Figure 8. Effects of exclusion of surface layer assimilation and associated ground temperature adjustment for the SARMAP case: (a) Vertical variation of predicted and observed virtual potential temperature at 1600 PDT, and (b) Temporal variation of the predicted depth of the ABL using the ACM-BKT scheme.

Figure 9. Combined effects of increased soil moisture availability and data assimilation of the boundary layer (including the free atmosphere) for the SARMAP case: Temporal variation of the predicted depth of the ABL using (a) the E-ε scheme and (b) the ACM-BKT scheme.

In summary, the effects of data assimilation are modulated slightly by the type of boundary layer closure scheme used and by variations in the soil moisture availability used in a simulation. Data assimilation is quite effective for correcting ABL errors due to uncertainties in representing physical processes. These results have important implications for representing land surface processes in meteorological models that maintain constant soil moisture availability over an entire simulation period.

3.2.2 A Technique to Improve the Surface Latent Heat Fluxes

From the above results it is clear that surface soil moisture specification strongly influences boundary layer predictions. To further reduce errors in the surface flux estimation, we present a technique to reduce the uncertainty in specification of soil moisture.

In the MM5 Version 2.7 modeling system, the surface latent heat fluxes are estimated using a simple scheme suggested by Carlson and Boland (1978) as described by Eq. 3 in Section 3.1.2. In this method, soil moisture availability (M_a) is held constant for each land use category irrespective of flood or drought conditions in MM5. It has two values, one for the warm versus cold season. Thus, there is no direct dependency on the transient nature of the canopy respiration or on the diurnal variations in the moisture content of the soil. To introduce the effects of evapotranspiration into this formulation, we developed a methodology based on a statistical index called the water deficit index. For convenience, we repeat Eq. 3 here:

$$L_{hf} = \frac{M_a k u_* \left(q_{vs}(T_g) - q_{va} \right)}{\lambda n \left(\dfrac{k u_* z_a}{K_a} + \dfrac{z_a}{z_\lambda} \right) - \Phi_h}$$

To introduce the vegetative influences on M_a, the soil moisture availability index, we created a new formulation that allows variability in M_a according to the vegetation conditions. This can be written as

$$M_a^* = M_a \left(e^{(0.5 - WDI)} \right) \tag{20}$$

where M_a^* is the modified soil moisture availability and *WDI* is the water deficit index as defined by Moran et al. (1994). The closure problem in the above formulation is the specification of *WDI* using available surface characteristic data and empirical formulations. *WDI* can be estimated from the formulation:

$$WDI = 1 - \frac{E_a}{E_p} \tag{21}$$

where E_a and E_p are total actual evaporation and total potential evaporation from the soil as well as from transpiring canopies. When E_a becomes equal to E_p, then *WDI* is zero, reflecting a zero deficit for the water supply. When *WDI* is zero, canopies can transpire at their maximum potential. On the other hand, when E_a becomes zero, then WDI is unity, reflecting a large water deficit.

To define or estimate WDI we must specify actual and potential evaporation in terms of the evaporation from vegetation and from soil. The components of these two parameters are given as

$$E_a = E_{av} + E_{as} \quad \text{and} \quad E_p = E_{pv} + E_{ps}$$

where E_{av} is actual evapotranspiration from vegetation, E_{as} is actual evaporation from bare soil, E_{pv} is potential evapotranspiration from vegetation (i.e., the maximum evaporation from the freely transpiring canopies), and E_{ps} is potential evaporation from bare soil. We made use of various formulations that exist in the literature to estimate these unknown variables. Using the Penman-Monteith equations, E_{av} can be written as:

$$E_{av} = d \left[\frac{\Delta . R_{nv} + \dfrac{r C_p [e_s(T_a) - e_a]}{r_{ah}}}{\Delta + \dfrac{g(r_{st} + r_{\lambda b} + r_{av})}{r_{ah}}} \right] \tag{22}$$

where δ is a shielding factor, Δ is the ratio of the change in saturation vapor pressure (e_s) to the change in ambient air temperature (Classius-Claperyron equation), R_{nv} is net radiation reaching the vegetation, e_a is actual vapor pressure, r_{ah} is aerodynamic resistance for heat, γ is the psychrometric constant, r_{st} is stomatal resistance, r_{lb} is leaf boundary resistance, and r_{av} is aerodynamic resistance for water vapor. The shielding factor can be written as:

$$d = 1 - \exp(-x . LAI)$$

where *x* is vegetation cover and *LAI* is leaf area index. The leaf boundary resistance can be estimated as:

$$r_{lb} = A \sqrt{\frac{\lambda_w}{\overline{U}}}$$

where λ_w is average leaf width and A is a constant (units are $\sqrt{s/m}$), and $\overline{U}$ is the mean horizontal wind speed.

Similarly, the actual evaporation from soil can be written as

$$E_{as} = (1-d) \left[\frac{\Delta . (R_{ns} - G) + \dfrac{r C_p [e_s(T_s) - e_a]}{r_{ah}}}{\Delta + \dfrac{g(r_{soil} + r_{av})}{r_{ah}}} \right] \tag{23}$$

where R_{ns} is net radiation reaching bare soil, G is soil heat flux, and r_{soil} is soil surface resistance. Following the formulations suggested by Grace et al. (1981), expressions for various unknown terms are given below:

$$r_{av} = 0.93\, r_{ah} \quad ; \qquad r_{ah} = r_{am} + 6.26(u_*)^{-2/3} \qquad r_{am} = \frac{\lambda n \left(\dfrac{z-d}{z_o} \right)}{k^2 \overline{U}} + 1.6 \left(\frac{\lambda n \left(\dfrac{z-d}{z_o} \right)}{k\, \overline{U}} \right)$$

where d is displacement height, z_o is roughness length, k is the Von Karman constant, and $\overline{U}$ is mean horizontal wind speed. The displacement height can be written as

$$d = (1.1h)\ \lambda n\left[1 + \left(C_d\, LAI\right)^{0.25}\right]$$

where h is mean height of the vegetation and C_d is mean drag coefficient for leaves. Following the Simple Biospheric model formulation (Sellers et al., 1986) , the soil surface resistance (r_{soil}) can be written as:

$r_{soil} = \exp(8.206 - 4.255W_s)$

where W_s is soil moisture, to be determined. The net radiation reaching vegetation and the soil surface can be written as:

$R_{nv} = R_{net}\ [1 - \exp(-0.7LAI)]$ and $R_{ns} = R_{net} - R_{nv}$

where R_{net} is the net radiation.

The equation for the potential evaporation from the vegetation can be written as

$$E_{pv} = d\left[\frac{\Delta.R_{nv} + \dfrac{rC_p\left[e_s(T_a) - e_a\right]}{r_{ah}}}{\Delta + g}\right] \tag{24}$$

and from bare soil it is

$$E_{ps} = (1 - d)\left[\frac{\Delta.(R_{ns} - G) + \dfrac{rC_p\left[e_s(T_s) - e_a\right]}{r_{ah}}}{\Delta + g}\right] \tag{25}$$

We made use of the formulation suggested by Taconet et al. (1986) to estimate the stomatal resistance:

$$r_{st} = r_{s\min}\left[\frac{Q_{\max}}{C_1 Q_{\max} + Q} + \left(\frac{1.2W_{wilt}}{W_s}\right)^2\right]\left(\frac{1 + 0.5LAI}{LAI}\right) \tag{26}$$

where W_{wilt} is soil moisture during wilting conditions, $Q_{\max}$ is maximum radiation reaching the ground, Q is radiation reaching the ground at a given instant, and $r_{s\min}$ is minimum stomatal resistance. Now the problem narrows down to the estimation of soil moisture, W_s. There are two ways to solve this problem. The first is the prognostic equation for solving soil moisture. This procedure is very common in many current land surface models. However, there are two problems with this approach. First, it is usually very expensive because very small time steps are required to solve the soil moisture prognostic equation. Second, uncertainty is present in the input data and in other data estimated using empirical formulations. To avoid these problems, we chose to use the second method for estimating soil moisture: an empirical relation. This approach is common in the

literature. Thus, we considered a formulation similar to that suggested by Mahfouf (1991) to estimate the soil moisture. This can be written as:

$$W_s = 114.95 - 0.31T_a - 0.06RH \qquad (27)$$

where T_a is air temperature and RH is relative humidity of the air in the surface layer. The constants in the above equation are obtained from a regression curve fit using data from the Environment and Climatic Observations NETwork (ECONET) observations database; these data are being collected continuously by the State Climate Office of North Carolina. The above equation is the main closure to the problem considered in our approach. Now that all unknown variables are specified or estimated, *WDI* can be written as

$$WDI = 1 - \frac{E_a}{E_p} = \frac{\text{O (Uncertainty)}}{\text{O (Uncertainty)}}$$

Note that several empirical formulations, constants, and parameters are used in the above series of equations. Thus, there is a lot of uncertainty in various parametric estimations of E_a and E_p. Because similar kinds of uncertainty exist in both the formulations and all of the related equations for E_a and E_p, we believe that the uncertainty in the specification of surface characteristics is minimized in this type of parameterization. Once *WDI* is estimated, the modified soil moisture availability can be calculated as

$$M_a^* = M_a . \exp[0.5 - WDI]$$

Since *WDI* ranges from 0 to 1, the value of the second part of the right hand side of the above equation ranges from about 0.6 to 1.6. This kind of equation assumes that the uncertainty in the M_a estimation is well between 40% of the higher end (overprediction) and 60% of the lower end (underprediction). For example, consider a grid cell covered with forest. Then, for this grid cell the Ma is 0.3 for summer and 0.7 for winter. With the new formulation the M_a^* can be between 0.18 and 0.48 for summer while for winter it can be between 0.42 and 1.12. Since, $M_a^* = 1.0$ means that the air at the surface is at its saturation level, any value above 1.0 does not have any physical meaning. Thus, the values of M_a^* are restricted to range from 0.0 to 1.0. Thus, using this new formulation, the Eq. 3 is rewritten as:

$$L_{hf} = \frac{M_a^* k u_* \left(q_{vs}(T_g) - q_{va} \right)}{\lambda n \left(\frac{k u_* z_a}{K_a} + \frac{z_a}{z_\lambda} \right) - \Phi_h}$$

To investigate whether the above new parameterization scheme for soil moisture improves the surface latent heat fluxes, we performed three 1-D simulations using the formulations and data from the earlier simulations. We used the FIFE data to provide initial conditions and to verify the modeled results. In each of the three simulations, we used a different method of estimating the surface latent heat fluxes: (1) the standard MM5 method as described by Eq. 3, (2) the new method just described in this section, and (3) the Noilhan and Planton (1989) method. Preliminary results are described below.

Figure 10 contrasts the surface latent heat fluxes observed with those predicted using the three different methods. Observations are denoted by "OBS," modeled values obtained from using the standard MM5

method by "OLD," those obtained from using the new method by "NEW," and those from the Noilhan and Planton (1989) method by "NPJ." As expected, predicted latent heat fluxes from OLD are lower than in the observations, while those from NPJ are higher. There is reasonable agreement between the observations and NEW. Also note that latent heat fluxes from NEW are higher than those from OLD, indicating that modulation of soil moisture availability seems to improve model predictions. Figure 11 shows observed and predicted surface sensible heat fluxes. It seems that all of the methods (OLD, NEW, and NPJ) overestimated sensible heat fluxes. The pattern is the reverse of that for latent heat fluxes: OLD results in the highest values while NPJ results in lower values than with the other methods. Sensible heat fluxes obtained from NEW are very close to the NPJ results. We think that the soil properties (e.g., heat capacity) prescribed in the 1-D model may not be suitable for the FIFE site. This issue needs further attention.

Observed and predicted virtual potential temperatures (Θ_v) at 1400 CDT are shown in Figure 12. Because the sensible heat fluxes are overpredicted in all simulations, predicted Θ_v is higher than in the observations. Consistently, results from NEW and NPJ are much closer to the observations than the OLD results. Observed and modeled water vapor mixing ratios at 1400 CDT are shown in Figure 13. The NEW predicted mixing ratios are very close to the observations.

In NPJ, the soil moisture is explicitly predicted for the two soil layers. NEW, on the other hand, does not do explicit estimation. However, it does have an empirical equation for the soil moisture based on a regression curve fit using the ECONET data. It is interesting to compare the soil moistures predicted by these two methods. Figure 14 shows the temporal variation of modeled soil moisture from NPJ and from NEW. In NPJ, soil layer 1 responds to diurnal changes; soil layer 2 acts as a reservoir, so its diurnal changes are expected to be small. The soil moisture estimated from NEW (denoted by NEW_SM) acts like that for soil layer 2 in NPJ, and the magnitudes of these two are comparable. The original formulation (OLD) does not contain vegetative effects. NEW, however, does contain these effects, so the temporal variation of soil moisture in NEW can be considered to be similar to the variation in NPJ's root zone moisture (i.e., soil layer 2 moisture).

38

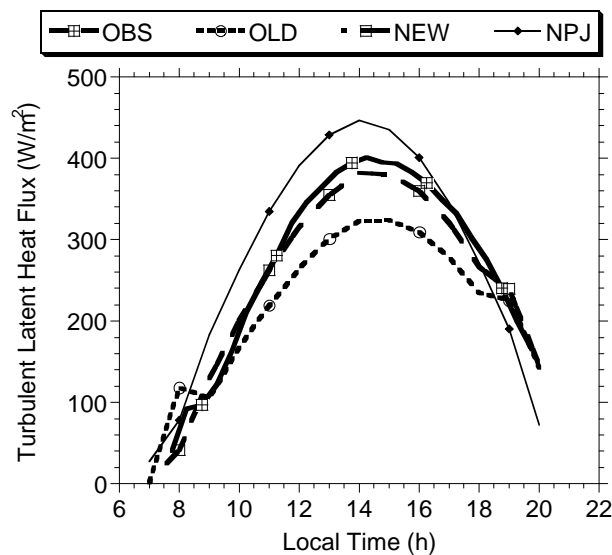Figure 10. Comparison of observed surface latent heat flux with simulations using three soil moisture formulations.. OBS: observations; OLD: standard MM5 method; NEW: WDI method; NPJ: Noilhan-Planton method.
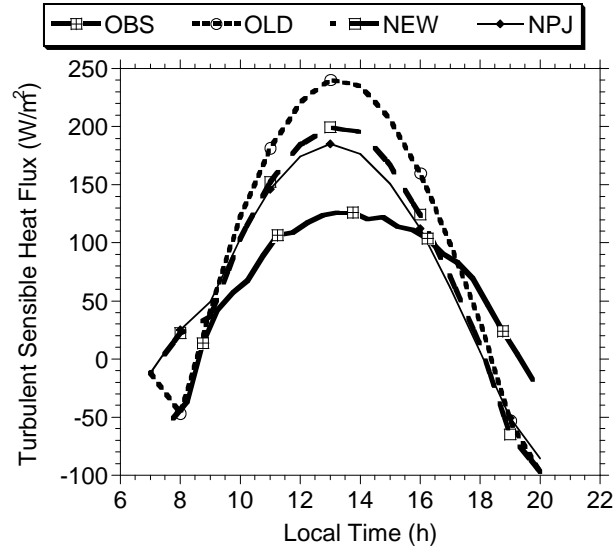
Figure 11. Comparison of observed sensible heat flux with simulations using three soil moisture formulations.. OBS: observations; OLD: standard MM5 method; NEW: WDI method; NPJ: Noilhan-Plantion method.

Figure 12. Vertical variation of virtual potential temperature at 1400 CDT. OBS: observations; OLD: standard MM5 method; NEW: WDI method; NPJ: Noilhan-Plantion method.

Figure 13. Vertical variation of water vapor mixing ratio at 1400 CDT. OBS: observations; OLD: standard MM5 method; NEW: WDI method; NPJ: Noilhan-Plantion method.
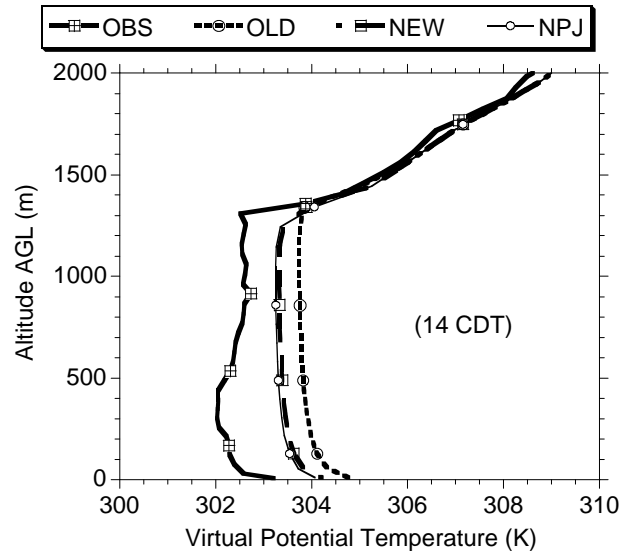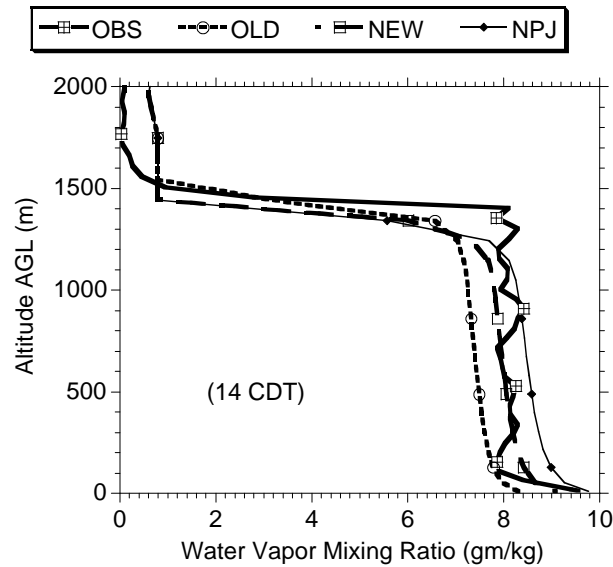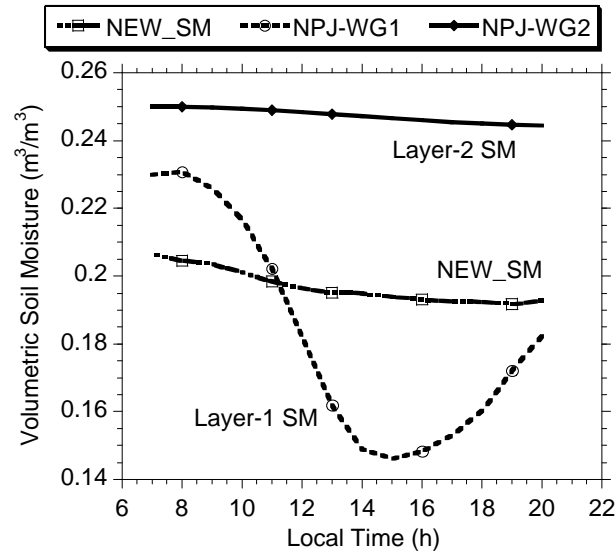
Figure 14. Temporal variation of soil moisture. NEW_SM: WDI method; NPJ: Noilhan-Plantion method.
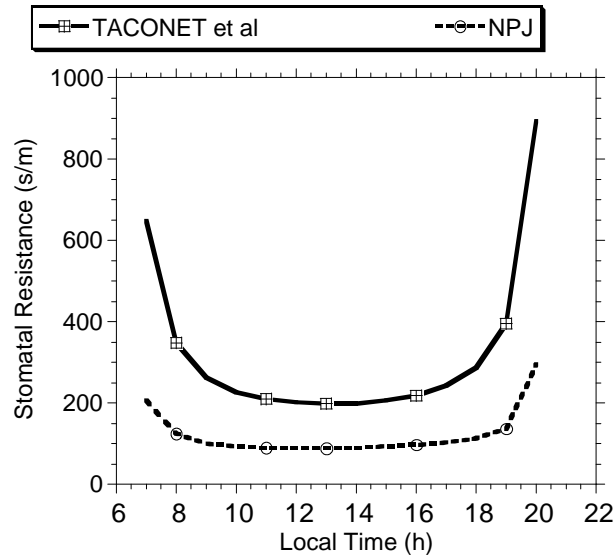

Figure 15. Temporal variation of stomatal resistance. NPJ: Noilhan-Plantion method.

These preliminary results are very encouraging and showed some improvement in the model predictions. To illustrate the effects of uncertainty, we show in Figure 15 the estimated stomatal resistance (R_s) from two different methods. This figure shows the temporal variation in R_s estimated by Teconet et al. (1986) and also from NPJ. Both formulations are based on observational evidence for different geographic regions. The figure shows that the type of formulation chosen in a scheme can result in different outcomes, thus contributing to uncertainty in the model estimates.

The method we have developed is designed to suppress the effects of uncertainty in the model estimation of various surface characteristics and processes. We are investigating how various formulations affect the estimation of WDI and hence the surface latent heat fluxes. We are currently conducting more simulations and sensitivity tests and will present the results at a later date.

3.3 Three-Dimensional Model Simulations

We now move to the three-dimensional model simulations we used to study the effects of various physical and dynamical processes that control the depths of the mixed layers over central California.

Results from prior 3-D numerical investigations have indicated that many mesoscale meteorological models have difficulty simulating the very shallow mixing depths often found in the SJV. For example, as noted in Section 1, Seaman et al. (1995) found that MM5 overpredicted afternoon mixing depths during two of the SJVAQS/AUSPEX cases by over 300 m (Figure 16). Although this result is not unique to MM5, the performance of this model is of particular interest because it has been adopted by CARB as the primary meteorological model for use in numerical air quality studies in California. Here we use MM5 (1) to study the 3-D physical and dynamical causes of the shallow mixing depths in the SJV, and (2) to determine what modeling options might correct errors in prior MM5 simulations of the SJV mixed-layer depths.

In this section we first present a statement of work based on hypotheses concerning the shallow SJV mixing depths and the causes of previous 3-D modeling errors. Next, we give a brief overview of the 3-D MM5 version used in the study, followed by a discussion of the experimental methodology we used to test these hypotheses. Finally, we describe the cases used in this study and the results obtained from the various simulations.

3.3.1 Hypotheses and Work Plan

We began the project by following the original Statement of Work (as documented in CARB Contract 96-319 with NCSC), which required us to examine the effects of large-scale dynamics and of model vertical resolution. As the work progressed, however, evaluation of the first few experiments suggested that additional processes might be important for explaining the occurrences of low mixing depths over the SJV. We therefore expanded the Work Plan (at no additional cost) in order to include several new experiments designed to investigate the following issues: (1) the role of the initial structure of the marine atmospheric boundary layer (MABL), (2) the role of mesoscale circulations in the Sacramento Valley, (3) the influence of the type of
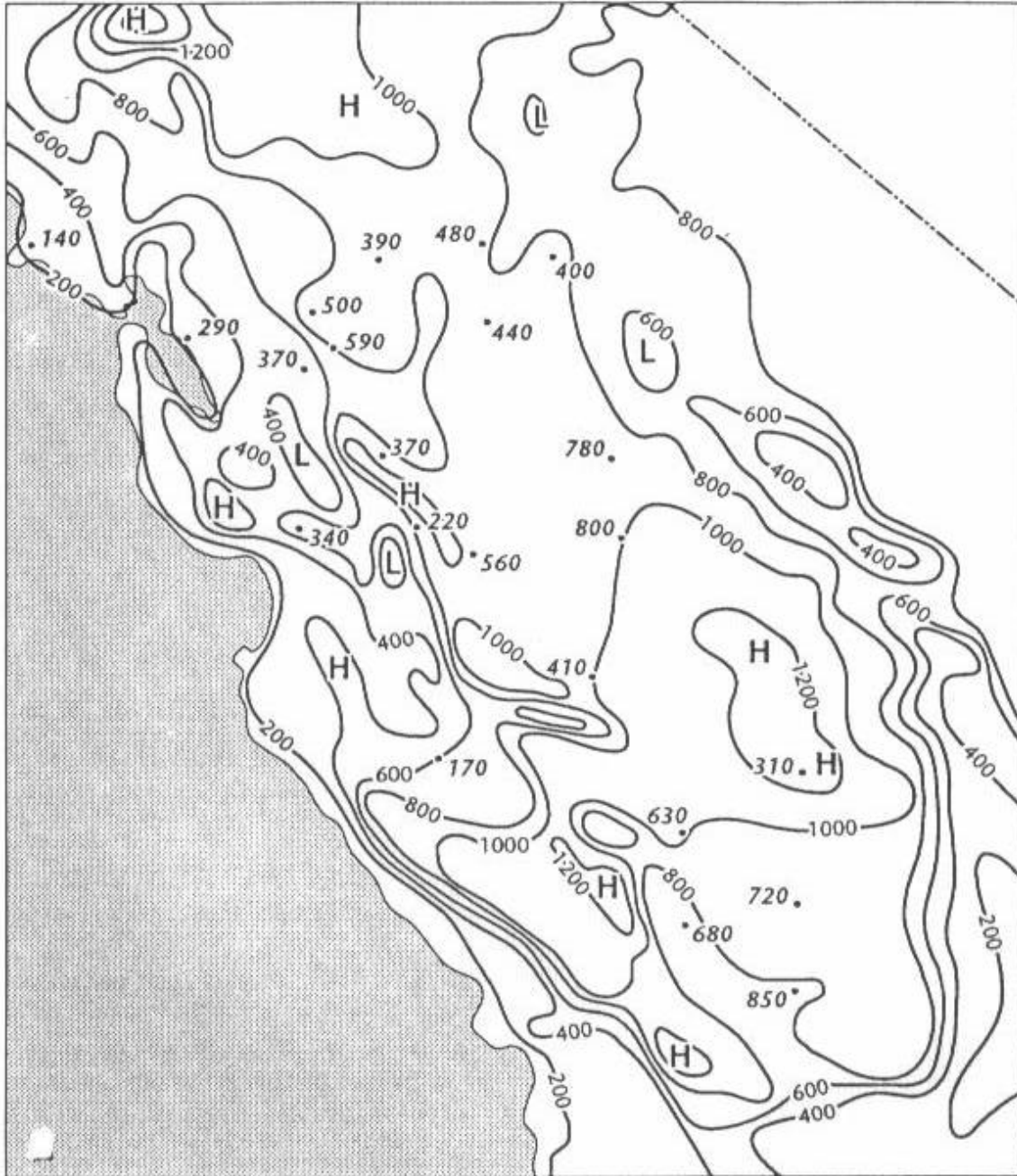
Figure 16. Mixed-layer depth (m) simulated by the MM5 at 0000 UTC 6 August 19990 in the 4-km domain described by Seaman et al. (1995), Experiment 7 in this report. Contour interval is 200 m. Observations from upper-air network (Fig. 17) are shown in italics.

boundary-layer turbulence parameterization used in the numerical model, and (4) the influence of four-dimensional data assimilation (FDDA) in the 36-km and 12-km domains. The goals of this 3-D modeling study were to identify the most important physical processes that contribute to shallow SJV mixing depths and to learn what numerical configurations and methods are necessary to successfully simulate those processes for this region. The expanded list of hypotheses and experiments appear in Sections 3.3.1.1 through 3.3.1.6.

3.3.1.1 Experiment 1: Effects of Large-Scale Dynamics and Thermodynamics

We hypothesized that strengthening of the large-scale subsidence associated with the Northeast Pacific Ridge may be an important factor contributing to the shallow mixing depths observed in the SJV during episodes of poor air quality. The Pacific Ridge is a quasi-stationary climatological feature that is very persistent during the summer months and is responsible for the well-known very strong inversion layer that caps the MABL off the coast of California (Ahrens 1993). When the ridge shifts toward the east, 500-mb heights rise over the interior of California. It is likely that this height rise is accompanied by increased synoptic-scale subsidence. The enhanced subsidence over California is hypothesized to contribute to broad adiabatic warming of the middle levels of the troposphere, thereby acting to prevent growth of the convectively unstable mixed layer and resulting in much-reduced ventilation of pollutants. This proposed mechanism may be an active contributor to the shallow mixing depths in the area of interest, but the absence of such an extreme response over larger areas of the western United States strongly suggests that it cannot be the only process at work.

In order for a numerical model to correctly simulate the changes in the ridge position and intensity, and thus the changes in the synoptic-scale subsidence, the outer model domain may need to include most or all of the region covered by the ridge. In earlier experiments reported by Seaman et al. (1995), the largest domain covered an area of only 1944 x 1944 km, using a 36-km mesh. In Experiment 1, we test the hypothesis that the dynamics of the ridge may be important in simulating the subsidence over the SJV by adding an outer domain having a 108-km mesh and covering an area of 4860 x 6480 km.

3.3.1.2 Experiment 2: Effects of Vertical Resolution

In the original MM5 experiments performed by Seaman et al. (1995), the model was configured with 30 layers in the vertical direction. While this is completely adequate for many purposes, it is hypothesized that the resolution used in the vicinity of the mixed-layer top was too coarse to adequately resolve weak capping inversions in that study (layer thicknesses in the lowest kilometer had averaged ~120-150 m). Therefore, Experiment 2 explores the impact of resolution by increasing the number of layers to 62, which allows the layer thickness to be only 40 m throughout the first kilometer above ground.

Better resolution not only allows more accurate treatment of the inversion layer in the SJV, it may also improve the model's representation of the transverse-vertical valley breeze circulation. The mesoscale valley breeze flowing up the sides of the mountain ranges flanking the SJV should induce a compensating subsidence circulation over the valley. This mesoscale subsidence has the potential of reinforcing the synoptic-scale subsidence, thus creating a regional maximum of downward motion and adiabatic heating over the SJV. It is hypothesized that superposition of the synoptic and mesoscale subsidences could explain the low mixing depths found in this region.

3.3.1.3 *Experiment 3: Effects Due to Initialization of the Marine Atmospheric Boundary Layer*

In the summertime, air originating over the ocean in the MABL is advected inland through the San Francisco Bay area and other gaps in the Coast Range mountains. It then is modified by surface heating as it travels southward into the SJV. As for most limited-area models, initialization of the MM5 variable fields in real cases requires the use of background global meteorological fields. In these 1990 cases, we used fields analyzed by the National Center for Environmental Predictions (NCEP). Over the ocean, where data are very sparse, these analyses rely mostly on short-range predictions generated by the most recent run of the NCEP global spectral model. Because the global model has relatively coarse vertical resolution and rather simple boundary layer physics, it often does not accurately represent the thermal and moisture structure of the MABL. Therefore, we hypothesized that errors in the initial offshore MABL structure used in MM5 experiments could adversely affect simulations of the inland modification of that marine air mass, and hence lead to errors in the predicted SJV mixing depths.

To test this hypothesis, we corrected the thermal and moisture structure of the MM5's MABL at the initial time, rather than allowing the MM5 to generate the MABL structure completely on its own. This was thought to be important because the physical processes that generate the shallow MABL act rather slowly, requiring ~24-48 h to create a fully developed cold MABL. The logistics for this initialization are relatively straightforward because Penn State already had developed a marine boundary layer initialization (MBLI) technique, based on climatology and case-specific observations, for use over the Eastern Pacific Ocean (Leidner et al. 2000).

3.3.1.4 *Experiment 4: Effects of Mesoscale Circulations in the Sacramento Valley*

One of the more important mesoscale circulations affecting airflow into the SJV is found in the Sacramento River delta area, where the strong marine inflow through the San Francisco Bay diverges into two separate branches. One branch heads southeastward into the SJV, while the other branch turns north-northwestward up the Sacramento Valley. These two flows are forced by two thermally induced low-pressure centers in the vicinities of Bakersfield and Redding, CA. We hypothesized that the accuracy of the model-simulated mass fluxes into these two valleys is dependent on the accuracy with which this split flow is represented by the model.

During the numerical experiments conducted by Seaman et al. (1995), the northern boundary of the 4-km domain was located just north of the city of Sacramento near 39.0 N (Figure 17). However, while this location for the 4-km boundary placed the Sacramento Delta within the 4-km domain, the location of the thermal low near Redding was farther north in the 12-km domain. That means that an artificial (numerical) interface was interposed between the region of the flow divergence and one of the low-pressure centers driving this mesoscale circulation. Consequently, there was considerable opportunity for the introduction of model-induced errors in the meteorological simulations.
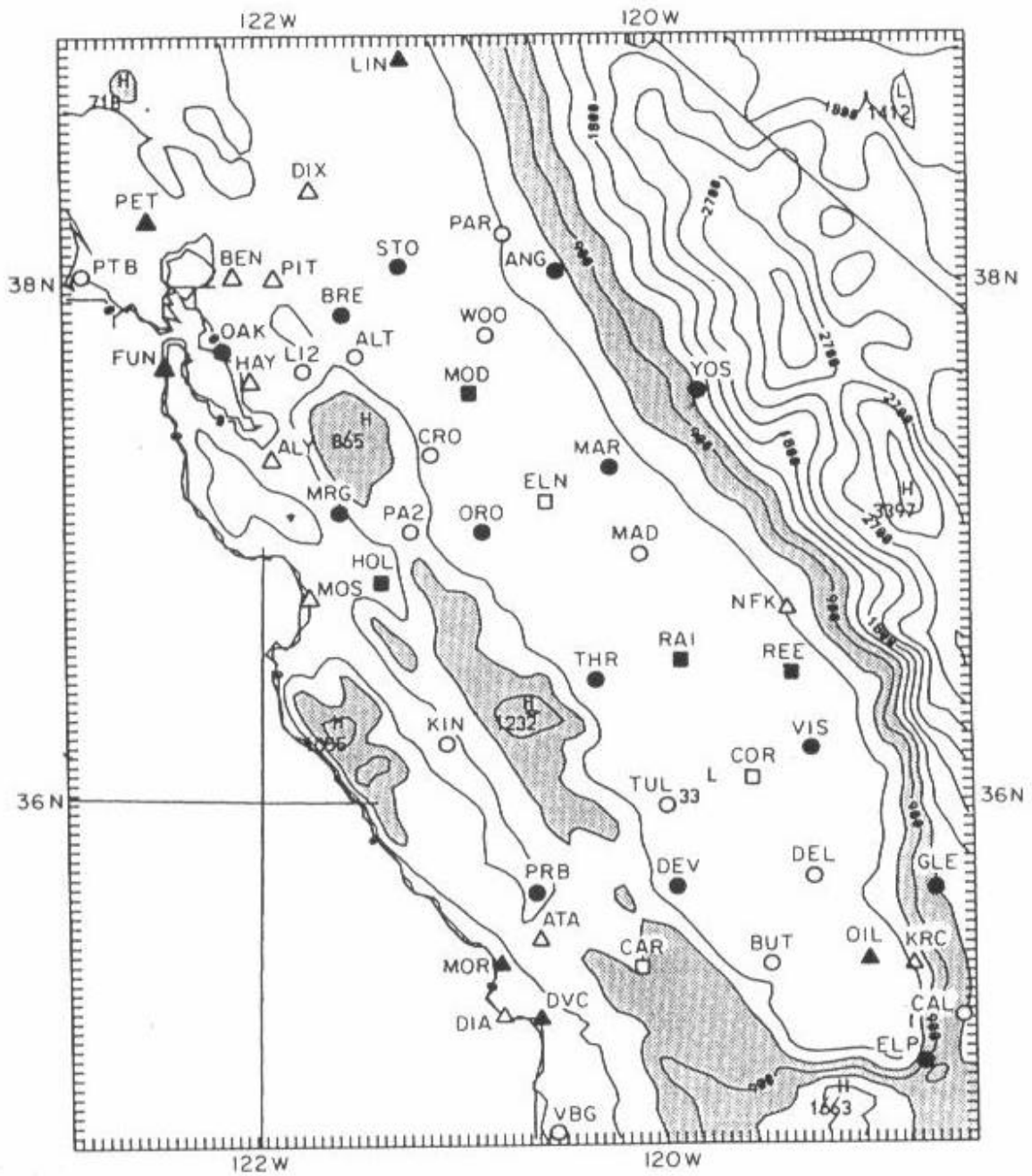
Figure 17. Location of special upper-air measurement sites for SJVAQS/AUSPEX. Circles represent radiosondes, triangle represent Doppler acoustic sounders, and boxes represent profilers. Data from these sites are used for model verification only and are not assimilated in any of the experiments.

As a corollary to the hypothesis expressed above for this experiment, we believed that a consistent treatment of the split flow requires that both thermal lows be included within the 4-km domain. This is done easily by extending the domain northward above Redding to about 40.2 N, as shown in Figure 18.

3.3.1.5 Experiment 5: Effects of Boundary-Layer Turbulence Parameterization

In the original experiments of Seaman et al. (1995), the Blackadar nonlocal turbulence scheme was used to represent boundary layer processes (Zhang and Anthes 1982). However, as seen in the 1-D model simulations and tests by Shafran et al. (2000), the Blackadar-type schemes have a bias toward overpredicting the depth of convectively unstable boundary layers, even when capped by a moderate inversion (2-6 °C). Therefore, we anticipate that after replacing the Blackadar scheme by a 1.5-order parameterization that explicitly predicts turbulent kinetic energy (TKE) and produces very low bias for boundary-layer depths (Shafran et al. 2000) MM5 would be better able to simulate the shallow mixing depths found in the SJV.

3.3.1.6 Experiment 6: Effects Due to Four-Dimensional Data Assimilation Strategy

It is well known that data assimilation strategies can have important influences on both numerical model solutions and analyses. In the case of the FDDA strategy used by Seaman et al. (1995), the solutions on the 36-km and 12-km domains were nudged toward synoptic-scale analyses from the top of the domain at 100 mb downward to the top of the boundary layer. However, that strategy may have had unexpected consequences. In particular, during the nocturnal period when only a shallow stable boundary layer exists, this FDDA strategy caused the layers in and above the vicinity of the daytime mixed-layer top (the interfacial layer) to be forced toward those synoptic-scale analyses. In the case of layers above the surface, the analyses are based on the National Weather Service standard synoptic observations spaced at roughly 400 km. However, these data do not provide sufficient horizontal or vertical resolution to accurately represent the stable layer capping mixed-layer growth and none exist over the SJV. (The special SJVAQS/AUSPEX data are not used to create analyses for model initialization or for analysis nudging.

We hypothesized that this FDDA strategy may have resulted in an unintended smoothing of any mesoscale mid-level stable layer that develops in MM5, thus weakening resistance to boundary-layer growth during the daytime. The direct effect of this smoothing occurs on the 36-km and 12-km domains where the analysis nudging is performed. However, the 12-km solutions are used to provide lateral boundary conditions to the 4-km domain (which is the primary domain used to study SJV phenomena). Therefore, it is possible that the loss of accuracy in the 12-km domain due to the nudging strategy of Seaman et al. (1995) could have indirectly degraded the accuracy of the 4-km solutions as the influence of the boundary conditions was advected through the domain during the model integrations.

Based on earlier FDDA work by Shafran et al. (2000), Experiment 6 is designed to test this hypothesis by removing all analysis nudging below 1.5 km AGL (unless, of course, the boundary layer is deeper than 1.5 km). This approach should prevent unintended weakening of any mid-level stable layer generated by mesoscale circulations or by other processes. No nudging toward
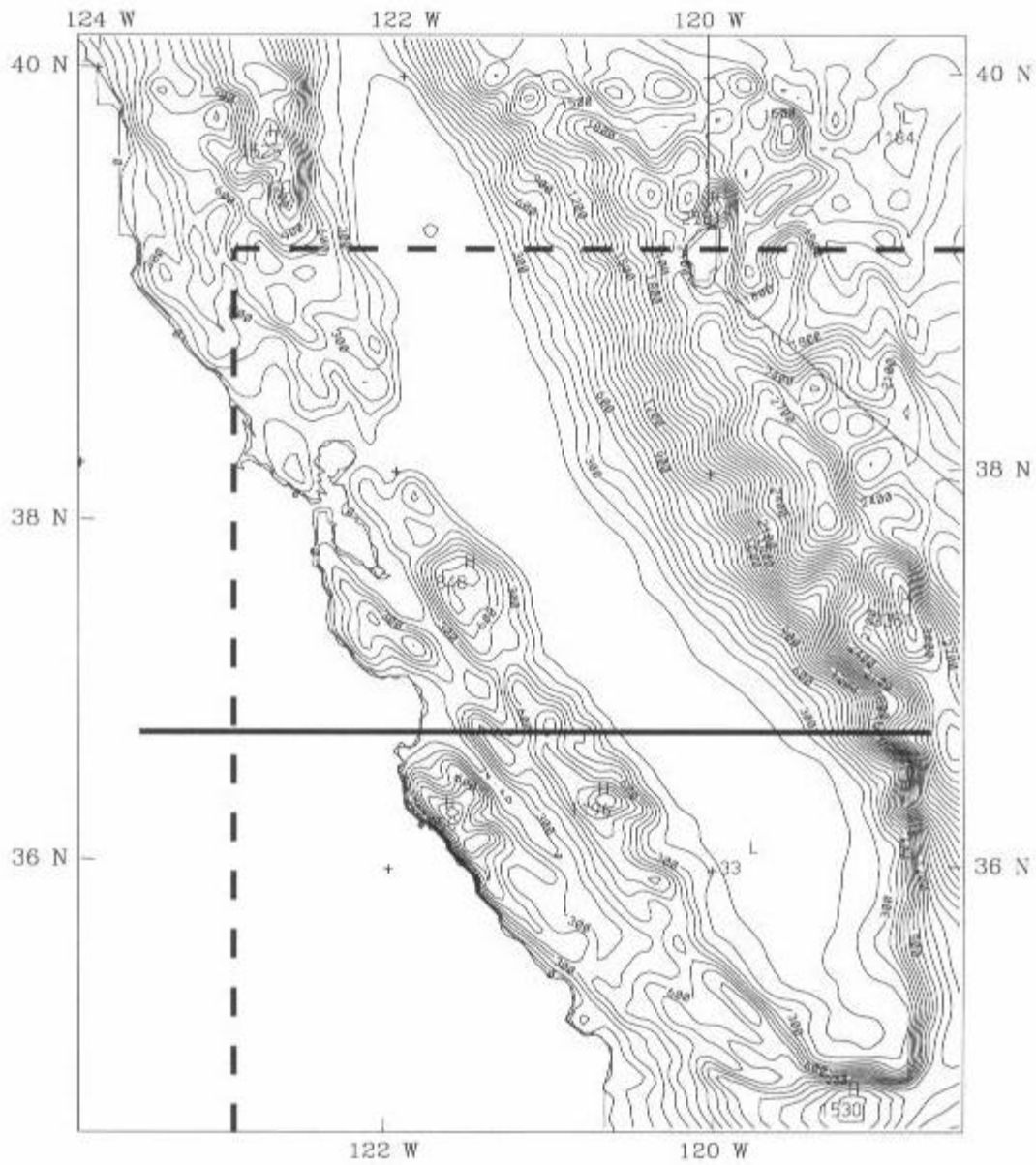
Figure 18. Terrain (m) for the large innermost 4-km mesh used in Exps. 1-4. Contour interval is 100 m. Heavy horizontal line shows location of a cross section through Fresno. Dashed line makrs location of the smaller 4-km domain used in Epxs. 5-7 (see Table 1).

any of the special SJVAQS/AUSPEX observations is performed in this study. Furthermore, no analysis nudging is used on the 4-km domain, so that FDDA is felt on the innermost domain only through the lateral boundaries supplied from the 12-km grid. This approach is used so that the model's physical and dynamical processes are free to develop mesoscale circulations on the 4-km inner mesh without imposing the influence of any artificial forcing terms.

3.3.2 Model Description

The numerical model used in this study is the 3-D nonhydrostatic MM5 (Dudhia 1993, Grell et al. 1994). The MM5 is a nested-grid primitive-equation model written in the terrain-following nondimensionalized pressure vertical coordinate (sigma). For efficiency, MM5 uses a split semi-implicit temporal integration scheme. Prognostic equations predict the 3-D wind components (u, v, and w), temperature (T), water vapor mixing ratio (q_v), and the perturbation pressure (p'). The perturbation pressure is the departure from a temporally invariant reference-state pressure described by Dudhia (1993).

A surface energy budget equation predicts the ground temperature (T_g) and includes the effects of insolation, atmospheric path length, water vapor, cloud cover, and longwave radiation (Zhang and Anthes 1982). Surface physical characteristics of albedo, roughness length, moisture availability, emissivity, and thermal inertia are defined as a function of land use for 14 categories via a look-up table. The land use definitions over California were made using a 1-km database supplied by the Desert Research Institute. Radiation flux divergence at each layer is calculated using a full column broadband two-stream scheme (Dudhia 1989). Additional model physics include explicit prognostic equations for mixing ratios of cloud water/ice (q_c) and rain/snow (q_r), but without mixed-phase microphysics (Dudhia 1989). Subgrid deep convection is parameterized using the scheme of Kain and Fritsch (1990).

Turbulent processes are represented in this study using either of two parameterizations. The first is a 1.5-order TKE-predicting scheme described by Shafran et al. (2000). The second is a Blackadar nonlocal-closure scheme (Zhang and Anthes 1982), which had been used in the experiments reported by Seaman et al. (1995). As mentioned earlier, Shafran et al. (2000) demonstrated that the 1.5-order TKE scheme produces lower biases for simulations of mixed-layer depth, so it is used in most of the experiments reported here.

3.3.3 Methodology

We conducted a series of seven experiments to learn how SJV mixing depths are influenced by the following factors: synoptic-scale dynamics, vertical resolution, MABL initial conditions, mesoscale circulations, boundary-layer physics, and FDDA. All experiments were performed for the four-day high-pollution episode that occurred from 2-6 August 1990 that was observed during the SJVAQS/AUSPEX. The initial and boundary conditions on the outermost model domain were specified from the NCEP global spectral-model analyses. Initial conditions for inner nested domains were obtained by interpolation, while the MM5 solutions from the next coarser grid were used to provide the conditions at the lateral grid-interfaces. Table 1 summarizes the experimental conditions.

Table 1. Experimental conditions for the MM5.

Exper No.	MBLI	No. of Domains	Expanded 4-km Domain	FDDA below 1.5 km	PBL Type	No. of Layers

1	Yes	4	Yes	No	TKE	62
2	Yes	4	Yes	No	TKE	32
3	No	4	Yes	No	TKE	32
4	No	3	Yes	No	TKE	32
5	No	3	No	No	TKE	32
6	No	3	No	Yes	TKE	32
7	No	3	No	Yes	BLKDR	32

All experiments used three model domains having mesh sizes of 36 km, 12 km, and 4 km, and Experiments 1-3 used a fourth 108-km domain of 46 x 61 points (Figure 19). The 36-km domain had 55 x 55 points and the 12-km domain had 79 x 55 points. Two different sizes of 4-km domain were used in the study. The larger grid had 151 x 121 points and was used for Experiments 1-4; the terrain for these four experiments is shown in Figure 18. A smaller 4-km grid of 118 x 100 points was used in Experiments 5-7, the area of which is indicated by the dashed lines in Figure 18. This smaller 4-km domain included the entire SJV, but omitted the upper Sacramento Valley to the north and had its western boundary closer to the coastline.

3.3.4 Case Description

The early August period of 1990 was fairly characteristic of the summertime climatology for California and of conditions associated with high levels of ozone. At the beginning of the episode (1200 UTC 2 August), a 500-mb ridge lay off the California coast with a maximum height of 591 dam centered several hundred kilometers southwest of Oakland (Seaman et al. 1995). During the episode the height maximum gradually intensified to 599 dam and shifted slowly northeastward over the western United States, until it reached southwestern Idaho on 7 August 1990. The intensification of the ridge and its movement over land during the period of most severe air pollution (5-6 August) are consistent with increased synoptic-scale subsidence and warming (temperatures rose about +3 °C at 500 dam over California-Nevada during the episode). However, since the subsidence rate in large anticyclones is only on the order of 1-5 cm s^{-1}, there are no observations for vertical velocity. Therefore, a numerical model provides the best means of estimating the evolution of subsidence as the episode proceeds.

As is typical for summertime, cool marine boundary-layer air is advected onshore due to the pressure gradients induced by intense heating over the interior of California.   This marine air is rapidly modified due to the daytime surface sensible heat flux and eddy transport in the convectively unstable boundary layer. Normally, as marine boundary-layer air is heated, the mixed layer should grow in depth. In this region, the heating occurs rapidly as the column of marine air experiences advection, so it is appropriate to follow the effects of the thermal
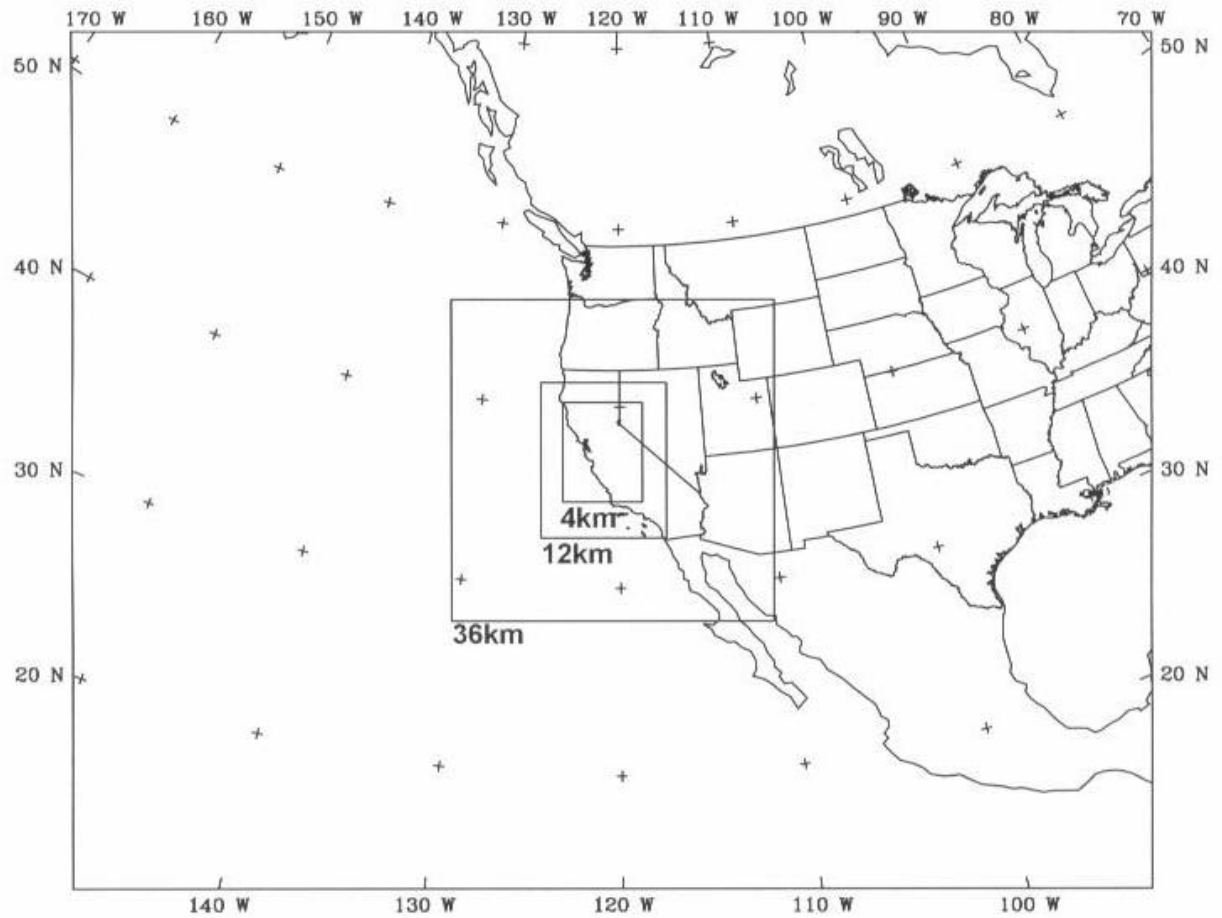
Figure 19. Mesoscale model nested domains showing the 108-km resolution outermost mesh. Boxes show locations of nested 36-km, 12-km, and large 4-km domains.

modification in a Lagrangian reference frame. To demonstrate the effects of this air mass modification, we examined observed thermal soundings obtained at five stations for a day during SJVAQS/ AUSPEX. These stations lie along a line running roughly east-northeast from Oakland, or approximately perpendicular to the California coastline and parallel to the mean wind direction in this area (for reference see Figure 17). We chose the stations at Oakland (OAK), Livermore (LI2), Brentwood (BRE), Stockton (STO), and Pardee Reservoir (PAR) because they are more or less free from obvious terrain influences and are representative of soundings throughout the SJV.

We analyzed the depth of the convectively unstable mixed layer from the observed temperature profiles using the following conventions. First, the average temperature of the two lowest levels in the sounding was calculated. For convectively unstable boundary layers over land, this gave a representative temperature for the atmospheric surface layer. However, if the sounding showed that the surface layer was strongly superadiabatic, then we replaced the surface-layer temperature with the temperature at the top of the superadiabatic layer plus 1.5 C. This averaged surface-layer parcel was then lifted dry adiabatically until it reached the point aloft where it intersected the sounding. We found that this intersection generally coincided with the base of the stable layer capping the mixed layer, even if that stable layer was fairly weak. For our purposes, this level was defined as the top of the mixed layer.

Figure 20 shows an example of temperature profiles observed at Oakland on August 5 as the high-ozone episode in the SJV was approaching its peak intensity. The soundings at 0400 and 1000 LST both show a shallow marine layer of about 290-300 m, capped by a very strong inversion of 15 °C, which is about normal for this part of the California coast in summer. The marine-layer depth at this coastal station actually develops a minimum during the afternoons (not shown), when the sea breeze reaches its maximum intensity and causes net horizontal divergence in the cool air at the shoreline. The horizontal divergence, in turn, causes the inversion base to fall. The continuous inflow of marine air during this flow pattern keeps the boundary layer at Oakland rather cool and shallow throughout the diurnal cycle. Although there is no sounding available at this site at 1600 LST on 5 August, examination of the days before and after suggest that the mixed-layer depth at Oakland generally remained about 300 m at this time of day.

Meanwhile, Figure 21 shows temperature profiles on 5 August at Livermore, which is only about 35 km inland from Oakland. The temperature profiles from the nocturnal hours (0100 and 0400 LST) have very cool surface temperatures capped by a strong inversion at about 300 m AGL, similar to those found in the coastal soundings at Oakland. Thus, in the absence of surface sensible heating, the marine layer is advected this far inland at night with very little modification. However, examination of the soundings at 1000 and 1600 LST reveals that the surface is heated rapidly during the daytime, reaching almost 36 °C by 1600 LST (0000 UTC 6 August). Nevertheless, on this afternoon the depth of the mixed layer remains only ~370 m. Above the top of the mixed layer, the 1600 LST sounding at Livermore is only weakly stable for another 700 m, but that is sufficient to prevent penetration by boundary-layer eddies. It should also be noted that the advective time scale for marine air to travel from Oakland to Livermore, assuming a mean speed of only 5 m s^{-1}, is about 2 h. This emphasizes how rapidly the shallow column of marine air undergoes heating as it travels to Livermore.
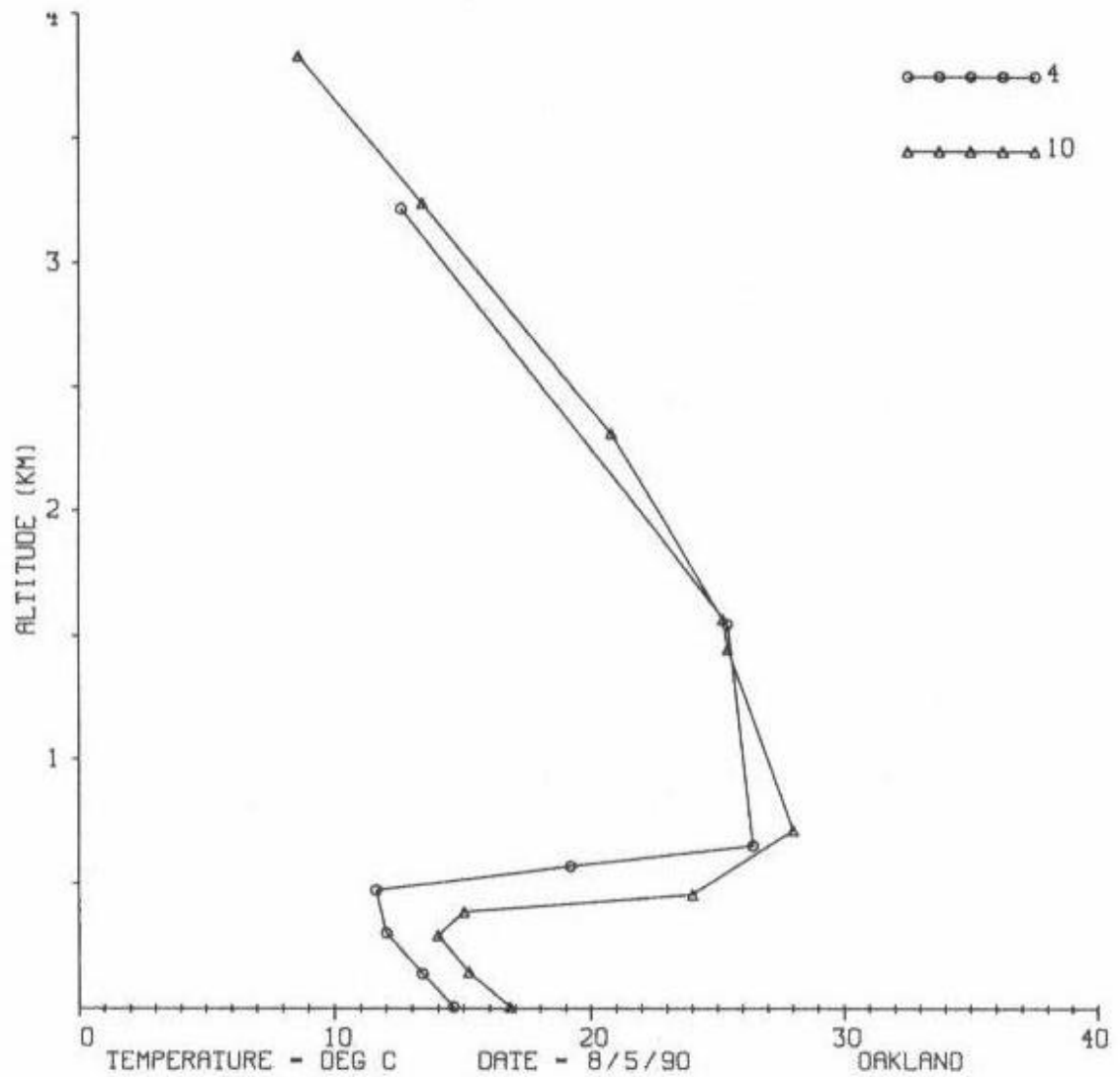
Figure 20. Observed temperature sounding © at Oakland on 5 August 1990. Times are given as local standard time.
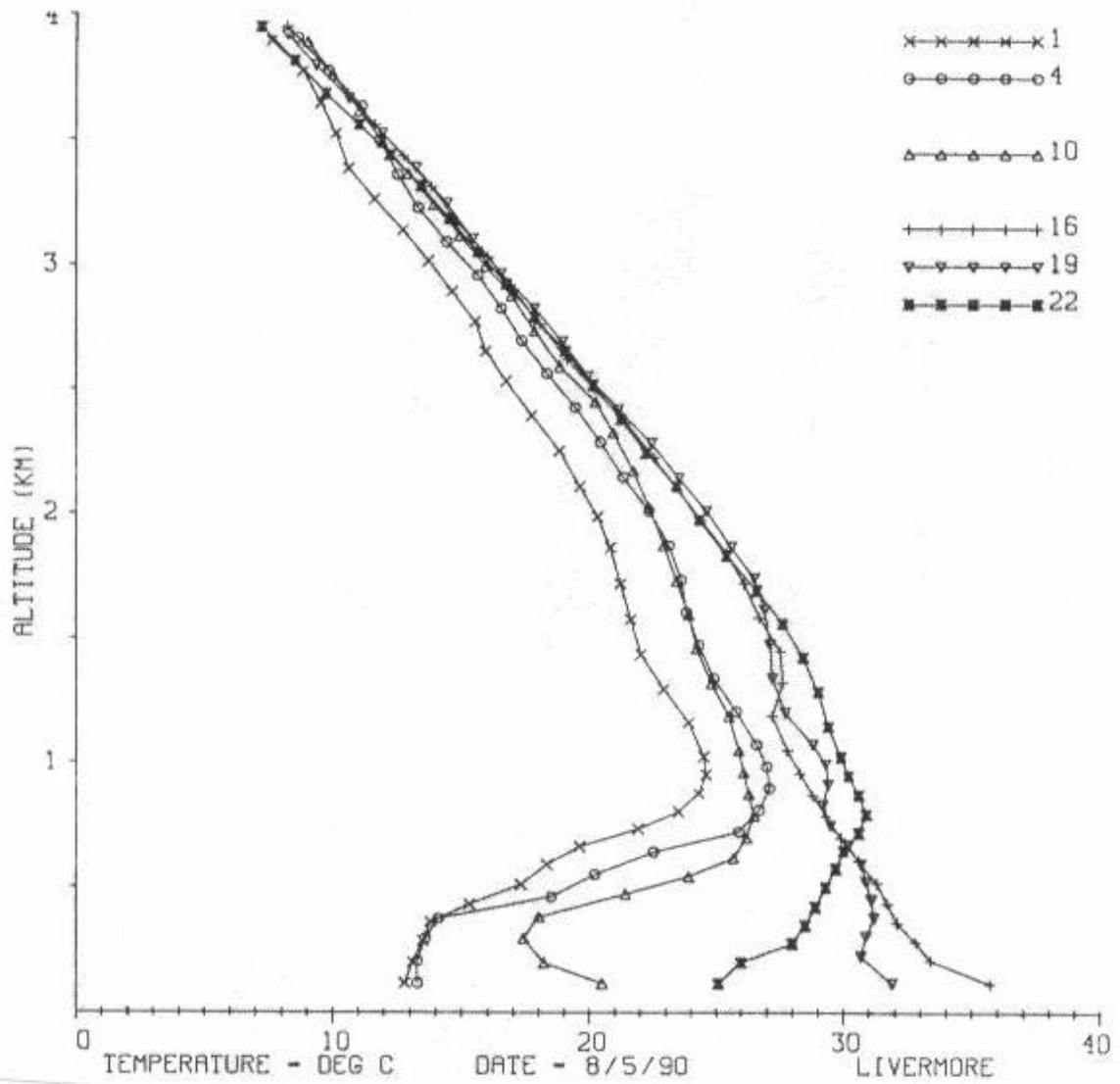
Figure 21. Observed temperature soundings (C) at Livermore on 5 August 1990. Times are given as local standard time.

From the observations shown for Oakland and Livermore, it seems easy to assume that a much deeper mixed layer must lie only a short distance farther inland, where the effects of surface sensible heating would have acted longer on the rapidly modifying marine air. The next available inland sounding site is at Brentwood, which lies about 55 km east of Oakland (Figure 22). Again, cool temperatures in the shallow nocturnal boundary layer rise rapidly following sunrise. By 1600 LST, the surface temperature has climbed to a maximum of 39.5 °C. However, despite this very high temperature, the mixed-layer depth at this time is only ~500 m AGL. Even though the capping inversion is only about 1 °C, notice that the air above that level is clearly stable. Thus, despite the hot surface temperature, the afternoon boundary layer remains shallow because the air only a few hundred meters above is potentially even hotter.

In the center of the northern SJV about 85 km from Oakland lies Stockton, for which the temperature profiles on 5 August are shown in Figure 23. The same cool nocturnal low-level temperatures also are found lying below a strong nocturnal inversion at this site. Again, as daytime temperatures reach their maximum of 35.5 °C at 1600 LST, the boundary layer is capped by still warmer air farther aloft. The mixed-layer depth at this time is only 390 m and the inversion layer is the strongest found at any of the four inland stations examined.

Lastly, the temperature profiles for 5 August for the easternmost site at Pardee Reservoir, 135 km from Oakland, are shown in Figure 24. This site lies in the western foothills of the Sierra Nevada Mountains ~350 m above sea level. Because of the distance from the coast and the elevation, there is no indication of the very strong nocturnal inversion noted at Stockton and westward (see 0100 and 0400 profiles), and minimum surface temperatures before sunrise remain above 21 °C. By 1600 LST (0000 UTC 6 August), however, the surface temperature at Pardee Reservoir has reached a maximum of 40 °C. At this site the afternoon mixed-layer depth is 780 m AGL, with a 2-3 °C capping inversion.

3.3.5 Results of Experiments

3.3.5.1 Numerical Factors Influencing Mixing-Depth Simulations

Our examination of the MM5 model results began with an evaluation of Experiment 1. Notice from Table 1 that Experiment 1 was designed to include all of the factors that were hypothesized to make a positive contribution toward accurate simulation of the shallow mixed layers found in the SJV (also see Section 2). Therefore, the goal of Experiment 1 was to learn whether the mesoscale model, with improved physics, enhanced grid configurations, and better initialization and FDDA, could more accurately simulate the depth of the mixed layer in the SJV during episodes having poor air quality. If this experiment were successful, then comparisons with the other six experiments would allow us to identify the most important factors contributing to this result.

First, we examine the influence of the MBLI during the 12-h dynamic initialization phase of Experiment 1 using Figures 25 and 26. These figures show a west-east cross section of potential temperature, q, on the 4-km domain. The section is located along Bakersfield. In Figure 25, the cross section shows the q-field at 1200 UTC 2 August 1990, at the beginning of the 12-h dynamic.
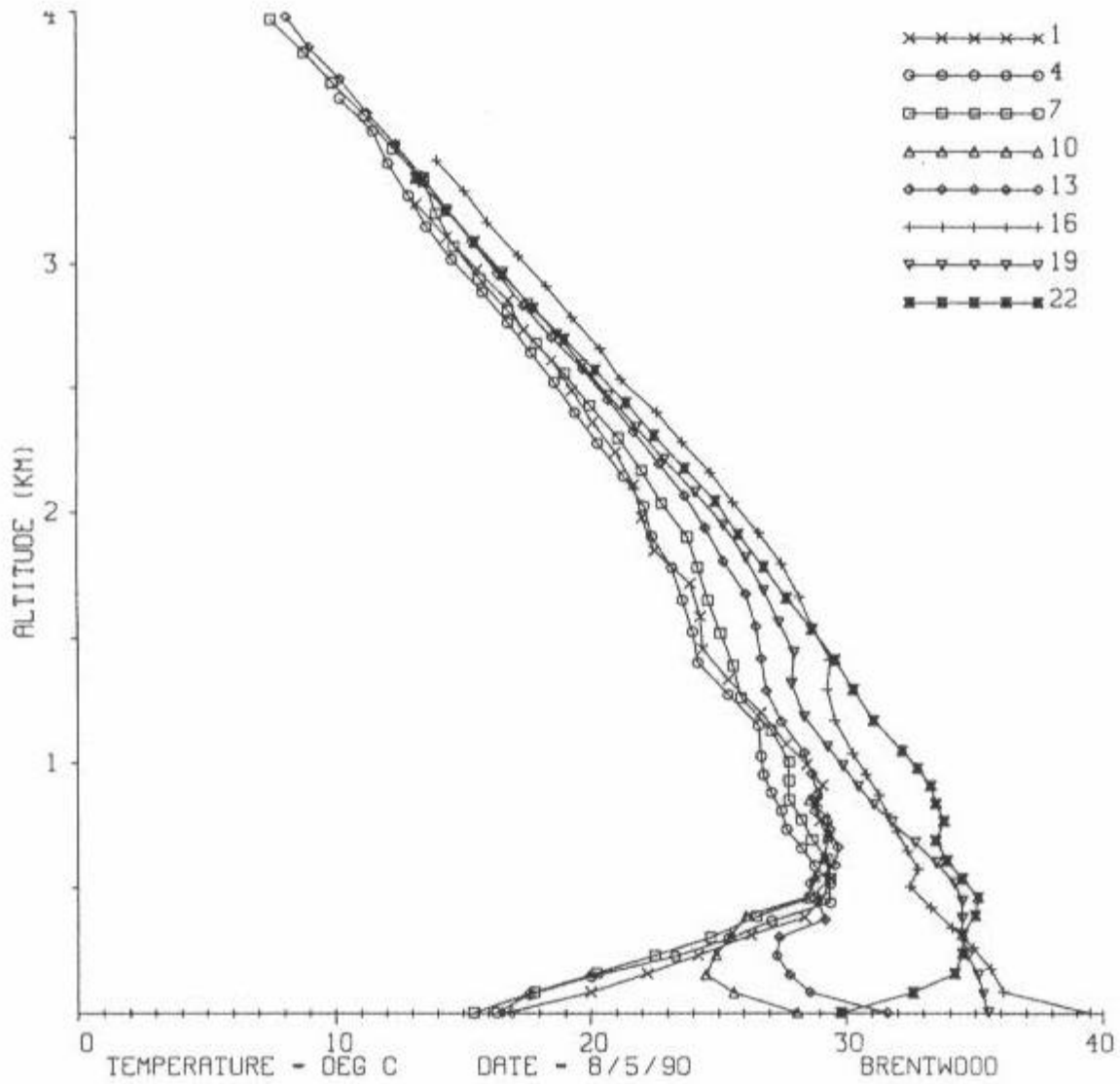
Figure 22. Observed temperature soundings (C) at Brentwood on 5 August 1990. Times are given as local standard time.
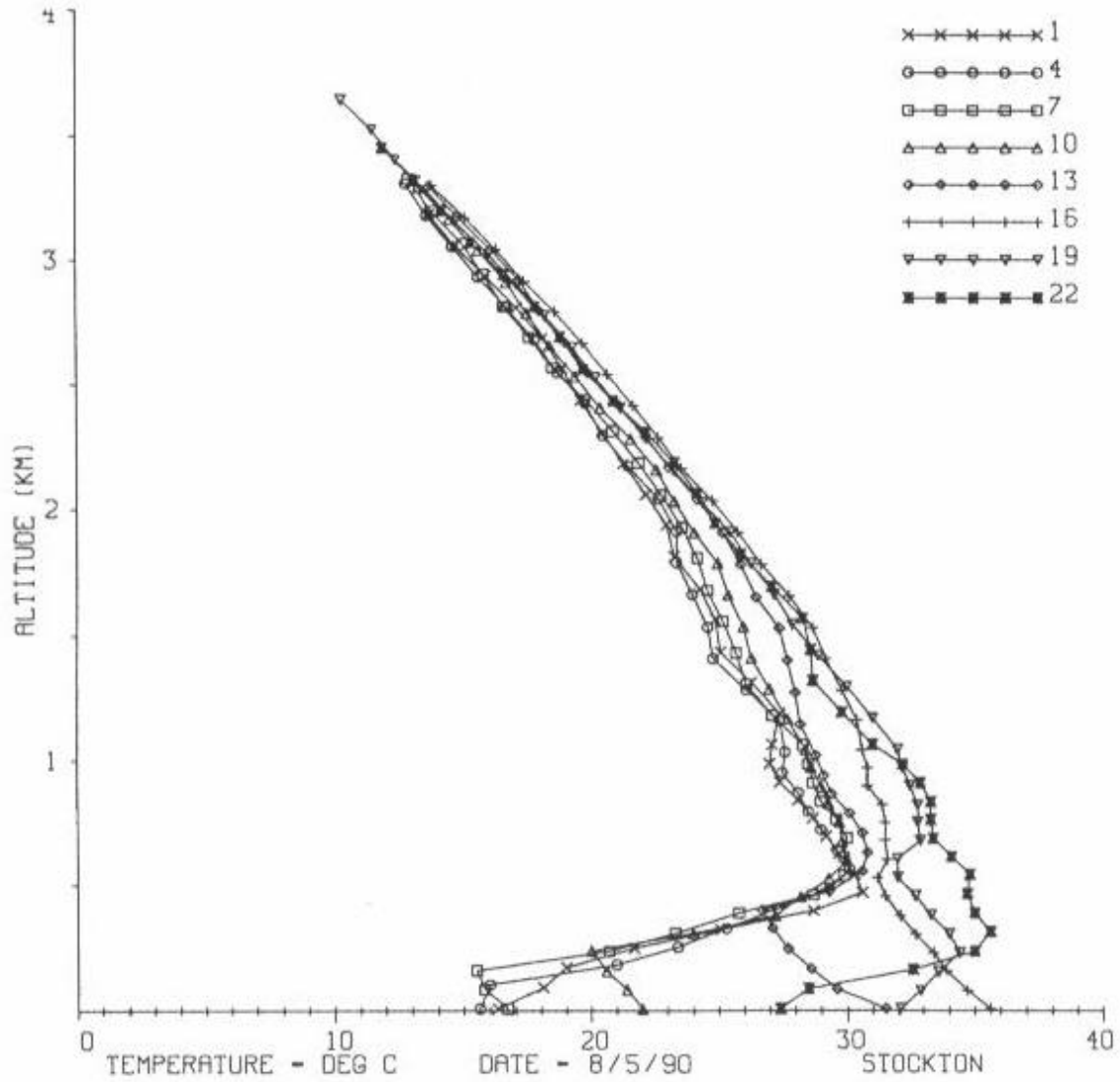
Figure 23. Observed temperature soundings (C) at Stockton on 5 August 1990. Times are given as local standard time.
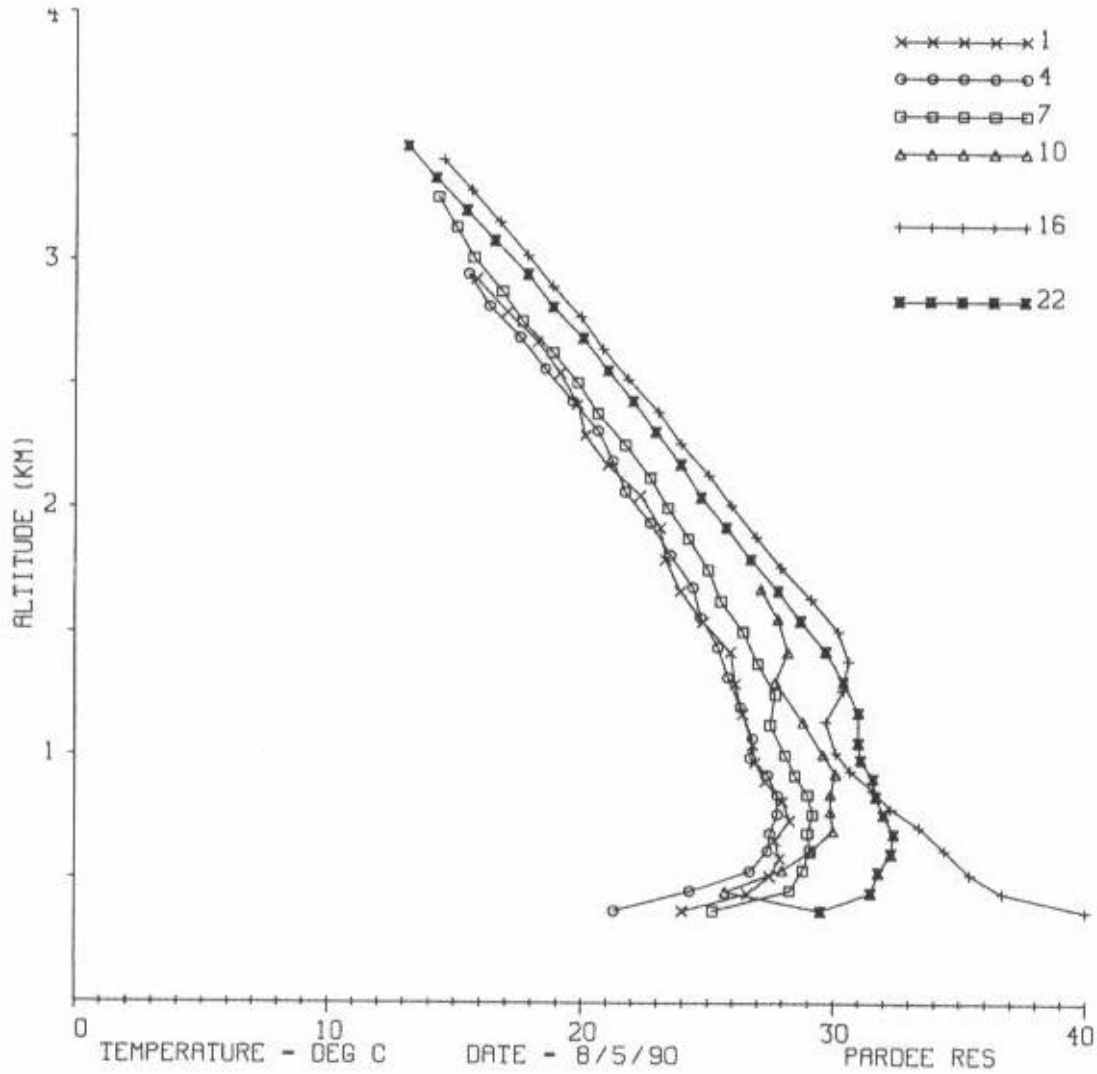
Figure 24. Observed temperature soundings (C) at Pardee Reservoir on 5 August 1990. Times are given as local standard time.

```
(X1,Y1)=( 13, 37) (X2,Y2)=( 50, 37) THETA    (K      | 90080212 = 90080212 +   0.00H  SM= 0
```

SARMAP 4km MM5V2 62 LAYER MBLI

CONTOUR FROM   286.00   TO   316.00   CONTOUR INTERVAL OF   1.0000   PT(3,31=   287.15

Figure 25. Vertical cross section of the MM5 initial potential temperature (K) below 700 mb for Exp. 1 on the 4-km domain at 1200 UTC 2 August 1990, before application of the MBLI dynamic initialization. Location is along the Bakersfiled. Isentrope interval is 1 K.
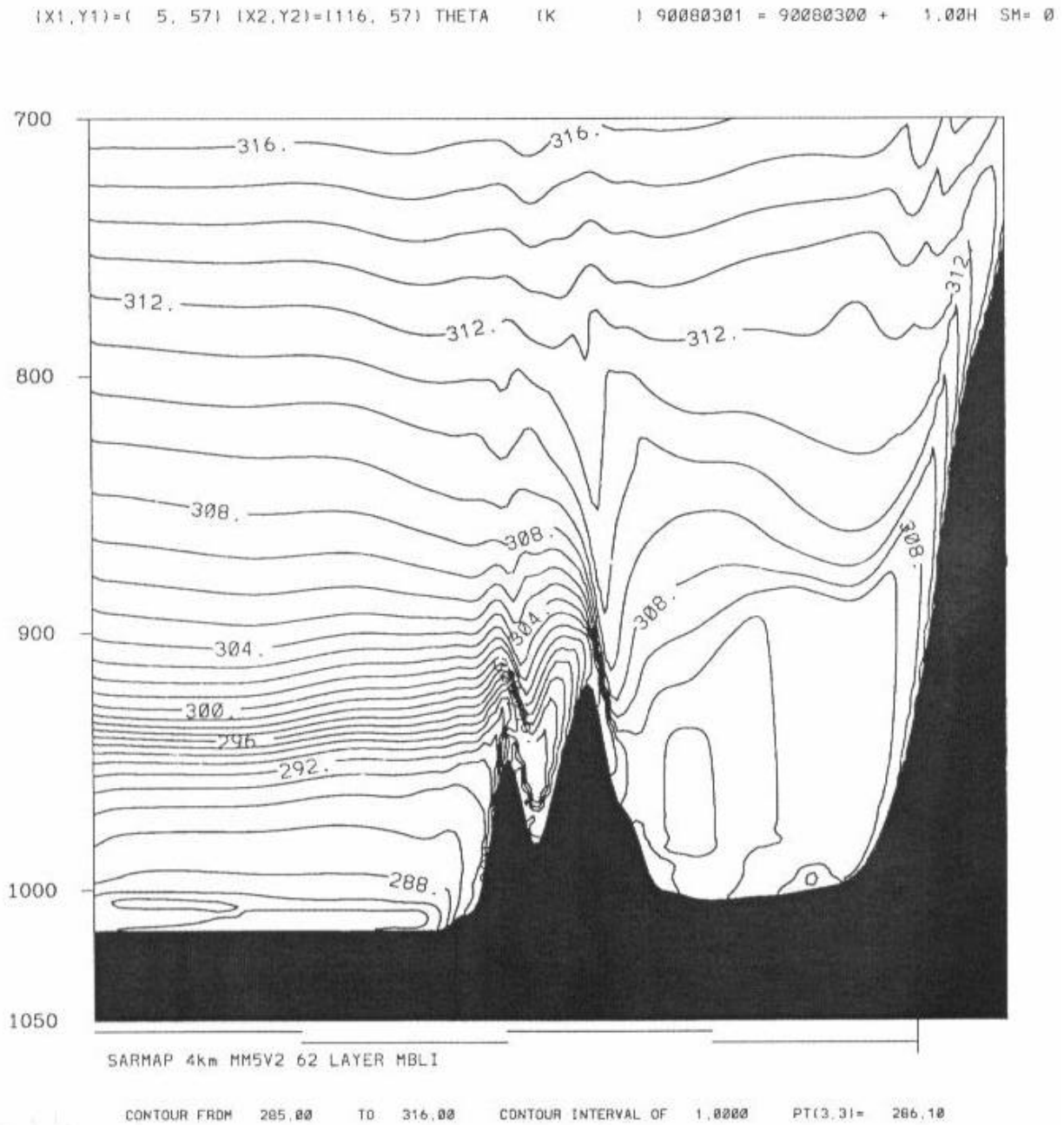
Figure 26. Vertical cross section of the MM5 potential temperature (K) below 700 mb for Exp. 1 on the 4-km domain at 0000 UTC 3 August 1990, after the 12-h application of the MBLI dynamic initialization. Location of the cross section is shown in Figure 18. Isentrope interval is 1 K.

initialization period over which the MBLI is applied. Notice that it reveals a shallow stable MABL confined below 1000 mb over the ocean (left side of the figure). By the end of the 12-h MBLI period, Figure 26 indicates that the MABL has become approximately moist adiabatic and is far less stable. As noted in Section 2, this more realistic MABL structure may contribute to the shallow inland mixed-layer depths, but determination of that contribution must await examination of the other sensitivity experiments. Notice that Figure 26 also shows that the afternoon mixed-layer depth at 0000 UTC, 3 August (1600 LST) has grown to ~112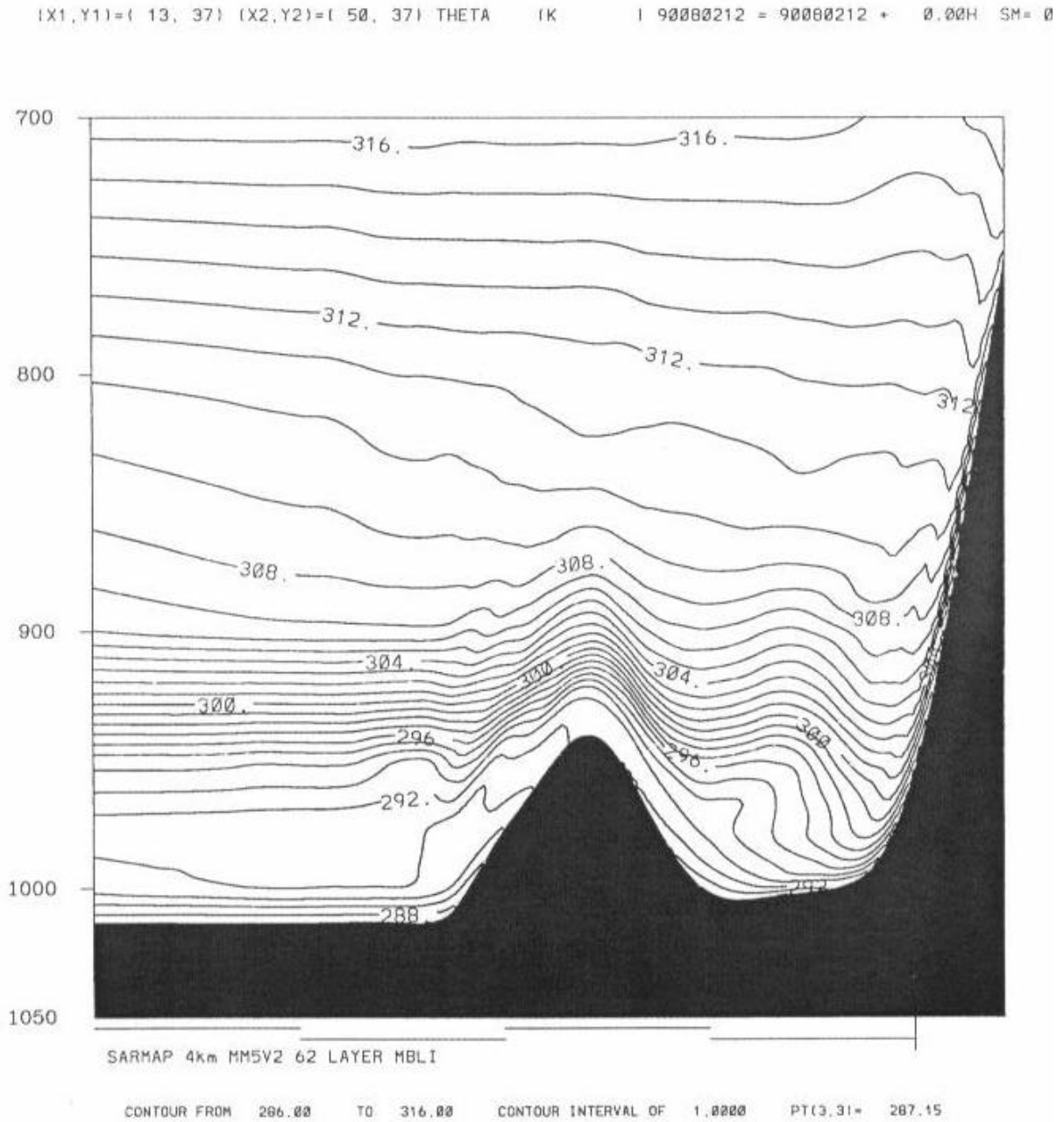5 m in the center of the SJV. Most of the remaining model evaluations concentrate on the second and third days following the MBLI period (0000 UTC 5-6 August), when the high-ozone episode was building toward its maximum intensity and mixed-layer depths over land were becoming steadily lower.

Figures 27 and 28 show that, 72 h after the end of the dynamic initialization, the horizontal solutions for temperature and wind over the Sacramento Valley and SJV are realistic for this case. In Figure 27, the surface-layer temperature at 0000 UTC 6 August (approximately the time of the peak of the high-ozone episode) shows maximums of 35 °C in the SJV and 41 °C in the Sacramento Valley. Figure 28 indicates that the model reproduces the divergent wind flow commonly observed east of San Francisco Bay and the 2-5m s^{-1} divergent northwesterly low-level winds in the SJV. The latter is the typical response caused by superposition of two types of mesoscale forcing: (1) northwesterly mean flow in the SJV due to the thermal low-pressure center near Bakersfield, and (2) low-level divergence caused by two independent valley breezes induced by the heated mountain ranges flanking the valley. Thus, these figures indicate that the basic wind and temperature patterns are consistent with observations and with results of previous modeling studies (e.g., Seaman et al. 1995).

Next, Figure 29 shows the horizontal distribution of mixed-layer depth simulated by MM5 in Experiment 1 at 0000 UTC 6 August (1600 LST 5 August) 1990. This figure can be compared to the observations and MM5 results from Experiment 7 performed by Seaman et al. (1995), which are shown in Figure 16. It is apparent upon examination of Figures 16 and 29 that the mixed-layer depths simulated over the SJV in Experiment 1 are generally lower than in Experiment 7. However, the complexity of the pattern makes it very difficult to draw objective conclusions. Therefore, we performed a statistical analysis of the mean error (*ME*) and mean absolute error (*MAE*), as defined by Stauffer and Seaman (1990), on the simulated mixed-layer depths for the experiments (Table 2).

Table 2 shows that the *ME* (a measure of the bias) in Experiment 1 is only 56 m, compared to 304 m in Experiment 7. The large positive *ME* in Experiment 7, which implies that the MM5-simulated meteorology contributes to significant overdilution of pollutants when used to drive an air chemistry model, was the primary motivation at CARB to conduct the present study.

SIGMA =0.997 T (C) 90080600 = 90080300 + 72.00H SMOOTH= 0

SARMAP 4km MM5V2 62 LAYER MBLI

CONTOUR FROM 8.0000 TO 40.000 CONTOUR INTERVAL OF 2.0000 PTI3,31= 16.011

Figure 27. MM5-simulated surface-layer temperature (C) at 10 m AGL for Exp. 1 on the large 4-km domain at 0000 UTC 6 August 1990 (72 h after the MBLI period). Isotherm interval is 2 C.
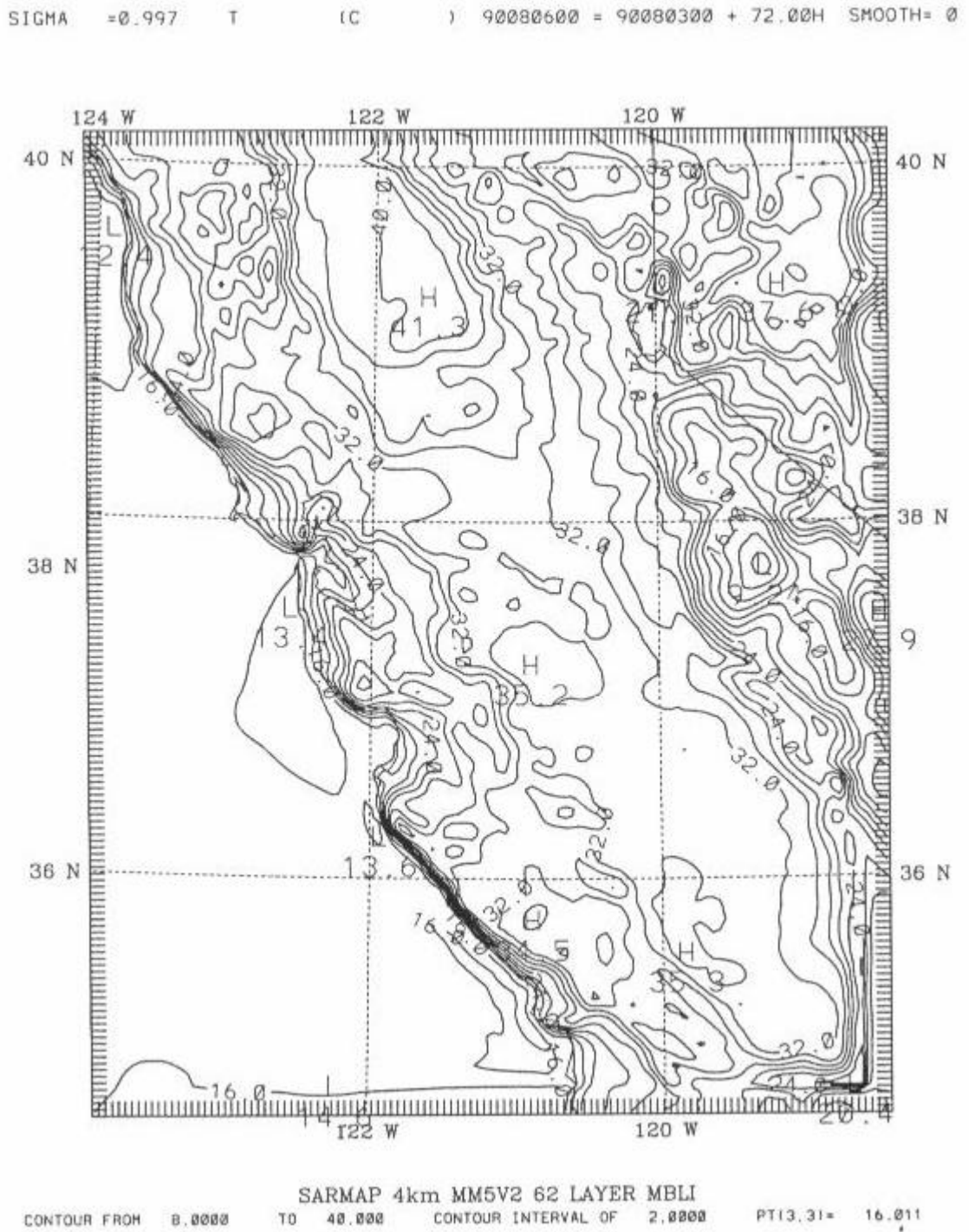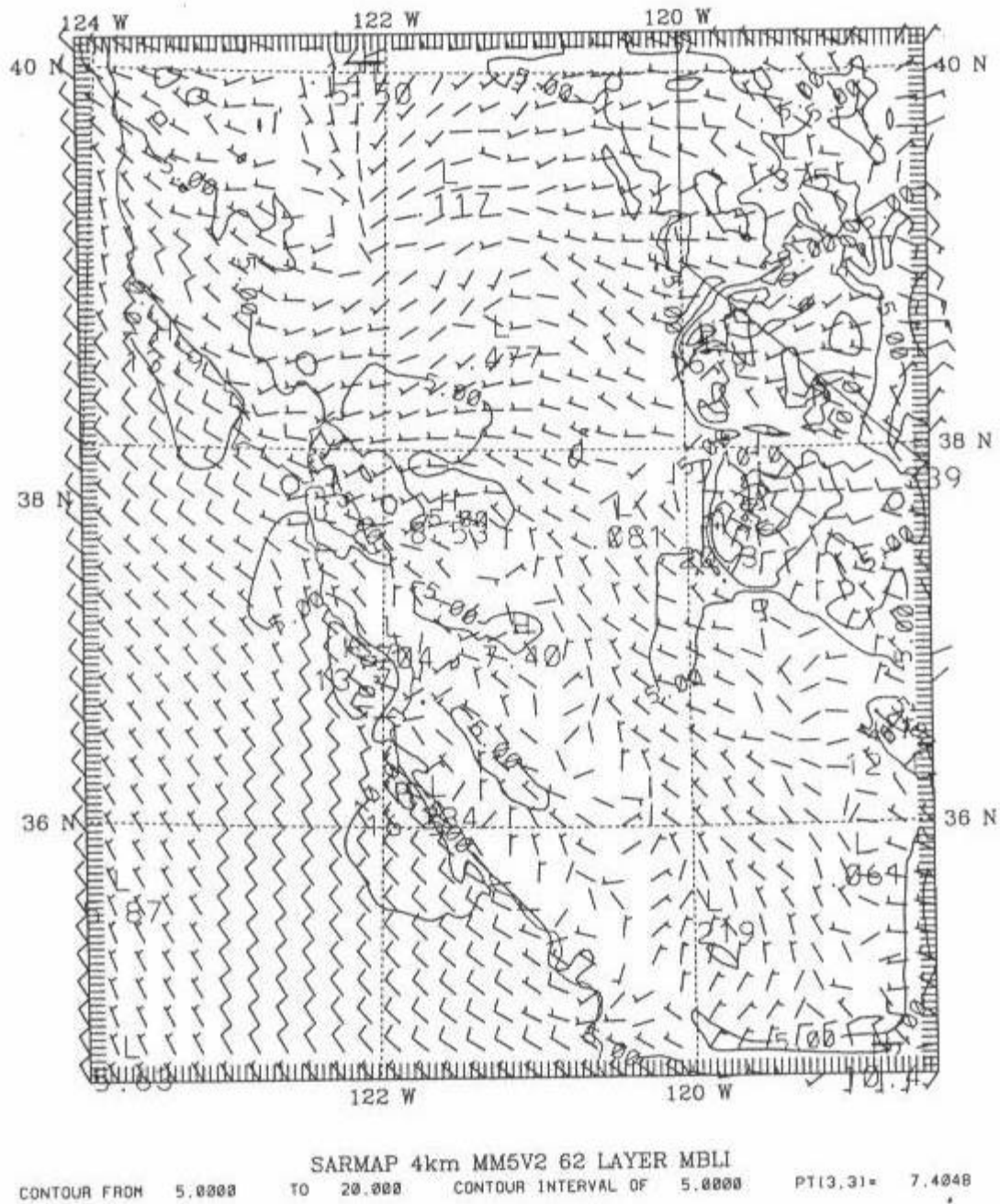
Figure 28. MM5-simulated surface-layer winds (m/s) at 10 m AGL for Exp. 1 on the large 4-km domain at 0000 UTC 6 August 1990 (72 h after the MBLI period). Isotach interval is 5 m/s.

Figure 29. Mixed-layer depth (m) simulated by the MM5 at 0000 UTC 6 August 1990 in the 4-km domain for Exp. 1. Contour interval is 200 m.

Table 2. Errors in model-predicted mixed-layer depths (model minus observations) for upper-air sites in the SJV at 0000 UTC 6 August (1600 LST 5 August) 1990.

Station ID	Obs'd Mixed-Layer Depth (m)	Exp. 1 Error (m)	Exp. 2 Error (m)	Exp. 3 Error (m)	Exp. 4 Error (m)	Exp. 5[a] Error (m)	Exp. 6 Error (m)	Exp. 7 Error (m)
PTB	140	+30	+10	+0	+10		+20	+80
OAK	290	-90	-140	-110	-110		-100	-75
LI2	370	+20	+0	+0	-170		+10	+200
BRE	500	+120	-100	-50	+450		+110	+320
ALT	590	-190	-220	-210	-210		-15	+210
STO	390	+210	+60	+190	-290		+240	+490
PAR	780	-190	-130	-100	-680		+145	+30
WOO	440	+60	+60	+50	-290		+200	+410
ANG	400	+120	+30	+200	-220		+50	+410
MRG	340	+60	+60	+40	+40		+80	+270
CRO	370	+350	+210	+280	+190		+380	+530
PA2	220	+355	+180	-20	+600		+460	+580
ORO	560	-60	+50	+300	-380		+190	+415
MAR	780	+200	-400	-240	-130		-55	+90
MAD	800	-130	-390	-580	-200		+80	+200
KIN	170	+210	+150	+70	+100		+215	+430
THR	410	+230	+5	-30	+0		+300	+530
TUL	630	+200	-50	-60	-190		+210	+380
VIS	310	+340	-120	-80	+270		+470	+920
DEV	680	-105	+70	-80	-600		-40	+90
DEL	720	+90	-220	-410	-130		+50	+190
BUT	850	-190	-250	-540	-460		-250	-70
ME (m)	--	*+56*	*-52*	*-63*	*-109*		*+125*	*+304*
MAE (m)	--	*161*	*132*	*165*	*260*		*167*	*317*

[a] The results of Experiment 5 had been lost by the time of this writing. The experiment is being performed a second time in order to obtain the missing statistical data and complete the table.

[b] *ME* = mean error, *MAE* = mean absolute error.

Station ID's are listed in geographical order from north to south.

The reduction of this bias by nearly 82% in Experiment 1 is a very significant improvement in model skill. At the same time, the *MAE* (a measure of the average size of the individual errors) in Experiment 7 has been reduced by half in Experiment 1, from 317 m to 161 m. Considering that the model's vertical resolution is 40 m and the accuracy with which the observations can be used to estimate mixed-layer depth is imperfect, these results appear to be very reasonable.

Further examination of the statistics in Table 2 reveals some very important information. Experiment 2 is identical to Experiment 1 except that the vertical resolution is reduced in the first kilometer so that the total number of layers is 32 instead of 62 (Table 1). However, despite the loss of vertical resolution, Experiment 2 actually produced slightly more accurate results than Experiment1 and had the lowest errors of any of the experiments in the study (*ME* = -52 m and *MAE* = 132 m). Also, the sign of the *ME* changed from positive to negative, meaning that Experiment 2 somewhat underestimated the depth of the mixed layer. Although the improvement in skill found for Experiment 2 compared to Experiment 1 is probably not statistically significant, this result is important nevertheless because it means that very high vertical resolution in the model is unnecessary to obtain accurate simulations of the SJV boundary -layer structurre and the related mesoscale circulations.

Next, comparison of Experiments 2 and 3 allowed isolation of the model's sensitivity to the MBLI over the Pacific Ocean. Table 2 shows that the removal of the MBLI in Experiment 3 caused the *ME* and *MAE* to become slightly degraded, but the amount is so small that this technique is probably unnecessary for most air quality studies in the SJV. This result is consistent with the observational evidence presented in Figures 20-24, which demonstrated that the cool marine air is modified very rapidly as it is advected onshore, so that the marine layer retains little of its original structure in the daytime once it reaches the SJV. However, comparison of the statistics from Experiments 3 and 4 reveals that there is a significant loss of accuracy when the 108-km outermost domain is removed. In fact, the *ME* in Experiment 4 is –109 m, meaning that for this case the model significantly underestimated the mixed-layer depth across the 4-km grid when the large-scale dynamics of the East Pacific Ridge were not contained fully within the outermost 108-km domain. The implication is that the subsidence induced by the large-scale dynamics was inaccurate (possibly overestimated) in this experiment. While an impact due to the size of the outer domain was not unexpected, it is surprising that its exclusion caused such a serious *under*estimate of this key variable. It cannot be assumed that the sign of the error would be the same in all cases, but it appears that use of a larger outer domain can be a valuable factor to ensure that the dynamics of the anticyclone are simulated well and are consistent with other scales of motion.

Comparison of Experiments 4 and 6 reveals a large shift of the *ME* from negative (-109 m) to positive (+125 m). Although results of Experiment 5 have been lost (they are being re-created), it is very likely that most of this large change in the *ME* can be traced to the inclusion of the FDDA strategy in Experiment 6. That is, when the analysis-nudging performed on the 12-km grid (and on the coarser domains) was allowed to push the model solutions toward the synoptic-scale analyses below 1500 m AGL (above the mixed layer) in Experiment 6, the mesoscale influences on the capping inversion above the boundary layer was weakened. Subsequently, horizontal advection carried the degraded (smoothed) mid-level thermal field into the 4-km domain, where it presented less inhibition to the growth of the SJV convectively unstable daytime mixed layer in this experiment.

Finally, comparison of statistics from Experiments 6 and 7 demonstrates the influence of changing the model's turbulence representation from the 1.5-order TKE scheme to the Blackadar nonlocal-closure scheme. Consistent with the results of Shafran et al. (2000), use of the Blackadar scheme in Experiment 7 caused a very

large increase in the positive bias for the mixed-layer depth (from +125 m to +304 m). In the Midwest U.S. cases studied by Shafran et al., however, a moderate subsidence inversion of 2-6 °C capped the convectively unstable boundary layer and may have helped reduce the magnitude of mixing-depth errors that could develop. In the August 1990 SJV case, on the other hand, Figures 20-24 showed that the capping inversion was often rather weak in the afternoons, so that this case presents a more difficult prediction problem for both turbulence schemes. In this challenging situation, the 1.5-order TKE scheme clearly performed rather well for this key variable.

3.3.5.2 Physical Processes Leading to Shallow Mixed-Layer Depths

Having determined the numerical requirements necessary for a mesoscale model such as MM5 to accurately simulate the occurrence of shallow mixing depths in the SJV, we next considered what might be the physical causes of those conditions. Examination of the 62-layer Experiment 1 provides an excellent opportunity to identify the dominant physical processes.   First, Figure 30 shows the TKE in the cross section through Fresno at 0000 UTC 5 August 1990 (1600 LST 4 August), during the period when the upper-level ridge is moving onshore over California. As anticipated, the TKE is small over the ocean, where the upwelling of cool water along the coast prevents strong surface sensible heat fluxes. Over land, however, the TKE shows the approximate depth of the convectively unstable mixed layer. The maximum TKE in the SJV is about 2.7 J kg^{-1} at this time. Notice that the large TKE values extend well above the inland Coast Range, where valley breezes directed up the east and west slopes converge and develop a strong buoyant plume of upward vertical velocities. It is not uncommon to find vertical motions reaching +1-2 m s^{-1} in this convergence zone over the mountain peaks (not shown). At the same time, Figure 31 shows the potential temperature, *q*, along the cross section, with the mixed-layer top indicated as a heavy dashed line. The depth of the mixed layer in the SJV at 0000 UTC 5 August ranges from about 700 m to 1000 m.

Over the following 24 h, in response to continued subsidence aloft, the isentropic surfaces and the mixed-layer depths are forced downward. First, Figure 32 shows that the TKE is very nearly as intense in the SJV at 0000 UTC 6 August (1600 LST 5 August) as on the previous day, with a maximum of 2.6 J kg^{-1}. The strong turbulence is consistent with the hot surface temperatures that are persistent during the episode. However, Figure 33 reveals that the mixed-layer depth in the cross section over the SJV at this time is as low as 450 m.

To better understand this change, compare the height of the 316 K and 312 K isentropic surfaces in the cross sections on these two afternoons (Figures 31 and 33). Over the ocean at the western boundary of the cross section (~200 km offshore), where mesoscale circulations associated with the California orography should be negligible, the 316 K isentrope is at virtually

(X1,Y1)=(5, 57) (X2,Y2)=(116, 57) GSTKE   (J/Kg   ) 90080421 = 90080300 + 45.00H SM=

```
700




800




900




1000



1050
```

SARMAP 4km MM5V2 62 LAYER MBLI

CONTOUR FROM 0.50000   TO   2.5000   CONTOUR INTERVAL OF 0.50000   PT(3,3)= -0.17772E-01

Figure 30. Vertical corss section of MM5 turbulent kinetic energy (J/kg) below 700 mb in Exp. 1 on the 4-km domain at 0000 UTC 5 August 1990 (48 h after end of dynamic initialization). Location of the cross section is shown in Figure 18. Contour interval is 0.5 J/kg.

Figure 31. Vertical cross section of the MM5 potential temperature (K) below 700 mb in Exp.1 on the 4-km domain at 0000 UTC 5 August 1990 (48 h after the end of dynamic initialization). Location of the cross section is shown in Figure 18. Isentrope interval is 1 K. Dashed line indicates the top of the mixed layer.
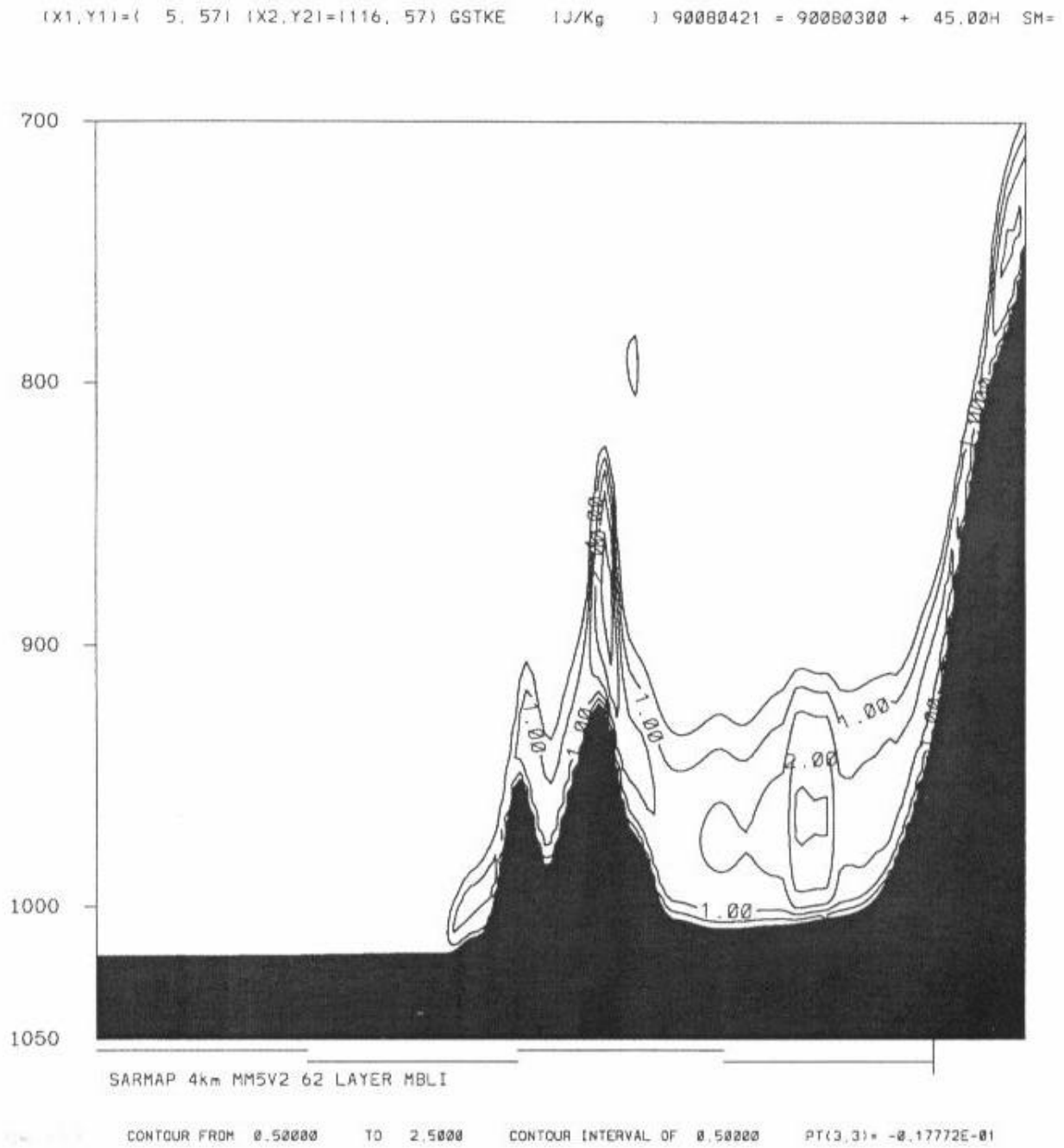
Figure 32. Vertical cross section of MM5 turbulent kinetic energy (J/kg) below 700 mb in Exp. 1 on the 4-km domain at 0000 UTC 6 August 1990 (72 h after dynamic initialization). Location of the cross section is shown in Figure 18. Contour interval is 0.5 J/kg.
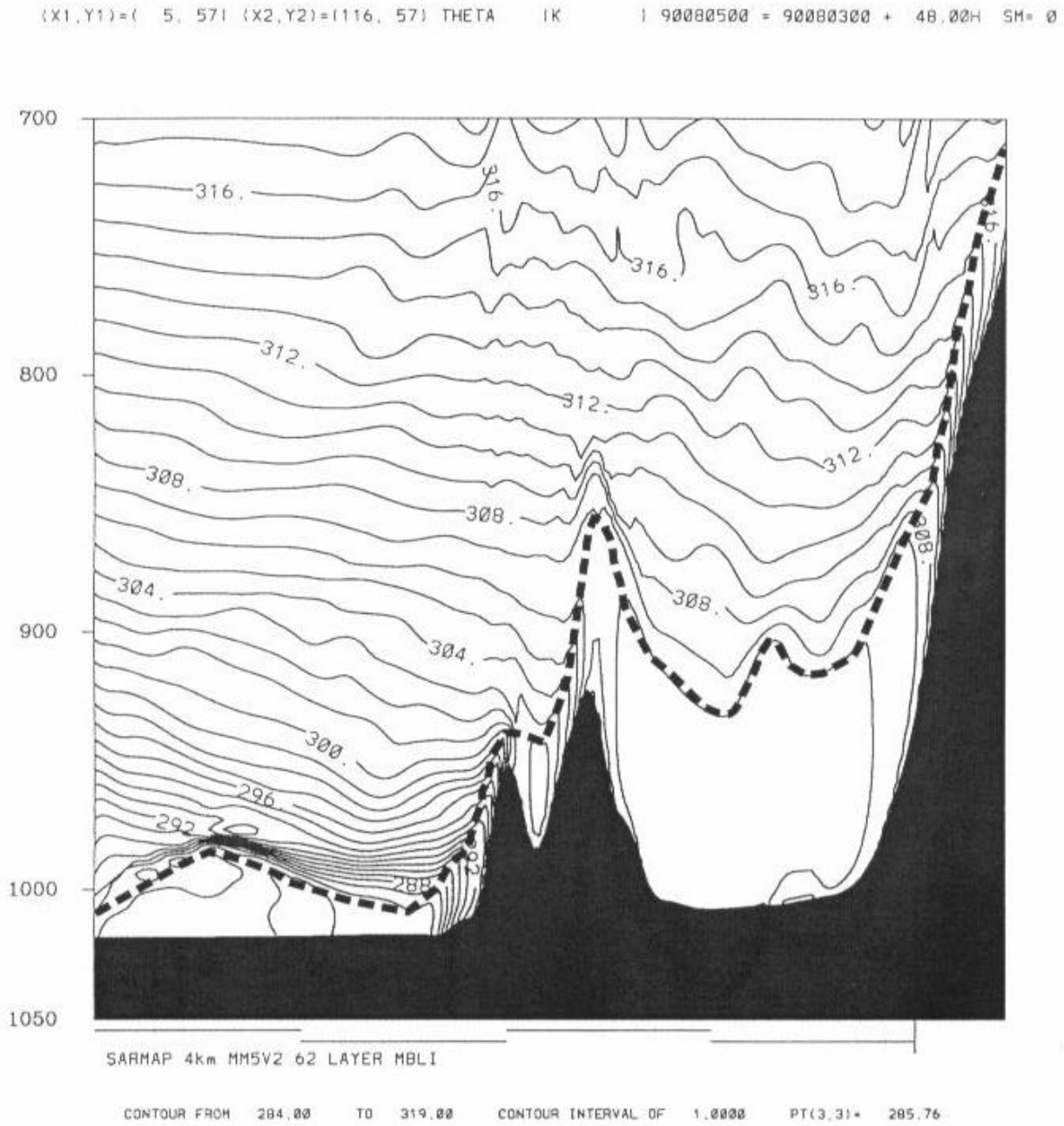
Figure 33. Vertical cross section of the MM5 potential temperature (K) below 700 mb in the Exp. 1 on the 4-km domain at 0000 UTC 6 August 1990 (72 h after end of dynamic initialization). Location of the cross section is shown in Figure 18. Isentrope interval is 1 K. Dashed line indicates the top of the mixed-layer.
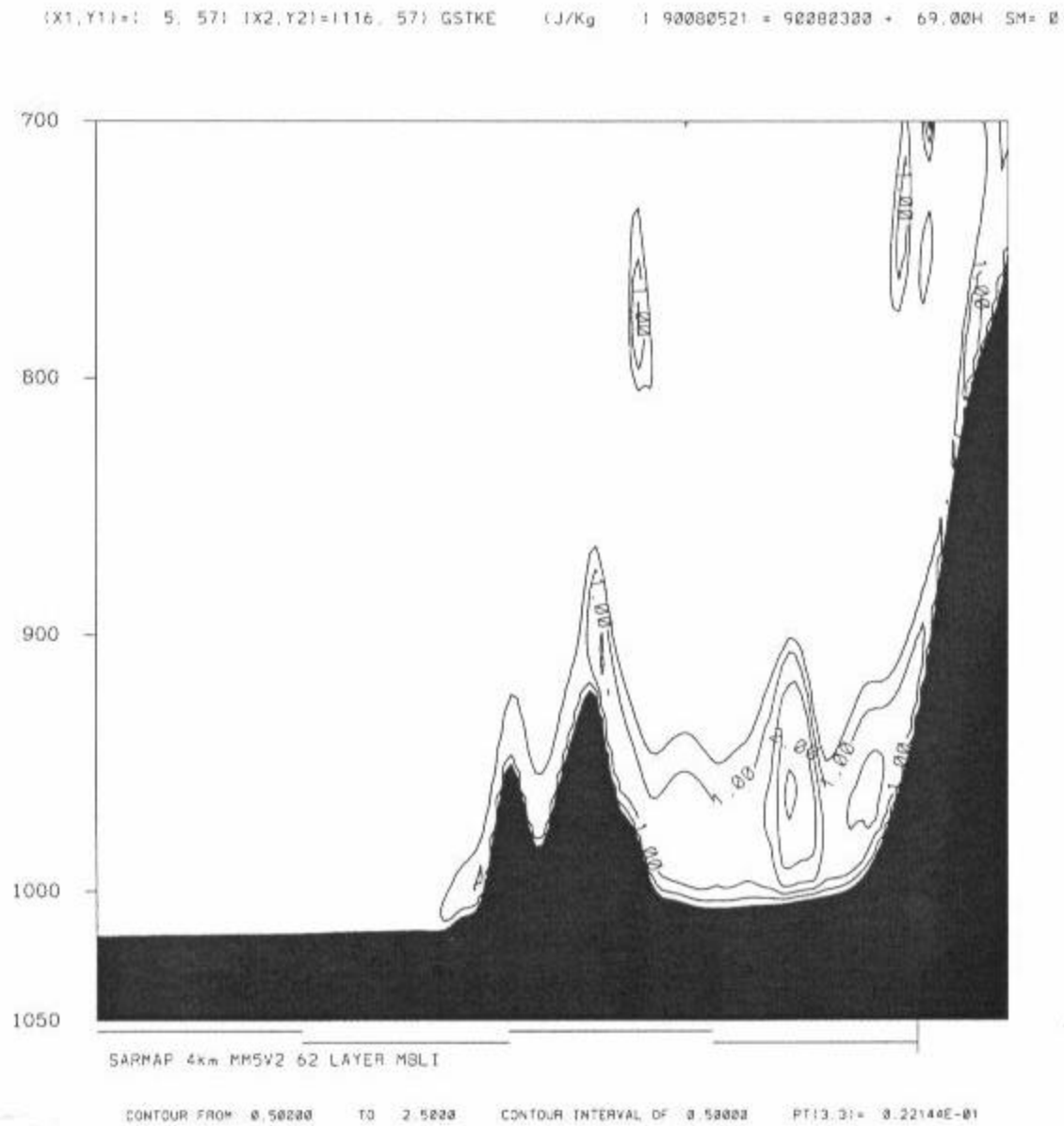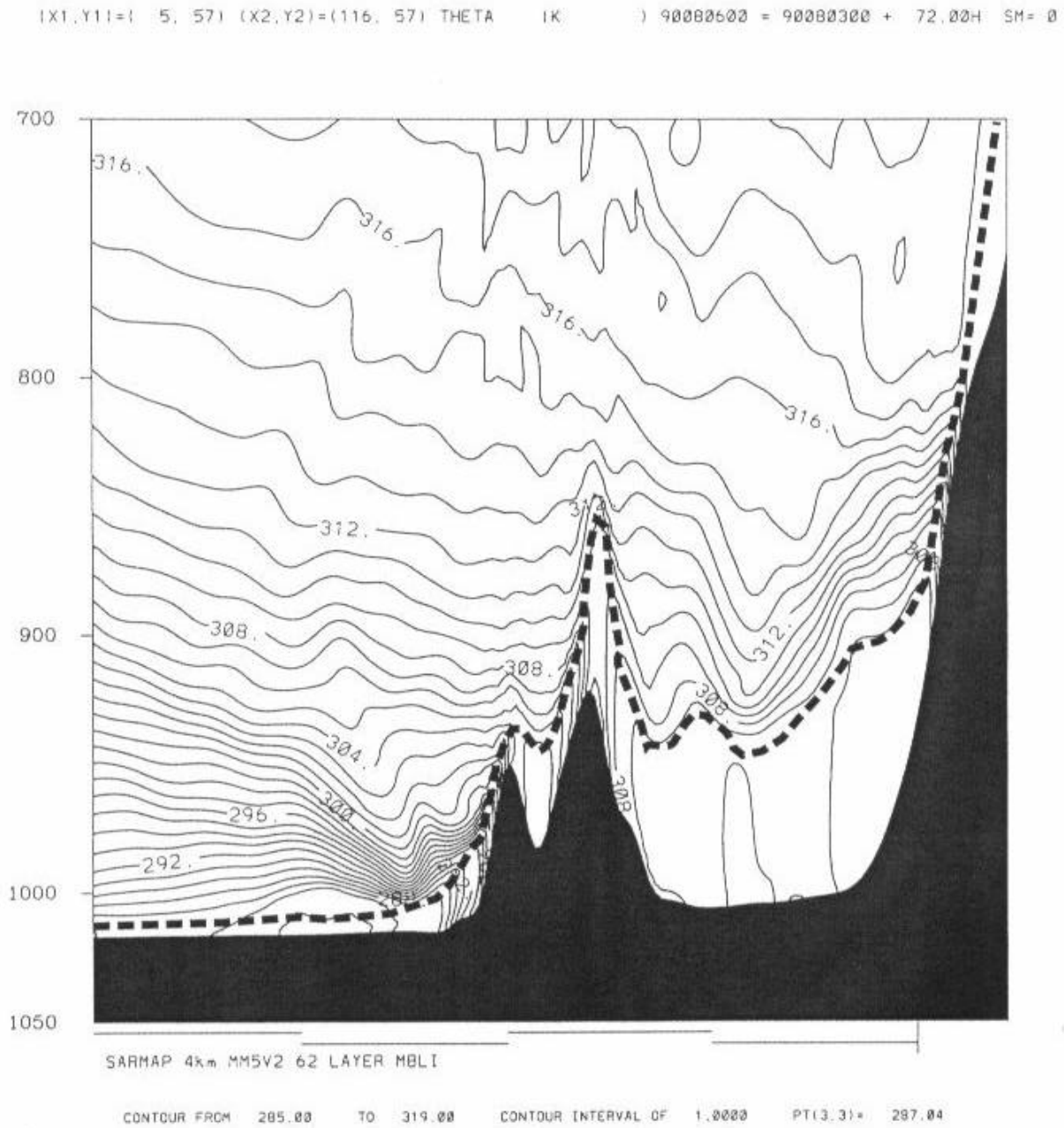
the same height on both days. Meanwhile the 312 K and 308 K isotherms between 900 and 800 mb have subsided about 435-440 m (see Table 3). The subsidence experienced in this area should be due almost entirely to the 3-D dynamics in the East Pacific Ridge. The 24-h local adiabatic warming in the layer is equivalent to a daily mean subsidence of about -0.51 cm s^{-1}.

Table 3. Change of heights of MM5-simulated isentropic surfaces (m) over the Pacific Ocean and over the SJV between 0000 UTC 5 and 6 August 1990 in Experiment 1. Values are calculated along the cross section shown in Figure 18.

Potential Temperature (K)	200 km West of CA Coast	San Joaquin Valley
316	+50	-565
312	-435	-730
308	-440	-380
304	-330	---

Notice in the figures that the isentropic surfaces slope downward from west to east (toward land). Table 3 also indicates that the subsidence in the cross section over the SJV is maximized for the 312 K surface, which is forced downward by 730 m over the 24-h period; this is equivalent to a daily mean rate of -0.85 cm s^{-1} over the valley. The stronger downward motion, compared to the oceanic region, represents the subsidence forced by the return branch of the mesoscale valley breeze circulation. Figure 33 suggests that the subsidence component due to the valley breeze is most intense in the central and eastern portions of the SJV, where the isentropic surfaces have dropped most rapidly. Of course, the mesoscale-induced subsidence should reach a maximum in the late afternoon when the upslope flow along the flanks of the mountain ranges is most intense, and then it should disappear at night. Thus, the mean mesoscale contribution over the valley (about -0.35 cm s^{-1}) must substantially underestimate the total rate during the afternoon. Because the mesoscale subsidence should be maximized over the SJV at about the same time as the daily maximum in surface heating, the combined subsidence-induced adiabatic heating aloft (synoptic plus mesoscale) should contribute significantly to raising temperatures directly above the convective boundary layer, thereby resulting in the especially low mixing depths in the valley.

Finally, Figure 34 shows the isentropic cross section from Experiment 6 at 0000 UTC 6 August (same time as in Figure 33). Recall that Experiment 6 does not include the large outermost domain (108-km mesh) or the large 4-km mesh and does not remove the analysis-nudging FDDA from the region below 1.5 km AGL (see Table 1). The sensitivity evaluation suggested that this set of conditions in Experiment 6 is less suitable for predicting shallow mixed-layer depths in the SJV. Figure 34 provides additional insight into this conclusion . In particular note that the 312 K isentropic surface in Experiment 6 does not slope downward from the ocean toward the SJV. This suggests that the mesoscale valley breeze is ineffective or has been neutralized in its role of reinforcing the synoptic-scale subsidence. However, examination of the model results confirms that the valley breeze in Experiment 6 develops in a realistic manner (not shown). Therefore, the most reasonable explanation for the result shown in
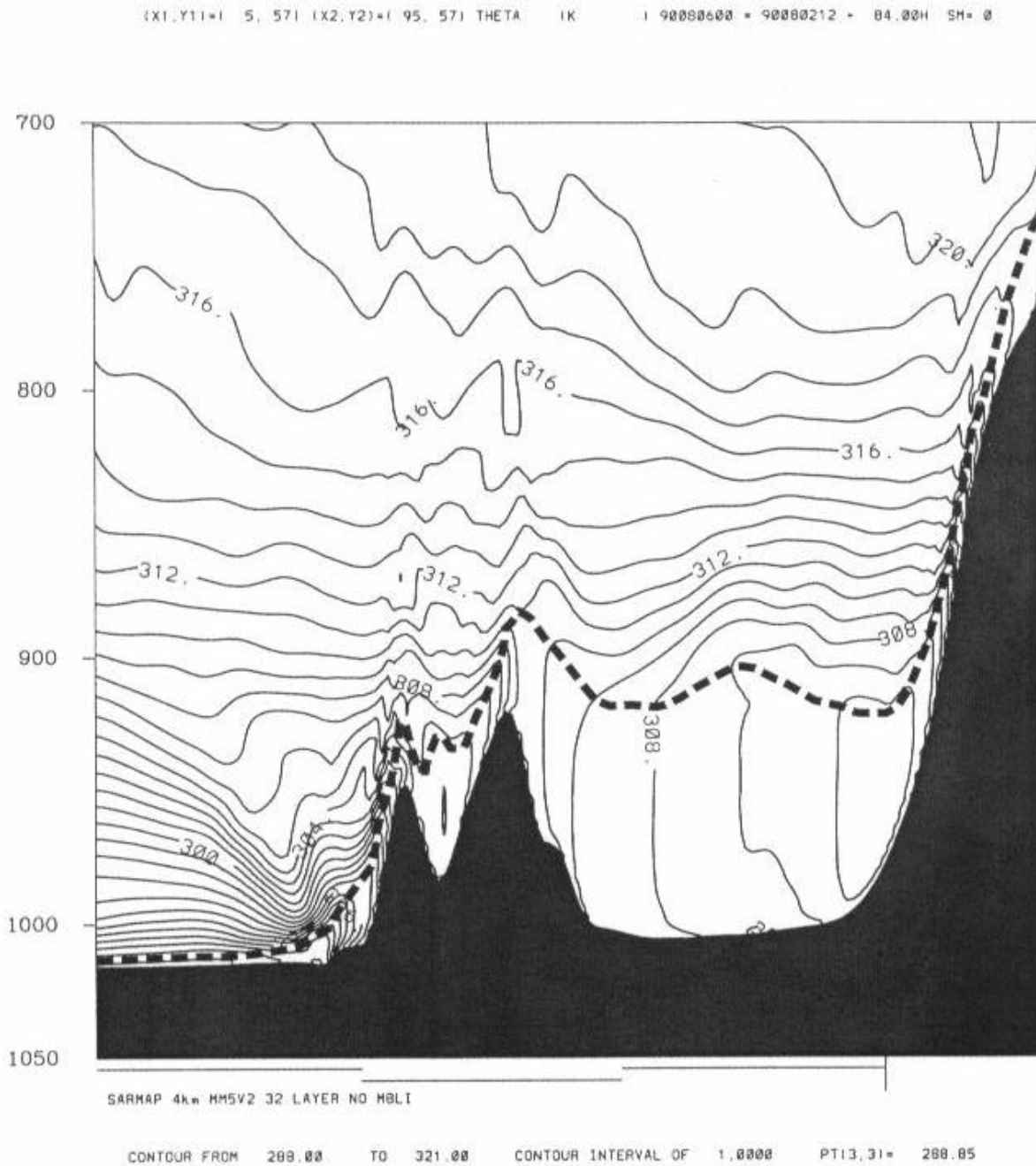
Figure 34. Vertical cross section of the MM5 potential temperature (K) below 700 mb in Exp. 6 on the 4-km domain at 0000 UTC 6 August (72 h after end of dynamic initialization). Location of the cross section is shown in Figure 18. Isentrope interval is 1 K. Dashed line indicates the top of the mixed-layer.

Figure 33 is that the poor analysis-nudging strategy used in this experiment acts to damp out the cumulative multiday impact of the mesoscale mountain-valley circulation on temperatures aloft in this region, as hypothesized in Section 3.3.1.6.

4. Summary

We followed two modeling strategies to determine reasons for the overestimation of mixed-layer depths by the mesoscale model MM5 over the central California region. In the first strategy, we performed sensitivity studies to understand the nature of some of the ABL errors and developed new techniques to improve the ABL simulation, using a 1-D model. When a simple land surface parameterization was used, simulation results for the Buttonwillow and FIFE sites indicated that a change of soil moisture availability by a factor of two led to large changes in simulated temperatures and mixing depths. Use of different mixed-layer formulations led to only minor differences between the simulations. However, the TKE-ε scheme performed better than the ACM-BKT scheme in predicting the surface features, as well as the ABL depth. Simulation results obtained by including a specified warming to represent the 3-D thermodynamics, due to synoptic–scale subsidence, also showed variability, depending on the type of mixed-layer schemes used in the simulations. Moreover, simulation results indicated that two different diagnostic methods of estimating the boundary layer depth yielded similar results in simulating the structures of the boundary layer. All these experiments indicated the presence of errors, with no assurance that a particular set of formulations can consistently provide accurate ABL structures.

Our new formulation to perform consistent adjustment of ground temperature, along with the assimilation of temperature and water vapor mixing ratio in the surface layer, mixed layer, and free atmosphere, led to very significant improvements in the simulated boundary layer depth and its structures. These results indicated that assimilation of the surface-layer data is possible when ground temperature is adjusted to reflect the changes in the surface-layer thermodynamic fields due to the data assimilation. Thus, we have shown that assimilation of surface temperature observations can be used successfully to adjust for uncertainties in surface characteristics, such as soil moisture specifications and inaccuracies in boundary layer parameterizations. This result has favorable implications for a number of data assimilation applications, including the development of improved meteorological conditions for air pollution modeling and meteorological analysis.

Another component of improvements in the model formulations is the proper estimation of surface latent heat fluxes, which control the mixed-layer depths. Our new formulation introduces vegetative effects in the equation that is being used in MM5 for estimating surface latent heat fluxes. This formulation uses many surface and vegetation parameters, as other sophisticated land surface schemes do. But the new formulation takes a diagnostic approach, providing two advantages over prognostic approaches; the diagnostic approach (1) is computationally inexpensive, and (2) controls or limits uncertainty present in the input data depicting surface and vegetation characteristics. Preliminary results obtained from the 1-D model simulations indicated very good improvement in the boundary layer predictions using this new methodology. Further research is in progress.

In the second modeling strategy, we performed several numerical simulations, using different configurations of MM5. Our first step was to determine the *numerical conditions* that allow

accurate simulation of the low mixed-layer depths in the SJV. The following are the most important findings of the numerical sensitivity experiments:

- No significant difference in skill was found when the number of layers was increased from 32 to 62 layers (higher resolution in the lowest km). Therefore, we conclude that the less expensive model configuration with 32 layers is quite adequate to generate accurate simulations of the mixed-layer depth in the SJV.

- Use of an outer domain large enough to include most of the East Pacific Ridge is valuable for ensuring that the dynamics of the anticyclone are simulated well and are consistent with other scales of motion influencing the model solutions in the SJV.

- Removal of analysis nudging in the region below 1.5 km AGL on the coarser domains improved the simulations of mixed-layer depth on the 4-km grid (even though that domain did not directly use any FDDA).

- The 1.5-order TKE-predicting turbulence scheme (Shafran et al. 2000) provided much more accurate simulations of mixed-layer depth than were possible when using the Blackadar nonlocal-closure scheme (Zhang and Anthes 1982).

The second step was to determine the *physical and dynamical processes* responsible for the unusually shallow boundary-layer heights found in the SJV during episodes of poor air quality. The following are the most important conclusions deduced from the sensitivity experiment results:

- Widespread subsidence is induced by the synoptic-scale East Pacific Ridge and acts across the entire 4-km domain, especially when the ridge builds eastward over land as the 2-6 August 1990 episode proceeds. This synoptic-scale subsidence averages about -0.5 cm s^{-1} and acts continuously throughout the diurnal cycle. While it is an important factor producing adiabatic heating in the middle troposphere, this alone cannot explain the shallow mixing depths in the SJV. Otherwise, similar shallow mixing depths would be found in nearby strongly heated inland regions of the western United States during the same episodes.

- Strong surface sensible-heat fluxes lead to rapid modification of cool marine air as it is advected inland by the regional scale pressure gradient. This heating causes surface potential temperatures to approach those above the capping inversion within just a few hours and over distances of less than 100 km from the coast. Therefore, the shallow SJV mixing depths cannot be explained as a remnant of the marine atmospheric boundary layer.

- Synoptic-scale subsidence is reinforced over the SJV by the return branch of the mesoscale upslope valley breeze. The induced mesoscale subsidence produces enhanced adiabatic warming in the region above the convectively unstable boundary layer over land. This mesoscale subsidence has a daily average of about -0.35 cm s^{-1} on 5-6 August 1990. However, since the valley breeze is driven by the diurnal heating cycle, it should be considerably stronger during the afternoon hours, thereby contributing to especially low mixing depths at the time of maximum daily heating over the SJV.

- Since very high concentrations of ozone do not occur every day during the summer, it is likely that the mixed-layer depths in the SJV become especially shallow primarily when the synoptic-scale and mesoscale subsidence mechanisms both exceed average values, as when the East Pacific Ridge shifts onshore.

5. Future Research

To further improve boundary layer predictions over the central California region, particularly to benefit air pollution modeling studies, it is highly desirable that the new formulations we developed in this study be implemented and tested rigorously in MM5. Because the 1-D model results were very encouraging, we anticipate that the implementation of these new formulations will lead to better predictions of mixed-layer depths.

References

Ahrens, C.D., 1993: Essentials of Meteorology. West Publishing Co., 437 pp.

Alapaty, K., D.T. Olerud, K. Schere and A.F. Hanna, 1995: Sensitivity of Regional Oxidant Model Predictions to Diagnostic and Prognostic Meteorological Fields. *J. Appl. Meteor.*, **34**, 1787-1801.

Alapaty, K., S. Raman, and D.S. Niyogi, 1997a: Uncertainty in the specification of surface characteristics: A case study of prediction errors in the boundary layer. *Bound.-Layer Meteor.*, **82**, 473-500.

Alapaty, K., J.E. Pleim, S. Raman, D.S. Niyogi, and D.W. Byun, 1997b: Simulation of atmospheric boundary layer processes using local- and nonlocal-closure schemes. *J. Appl. Meteorol.*, **36**, 214-233.

Alapaty, K., and R. Mathur, 1998: Effects of atmospheric boundary layer mixing representations on vertical distribution of passive and reactive tracers. *Meteorol. and Atmos. Phy.*, **69**, 101-118.

Alapaty, K., and D.S. Niyogi, 1999: A Study to Improve the Existing MM5 Land-Surface Scheme using Statistical Indices. The Ninth PSU/NCAR Mesoscale Model Users' Workshop, pp 12, 23-25 June 1999, Boulder, Colorado, USA.

Anthes, R.A., E.-Y. Hsie, and Y.-H. Kuo, 1987: *Description of the Penn State/NCAR Mesoscale Model Version 4 (MM4)*. NCAR Tech. Note, NCAR/TN-282+STR, 66 pp.

Blackadar, A.K, 1976: Modeling the nocturnal boundary layer. Preprints, *Third Symposium on Atmospheric Turbulence, Diffusion and Air Quality*, Raleigh, Amer. Meteor. Soc., 46-49.

Blackadar, A.K., 1979: Modeling pollutant transfer during daytime convection. Preprints, *4th Symposium on Turbulence, Diffusion and Air Pollution*, Reno, Amer. Meteor., Soc., 443-447.

Blumenthal, D.L., et al.1993: Field program plan for the San Joaquin Valley air quality study (SJVAQS) and the atmospheric utility signatures, predictions, and experiments program. [Available from The Valley Air Pollution Study Agency, Sacramento, CA.]

Businger, J.A., J.C. Wyngaard, Y. Izumi and E.F. Bradley, 1971: Flux-profile relationship in the atmospheric surface layer. *J. Atmos. Sci.*, **28**, 181-189.

Carlson, T.N., and F.E. Boland, 1978: Analysis of urban-rural canopy using a surface heat flux/temperature model. *J. Appl. Meteor.*, **17**, 998-1013.

Chang, J.S., R.A. Brost, I.S.A. Isaken, S. Madronich, P. Middleton, W.R. Stockwell, and C.J. Walcek, 1987: A three-dimensional Eulerian acid deposition model: Physical concepts and formulation. J*. Geophys. Res.*, **92**, 14681-14700.

Deardorff, J., 1978: Efficient prediction of ground surface temperature and moisture, with inclusion of a layer of vegetation. *J. Geophys. Res.*, **83**, 1889-1903.

Detering, H.W., and D. Etling, 1985: Application of E-ε turbulence model to the atmospheric boundary layer. *Bound.-Layer Meteor.*, **33**, 113-133.

Dickinson, R.E., Kennedy, P.J., Henderson-Sellers, A., 1993: Biosphere-Atmosphere Transfer Scheme (BATS) - Version 1E as coupled to the NCAR Community Climate Model. NCAR Tech. Note NCAR/TN-387+STR, National Center for Atmospheric Research, Boulder, CO, 72 pp.

Dudhia, J., 1989: Numerical study of convection observed during the winter monsoon experiment using a mesoscale two-dimensional model. J. Atmos. Sci., 46, 3077-3107.

Dudhia, J., 1993: A nonhydrostatic version of the Penn State-NCAR Mesoscale Model: Validation tests and simulation of an Atlantic cyclone and cold front. Mon. Wea. Rev., 121, 1493-1513.

Grell G. A., J. Dudhia, and D. R. Stuaffer, 1994: *A description of the fifth – generation Penn State / NCAR mesoscale model (MM5)*, NCAR TN – 398+STR, 138 pp.

Hass, H., H.J. Jacobs, M. Memmesheimer, A. Ebel, and J.S. Chang, 1991: Simulation of a wet deposition case in Europe using the European Acid Deposition Model (EURAD). *In Air Pollution Modeling and its Applications VIII*, Plenum Press, New York, 205-213.

Holtslag, A.A.A., E.I.F. de Bruijn, and H.-L. Pan, 1990: A high resolution air mass transformation model for short-range weather forecasting. *Mon. Wea. Rev.*, **118**, 1561- 1575.

Idso, S., R. Jackson, B. Kimball, and F. Nakayama, 1975: The dependence of bare soil albedo on soil water content. *J. Appl. Meteor. ,* **14**, 109-113.

Jacquemin, B., and J. Noilhan, 1990: Sensitivity study and validation of land surface parameterization using the HAPEX-MOBILHY data set. *Bound.-Layer Meteor.,* **52,** 93-134.

Kain, J.S., and J.M. Fritsch, 1990: A one-dimensional entraining/detraining plume model and its application in convective parameterization. J. Atmos. Sci., 47, 2784-2802.

Lakhtakia, M.N., 1999: Multiple-Storm Simulations: A First Step to Regional Climate Modeling. The Ninth PSU/NCAR Mesoscale Model Users' Workshop, pp 194, 23-25 June 1999, Boulder, Colorado, USA.

Leidner, S.M., D.R. Stauffer, and N.L. Seaman, 2000: Improving short-term numerical weather predictions in the California coastal zone by dynamic initialization of the marine boundary layer. Submitted to Mon. Wea. Rev., 128, 39 pp.

Lohmann, U., N. McFarlane, L. Levkov, K. Abdella, and F. Albers, 1999: Comparing different cloud schemes of a single column model by using mesoscale forcing and nudging technique. *J. Clim.*, **12**, 438-461.

Mahfouf J., 1991, Analysis of soil moisture from near - surface parameters: a feasibility study, J. Appl. Meteor., 30, 1534 - 1551.

Mellor, G.L., and T. Yamada, 1974: A hierarchy of turbulence closure models for planetary boundary layers. *J. Atmos. Sci.,* **31,** 1791-1806.

Monin, A.S., and A.M. Yaglom, 1971: *Statistical Fluid Mechanics. Vol. I,* MIT Press, 468-504.

Niyogi D., S. Raman, K. Alapaty K., and J. Han, 1997: A dynamic statistical experiment for atmospheric interactions, *Environ. Model. Assess.,* **2**, 209 – 225.

Niyogi D., S. Raman, and K. Alapaty, 1999: Uncertainty in specification of surface characteristics, Part II: Hierarchy of interaction – explicit statistical analysis, *Bound.-Layer Meteor.,* **91**, 341 – 366.

Noilhan, J., and S. Planton, 1989: A simple parameterization of land surface processes for meteorological models. *Mon. Wea. Rev.*, **117**, 536-549.

Pederson, J.R., et al.1995: California Ozone Depostion Experiment: Methods, Results, and Opportunities. *Atmos. Envi.*, **29**, 3115-3132.

Pleim, J.E., and A. Xiu, 1995: Development and testing of a surface flux planetary boundary layer model with explicit soil moisture parameterization for applications in mesoscale models. *J. Appl. Meteor.*, **34**, 16-32.

Pleim, J.E., and J.S. Chang, 1992: A non-local closure model for vertical mixing in the convective boundary layer. *Atmos. Environ.,* **26A,** 965-981.

Ranzieri, A. J., and R. Thuiller, 1991: San Joaquin Valley Air Quality Study (SJVAQS) and Atmospheric Utility Signatures, Predictions and Experiments (AUSPEX): A collaborative model program. Preprints, 84th Annual Meeting and Exhibition of A&WMA, Vancouver, BC, Canada, A&WMA, 1-27.

Ruggiero, F.H., K.D. Sashegyi, R.V. Madala, and S. Raman, 1996: The Use of Surface Observations in Four-Dimensional Data Assimilation in a Mesoscale Model, Mon. *Wea. Rev.*, **124**, 1018 - 1033.

Russell, A. G., and R. Dennis, 2000: NARSTO critical review of photochemical models and modeling, *Atmos. Environ.,* **34**, in press.

Schumann, U., 1989: Large-eddy simulation of turbulent diffusion with chemical reactions in the convective boundary layer. *Atmos. Environ.*, **23**, 1-15.

Seaman, N.L., D.R. Stauffer, and A.M. Lario-Gibbs, 1995: A multiscale Four-Dimensional Data Assimilation System Applied to in the San Joaquin Valley during SARMAP. Part I: Modeling Design and Basic Performance Characteristics. *J. Appl. Meteor.*, **34**, 1739-1754.

Sellers P. J., F. G. Hall, G. Asrar, D. E. Strebel, and R. E. Murphy. 1992: An overview of the **F**irst **I**nternational Satellite Land Surface Climatology Project (ISLSCP) **F**ield **E**xperiment (FIFE). *J. Geophys. Res.*, **97**, 18,345-18,371.

Shafran, P.C., N. L. Seaman, and G. A. Gayno, 2000: Evaluation of numerical predictions of boundary – layer structure during the Lake Michigan Ozone Study (LMOS). *J. Appl. Meteor.,* **39**, 412-426.

Sistla G., N. Zhou, W. Hao, J. –K. Ku, S. T. Rao, R. Bornstein, F. Freedman, and P. Thunis, 1996: Effects of uncertainties in meteorological inputs on Urban Airshed Model predictions and ozone control strategies, *Atmos. Environ.,* **30**, 2011 – 2025.

Stauffer, D.R., and N.L. Seaman, 1990: Use of four-dimensional data assimilation in a limited area mesoscale model. Part I: Experiments with synoptic-scale data. *Mon. Wea. Rev.*, **118**, 1250-1277.

Stauffer, D. R., N. L. Seaman, and F. S. Binkowski, 1991: Use of four – dimensional data assimilation in a limited-area mesoscale model. Part II: Effects of data assimilation in the planetary boundary layer, *Mon. Wea. Rev.,* **119**, 734 – 754.

Zhang, D. L., and R. A. Anthes, 1982: A high resolution model of the planetary boundary layer: Sensitivity tests and comparisons with SESAME-79 data, *J. Appl. Meteor.,* **21**, 1594 – 1609.

Glossary of Symbols

A	Constant
C_1, C_2	Soil moisture coefficients
C_d	Mean drag coefficient for leaves
C_p	Specific heat of air at constant pressure
C_T	Inverse of the thermal capacity of a particular soil type
d	Displacement height
d_1, d_2	Model's layer 1 and 2 thicknesses
E	Total kinematic latent heat flux or turbulent kinetic energy
e_a	Actual vapor pressure
E_a , E_p	Total actual evaporation and total potential evaporation
E_{as}	Actual evaporation from bare soil
E_{av}	Actual evapotranspiration from vegetation
E_g	Evaporation flux at the soil surface
E_{ps}	Potential evaporation from bare soil
E_{pv}	Potential evapotranspiration from vegetation
E_r	Evaporation rate from the wet parts of the canopy
E_{tr}	Transpiration flux
F	Forcing term representing the effects of all physical processes
G	Soil heat flux
g	Acceleration due to gravity
G_α	Nudging factor (magnitude) for α
h	Depth of atmospheric boundary layer or height of the vegetation
k	Von Karman constant
K_a	Background molecular diffusivity
K_m , K_h	Coefficients of eddy diffusivity for momentum and heat
K_o	Background vertical eddy diffusivity in the free atmosphere
K_z	Coefficient of vertical eddy diffusivity for heat, momentum, and moisture in stable boundary layer.
LAI	Leaf area index
L_{hf}	Turbulent latent heat flux
M	Mass mixing rates
M_a	Soil moisture availability
M_a^*	Modified soil moisture availability
P_g	Flux of liquid water reaching the soil surface
P_r	Precipitation rate at the top of the vegetation
Q	Radiation reaching the ground at a given instant
Q_{max}	Maximum radiation reaching the ground
q_{va}	Water vapor mixing ratio of air in the lowest layer of the model
q_{vs}	Saturated water vapor mixing ratio
r_{ah}	Aerodynamic resistance for heat
r_{av}	Aerodynamic resistance for water vapor

R_c	Critical Richardson number
R_i	Richardson number
r_{lb}	Leaf boundary resistance
R_n , R_{ns}	Net radiation reaching the surface
R_{ns}	Radiation reaching bare soil
R_{nv}	Radiation reaching the vegetation
R_r	Runoff rate from canopy interception reservoir.
r_{smin}	Minimum stomatal resistance
r_{soil}	Soil surface resistance
r_{st}	Stomatal resistance
S	Vertical wind shear
S_{hf}	Turbulent sensible heat flux
t	Time
T_{g1}	Temperature of first soil layer
T_{g2}	Temperature of second soil layer
u_*	Friction velocity
$\overline{U}$	Mean horizontal wind speed
V_c , ξ	Vegetation cover in fractional units
WDI	Water deficit index
W_{g1}, W_{g2}	Volumetric soil moisture contents of the two soil layers,
W_{geq}	Layer 1 soil moisture when gravity balances the capillary forces
W_r	Water content on the wet parts of the canopy due to rainfall and/or dew formation on the foliage
W_s	Soil moisture
W_{wilt}	Soil moisture during wilting conditions
z_a	Altitude of the lowest level in the model
z_o	Roughness length
z_λ	Depth of the molecular layer
τ	Number of seconds in a day
Φ_h	Nondimensional stability parameter for heat
Θ_v	Virtual potential temperature
ι	Characteristic turbulent length scale
θ_*	Scale for temperature
λ_w	Average leaf width
$\hat{a}$	Analyzed value obtained from observations for α
$\Delta\sigma$, Δz	Relative mass in or thickness of a grid cell
Δt	Diffusion time step
ρ_w	Density of liquid water
ε	Dissipation rate of turbulent kinetic energy
α	Prognostic variable for which observations are available
γ	Psychrometric constant
Δ	Ratio of the change in saturation vapor pressure (e_s)
δ	Shielding factor
σ	Vertical coordinate